Aalto University
School of Engineering

Tamer Gökdemir

Quantification of deformation trends in a sublevel caving mine using mobile 3D laser scanning

Master's thesis submitted in partial fulfilment of the requirements for the degree of Master of Science in Technology

Espoo: 22.02.2021
Supervisor: Prof. Mikael Rinne
Advisor: Tristan Jones, PhD

Aalto University
School of Engineering

Aalto University, P.O. BOX 11000, 00076
AALTO
www.aalto.fi

Abstract of master's thesis

Author Tamer Gökdemir

Title of thesis Quantification of deformation trends in a sublevel caving mine using mobile 3D laser scanning

Master programme European Mining, Minerals and Environmental Programme (EMMEP) **Code** ENG3077

Thesis supervisor Prof. Mikael Rinne

Thesis advisor(s) Tristan Jones, PhD

Date 22.02.2021 **Number of pages** 97+5 **Language** English

Abstract:

The Malmberget mine shows, in its great geological variety some weak rock zones consisting mainly of granites with biotite schist inclusions in the footwall as well as in the crosscuts, which forced the mine to stop mining in some drifts and invest in supplementary support and blasting of the floor to keep the tunnels open. Therefore, the mine is seeking to better understand the linkage between underground production, mining-induced stresses and deformation in different geologic structures encountered.

The conducted research assesses trends in deformation based on geotechnical parameters in three orebodies with a mobile LiDAR system, namely the uGPS Rapid Mapper™, to gain a higher understanding of current deformations. By doing that also the real-life capabilities of the scanning system were observed.

The study started with a comprehensive literature review about rock mass classification systems, deformation in underground excavations and mobile laser scanning in an underground environment to be at the current state of research. The further scope includes several hundred scans in areas that are prone to deformation for testing the repeatability and accuracy of the mobile scanner as well as detecting trends in deformation. Additionally, field observations regarding deformation changes, damages, water inflows and occurrence of additional reinforcement measures were collected.

The designed tests and conducted scans showed that the uGPS Rapid Mapper™ works within the known parameters. The intention to detect and track deformation on a regular basis with little work power is given. Also, the immediate 3D visualization proved to be valuable for interpreting data. Deformation commonly occurs in grey leptite with an elevated content of biotite schist intrusions when the GSI is 10-35 and especially when adjacent a competent rock mass is present. This condition is often present at the ore contact zone.

The research was able to further support suspected deformations and provide more accurate numbers of deformation. The work supports the hypothesis that convergence occurs mainly in areas of geotechnically weak zones due to squeezing mechanisms.

Keywords Underground Mining, Sublevel Caving, Rock Mechanics, LiDAR Scanning, Mobile Scanning, Convergence Monitoring, Deformation

Preface

First of all, I would like to thank Prof. Mikael Rinne for his great support and assistance during the study. In addition to my supervisor, I would like to express my gratitude to Tristan Jones who initiated the research and was always there for me when I had questions. Completion of this thesis would not have been possible without their effort.

I thank all colleagues from the Rock Mechanics department as well as other departments at LKAB for their assistance and all the discussions we had at daily coffee breaks.

Finally, I would like to thank my parents and sister for supporting me to reach my goals and encouraging me throughout this hard year. A special thanks must be addressed to Gözde who kept me motivated and took my mind off the thesis.

Espoo, 22.02.2021

Tamer Gökdemir
Many thanks and Glück auf!

Table of Content

List of Figures

List of Tables

Abbreviations

AL *Alliansen*

D_e *Equivalent dimension of the excavation*

ESR *Excavation support ratio*

GSI *Geological strength index*

HO *Hoppet*

IMU *Internal measurement reading unit*

LHD *Load-haul-dump (loader)*

LiDAR *Light detection and ranging*

LKAB *Luossavaara-Kiirunavaara Aktiebolag*

PR *Printzsköld*

RFID *Radio-frequency identification*

RQD *Rock quality designation*

UCS *Uniaxial compressive strength*

UTS *Uniaxial tensile strength*

1 Introduction

1.1 Problem statement

The Malmberget mine shows, in its great geological variety some weak rock zones consisting mainly of granites with biotite schist inclusions in the footwall as well as in the crosscuts, which forced Luossavaara-Kiirunavaara Aktiebolag (LKAB) to stop mining in some drifts such as in the Printzsköld orebody. The biotite schist between the strong ore and host rock is the weakest zone and leads to deformation through a squeezing mechanism under stress. An additional consequence is the need for cost intensive supplementary support and blasting of the floor to keep the tunnels open. Therefore, the mine is seeking to better understand the linkage between underground production, mining-induced stresses and deformation in different geologic structures encountered in the mine, as well as how different rock support or reinforcement techniques are functioning to reach higher safety standards and an ongoing production resulting in higher efficiency and recovery rates.

1.2 Aim and objectives

The aim of the research is to identify and quantify trends in deformation based on different geotechnical parameters from level 996 to 1082 in three orebodies of the mine, namely Printzsköld (PR), Hoppet (HO) and Alliansen (AL) with a mobile light detection and ranging (LiDAR) system, the uGPS Rapid Mapper™, to gain a higher understanding of current deformations and their impact on the overall production. By doing that, there are different objectives:

- What are the real-life capabilities of the uGPS Rapid Mapper™ in the Malmberget Mine?
- How do geotechnical properties and production impact deformation?
- What is the trend and magnitude of deformation?

Additionally, the research provides guidance on how deformation can be detected with the used approach by understanding the mobile LiDAR system and analysis in underground excavations to work efficiently in the future.

1.3 Approach

The thesis work is divided in different stages to reach the aim and objectives. For the mentioned research the uGPS Rapid Mapper™ by Peck Tech Consulting Ltd. is used. The scanner is installed on a vehicle to scan with a typical speed of 3 km/h. It is the first use of a comparable device in the Malmberget Mine and therefore it is also of great interest to gain more knowledge about the system since the mobile and fast scanning procedure is a big advantage in a mining environment in comparison to common stationary scanning and other monitoring possibilities. Scans can be conducted regularly to detect movements on short-term.

The first step includes the implementation of the uGPS Rapid Mapper™ and gaining a better understanding of collected data to identify real deformation. To have comparable scans, highly reflective targets are used and surveyed in the research area. By doing that the scans can be georeferenced. For a better understanding of the results several experiments are designed, conducted and analysed prior to the interpretation of gained data.

The main field work includes scans of the research area in defined time intervals and the mapping of deformation, damage, water inflows and occurrence of additional reinforcement measures. Prior to that, it was necessary to know which areas are prone to deformation and of central interest for the mine. Areas of interest were already assigned in earlier researches and marked. Several footwall drifts and crosscuts in PR 996, PR 1023, PR 1051, HO 1023, HO 1051, HO 1080, AL 1052 and AL 1082 are investigated. Additionally, literature research on deformation in underground excavations with a focus on mobile laser scanning systems is carried out during the thesis work to be at the current state of research.

After the data collection through several hundred scans the analysis is conducted. Earlier studies in some drifts of the research area made ongoing damage mapping and deformation information available, which are used as an additional source of information to support the collected data. Geotechnical characteristics are analysed in the different orebodies based on internal production records as well as publications. The collected data of the mobile laser scanner is observed in CloudCompare regarding the individual scans and deformation between scans of different times.

1.4 Thesis outline

The thesis is divided into eight chapters:

Chapter 2: Systematic review of literature – describing rock mass classification approaches, deformations in mining and mobile laser scanning appliances in underground excavations

Chapter 3: Presentation of the research area including general information

Chapter 4: A detailed description of the current state in the research area regarding impacts of deformation and parameters influencing the deformation

Chapter 5: The uGPS Rapid mapper™ with specifications, implementation and validation of real-life capabilities

Chapter 6: Results of the methodology

Chapter 7: Discussion of the results obtained in the study

Chapter 8: Conclusion of the research work

Chapter 8: Recommendations for future work

1.5 Site information

As a basis of the thesis, this subsection clarifies the general settings of the mine with the mining method and occurring geology.

1.5.1 LKAB

With three operating mines and an 80 % share of the produced iron in Europe, LKAB is a leading iron ore producer on global scale. LKAB was founded in 1890 and is 100 % state owned since 1950. Industrial mining in Kiruna and Malmberget started in the beginning of the 1900s after the construction of the railway from Luleå to Narvik crossing both mines, but already in the 1660s iron ore samples were collected. The infrastructure of the company in Scandinavia consists of three mines with processing plants, the ore railway, the head office and the harbour in Luleå for mainly the European market and the southern division as well as the harbour in Narvik for mainly the global market and the northern division (Figure 1) (LKAB, 2019).

Figure 1: Infrastructure Scandinavia LKAB (LKAB, 2019)

In 2019 stable and favourable market conditions enabled the company to achieve strong earnings. LKAB produced 27.2 Mt of iron ore products and registered sales of 31.26 BSEK, from which 90 % are accounted to iron products. This resulted in a profit of 11.79 BSEK and an operating margin of 37.7 % (LKAB, 2019).

Table 1 shows the mineral reserves and resources of the operating mines at LKAB. The company also published in the annual report of 2018 mineral resources of 471 Mt at not operating locations, which are not mentioned in the table (LKAB, 2018).

Table 1: Mineral reserves and resources of operating mines at LKAB (LKAB, 2018)

	Kiruna		Malmberget		Leveäniemi	
	Quantity [Mt]	Fe [%]	Quantity [Mt]	Fe [%]	Quantity [Mt]	Fe [%]
Proven reserves	624	44.1	346	42.6	87	48.1
Probable reserves	62	40.5	23	41.8	9	37.5
Measured resources	0	-	6	45.1	67	46.6
Indicated resources	35	36.6	103	43.2	71	42.5
Inferred resources	355	42.2	194	44.0	34	41.7

1.5.2 Malmberget Mine

The mine is located in the municipality of Gällivare about 70 km north of the Arctic Circle in Northern Sweden. The mining area includes 20 orebodies, of which about half of them are mined currently. The total aerial size of the orebodies is around 2.5x5 km with an eastern and western major ore field. The western part is divided in the Välkomman, Baron, Johannes, Hends and Josefina orebodies while the eastern part is divided in the Printzsköld, Hoppet, Alliansen, Fabian, Dennewitz, Parta, Östergruvan and Vi-Ri orebodies (Figure 2). Current mining is in a depth of 800 m to 1200 m.

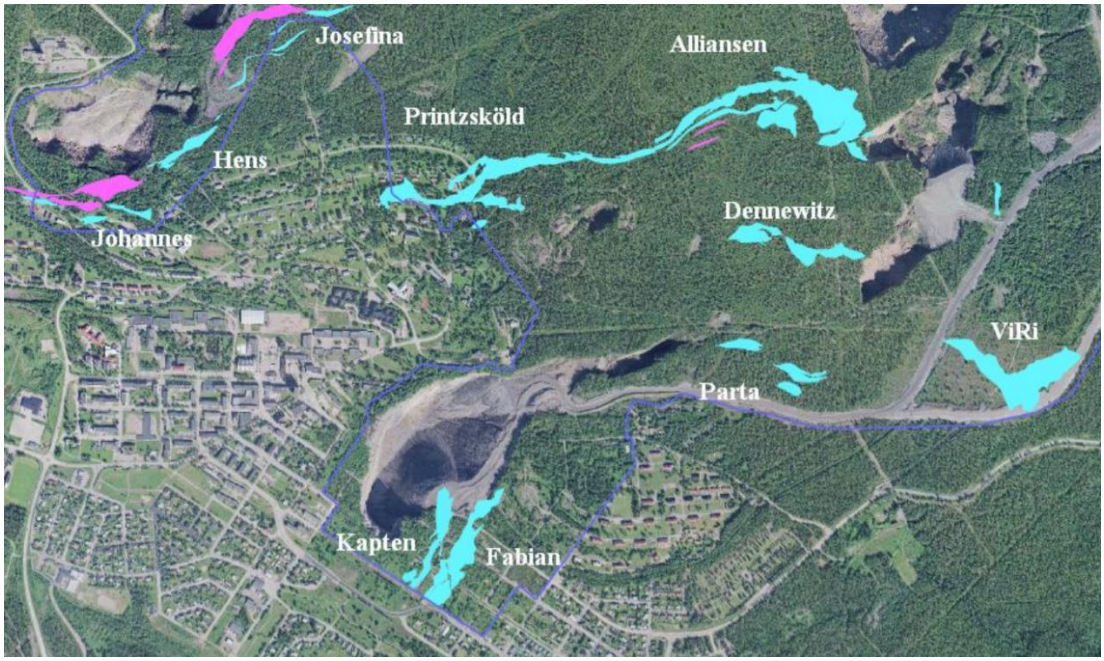

Figure 2: Plan view of mining area with orebodies. Blue stands for magnetite and magenta for hematite (LKAB database)

In the beginning during the 1900s mining was done through open-pit mining in Malmberget as well as in Kiruna. The shift to underground mining started in the 1920s and since the 1960s sublevel caving is the principal mining method in the orebodies of Malmberget. In that time the sublevel height was about 15 m. With the following years the sublevel height could be maximized to 20 to 30 m, which leaded to a higher efficiency in mining operations caused by mainly lower development costs. In General, transverse sublevel caving is used in Malmberget, but due to different shapes of orebodies, dips, strikes, stresses and other considered factors in some orebodies, such as Baron, the longitudinal sublevel caving mining method is used sometimes (Quinteiro, Quinteiro, & Hedström, 2001).

1.5.3 Sublevel Caving

Figure 3 shows a typical transverse sublevel caving layout. In the transverse sublevel caving the production drift orientation is perpendicular to the strike of the orebody and the rings are blasted towards the footwall side starting at the hanging wall. The longitudinal sublevel caving method is defined by production drifts parallel to the

strike of the orebody. This results in a mining sequence along the strike of the orebody from start to end (Dunstan & Power, 2011).

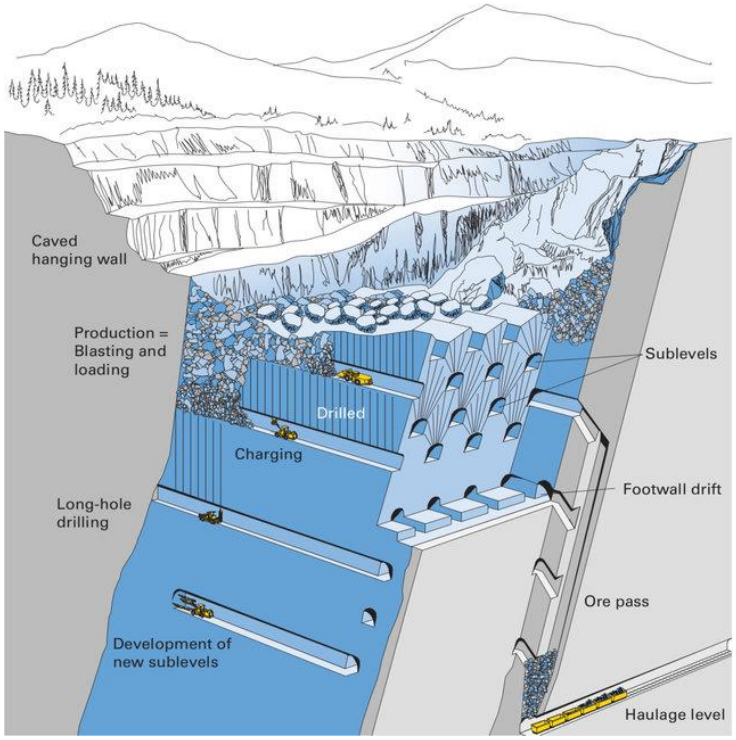

Figure 3: Sublevel caving mining layout (Atlas Copco, 2007)

The mining method relies on the gravity flow process and the cavability of the overlying orebody, which leads through production blasts to the caving of the orebody into the void. Afterwards the material is loaded with load-haul-dump loaders (LHDs) from the draw points to transport it to the ore passes where the ore is collected at the main haulage level (Quinteiro, Quinteiro, & Hedström, 2001). The current main haulage levels are located at level 1000 and 1250 each having two crushers. After the crushing step the ore is transported with a combination of shafts and conveyor belts to the surface.

The method combines a high productivity and recovery with low mining costs. Furthermore, it is suitable for full mechanization and therefore, also linked to good health and safety standards. Disadvantages are extensive initial development costs, which account in general to 15-20 % of the production costs, possibly occurring problems in the draw control and the subsidence of the surface.

1.5.4 Geology

The Malmberget mine has one of the largest apatite-iron ore deposits of the world (Figure 4). The orebodies of the western part contain magnetite and hematite with an elevated share of apatite while the eastern orebodies contain mainly magnetite with a low share of apatite. Alliansen has a few areas with hematite. The orebody shows a vein system with impregnations of several minerals and is strongly affected by metamorphic recrystallisation. The main gangue minerals are apatite, amphibole, pyroxene and biotite and granitic intrusions often cross the ore (Bergman, Kübler, & Martinsson, 2001). In average the orebodies are dipping with 45°-50° with a variation between 45° and 70°. The thickness of the orebodies range between 20 and 100 m. Approximately 90 % of the total ore is magnetite (Quinteiro, Quinteiro, & Hedström, 2001). The volcanic host rock consists of grey, red-grey and red leptites with increasing strength (Jones, Nordlund, & Wettainen, 2019).

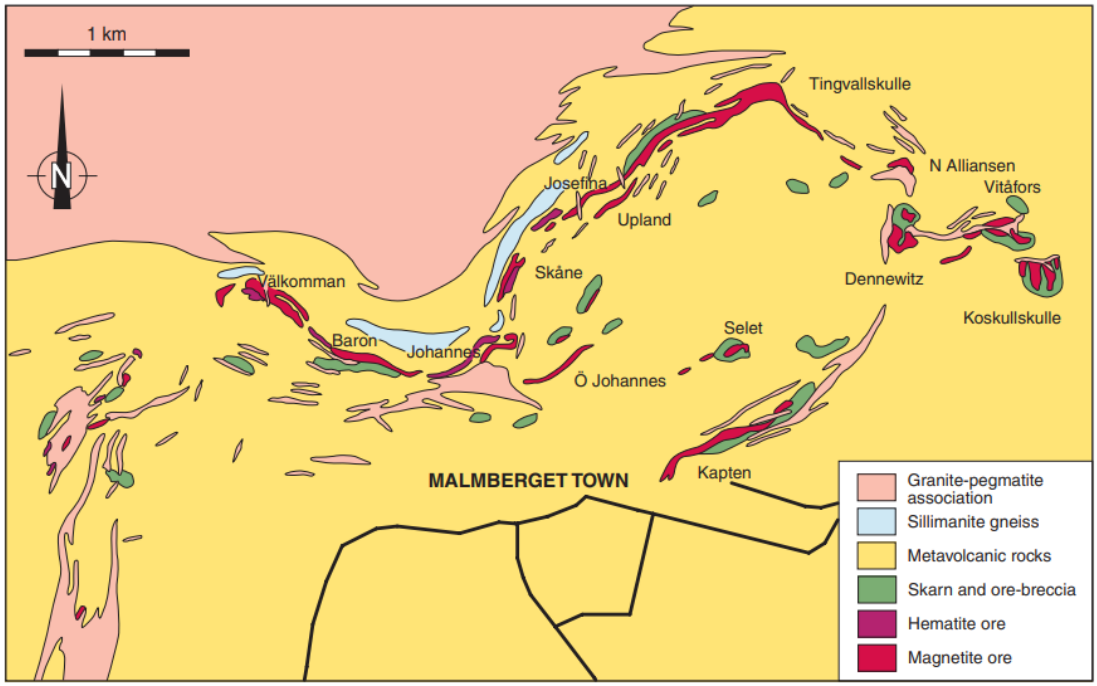

Figure 4: Geological map of Malmberget area with the orebodies (Bergman, Kübler, & Martinsson, 2001)

2 Literature review

2.1 Rock mass classification in rock engineering

The more information is given about the rock mass properties, the more precise the planning of the underground excavations can be. During rock mass classification, the rock masses are sorted into classes based on defined correlations and thus the characteristic behaviour can be forecasted (Bieniawski, 1989). The method lets the user follow a guide to classify the rock masses into a suitable class. The classes are often separated by properties such as discontinuities and joints. The classification serves as a way to communicate consistently and was created to assist the engineering procedure rather than replace field observations, measurements and engineering assessment (Bieniawski, 1993). According to Bieniawski (1989), the systems need further improvement to be used for final designs and complex underground excavations. However, in practice various rock mass classification systems have their legitimacy and provide a useful systematic aid in underground constructions (Hoek, 2007). The purpose of the rock mass classification is to (Bieniawski, 1993):

- Identify the most significant parameters influencing the behaviour of rock mass
- Divide the particular rock mass formation into a number of rock mass classes of varying quality
- Provide a basis for understanding the characteristics of each rock mass class
- Derive quantitative data for engineering design
- Recommend support guidelines for tunnels and mines
- Provide a common basis for communication between engineers and geologists
- Relate the experience on rock conditions at one site to the conditions encountered and experience gained at other sites.

A main advantage of rock mass classification is the improvement of investigations through a systematic identification and quantification of properties. Rational analysis is more valuable than subjective analysis. This results in better engineering judgment and effective communication during a project. A great risk of classification systems is the use of the systems as an ultimate solution to various problems and ignoring analytical and observational methods. Moreover, never one classification without using a second one for further analysis should be used (Bieniawski, 1993).

In order to adequately describe rock mass, various parameters must be taken into account. According to Bieniawski (1993), the important parameters for the description and classification of rock mass are as follows:

- The strength of the intact rock material
- The rock quality designation (RQD)
- Parameters of rock joints such as orientation, spacing and condition
- Groundwater pressure and flow
- In-situ stress
- Major geological structures.

Developed by Deere et al. (1967), the RQD is used as a standard parameter in drill core logging and its main advantage is its simplicity as well as the fast and cheap analysis. The index is defined in percent as the proportion of intact parts larger than 10 cm in the total length of the drill core log. Equation (1) shows the mathematical expression (Deere & Deere, 1988).

$$RQD\ [\%] = \frac{\sum Core\ pieces > 10\ cm\ [cm]}{Total\ length\ of\ drill\ core\ log\ [cm]} \times 100 \qquad (1)$$

RQD is an index of the fracturing of the rock mass and aims to represent the in situ rock mass quality. As shown in Table 2, the greater the RQD value the better the rock mass quality.

Table 2: Rock mass classification based on RQD (Deere et al., 1967)

RQD	Rock Mass Quality
< 25	Very poor

25 – 50	Poor
50 – 75	Fair
75 – 90	Good
90 – 100	Excellent

The disadvantage of the RQD is the limited view on the rock mass quality since only one parameter is considered. It considers only the fracturing of the rock mass and does not examine the rock strength or properties of the joints. RQD is used as a parameter in the RMR and Q system.

Frequently used rock mass classification systems in rock mechanics for underground excavations are RMR, Q and GSI systems.

To achieve the goal of determining the stability and reinforcement needs of underground excavations, the RMR system was developed by Bieniawski (1973). This made it possible to assign excavation dimensions as well as suitable support implementations in form of rock bolts, mesh, shotcrete or steel sets based on a rock mass classification. A great advantage is the consideration of a few parameters (Bieniawski, 1989). The following parameters are used for the classification according to Bieniawski (1989):

- Strength of intact rock material
- Rock quality designation (RQD)
- Discontinuity spacing
- Condition of discontinuities
- Groundwater conditions
- Orientation of discontinuities

Each of the listed parameter is evaluated quantitively based on the rock mass quality and then summed up with the other parameters, with the joint orientation serving as an adjustment factor. RMR classification is divided in five rock mass classes (Table 3).

Table 3: Meaning of rock mass classification by RMR (Bieniawski, 1978)

Rock type	Rock mass rating (class)				
Rating	100-81	80-61	60-41	40-21	<20
Class. of rock mass	Very good	Good	Fair	Poor	Very poor
Average stand-up time	10 years for 15 m span	6 months for 8 m span	1 week for 5 m span	10 h for 2.5 m span	30 min for 1 m span
Cohesion [kpa]	>400	300-400	200-300	100-200	<100
Friction angle [°]	>45	35-45	25-35	15-25	<15

The rock tunnelling quality index, the Q-system, was introduced by Barton, Lien and Lunde (1974) and is also a multi-parameter method. It consists of six parameters divided into three geotechnical parameters:

- Relative block size
- Relative frictional strength
- Active stress

The Q-system is defined as:

$$Q = \frac{RQD}{J_n} \times \frac{J_r}{J_a} \times \frac{J_w}{SRF} \quad (2)$$

where RQD = Rock quality designation

J_n = Joint set number

J_r = Joint roughness number

J_a = Joint alteration number

J_w = Joint water reduction factor

SRF = Stress reduction factor

A detailed breakdown of the six parameters with their respective values is provided in Appendix 1. The first quotient of the formula refers to the rock mass geometry and deals with the block size. As the RQD becomes larger with a smaller set of discontinuities, the values amplify each other in the first quotient (Hoek, 2007). The second quotient relates to the relative frictional strength and represents the roughness and friction of the joint surfaces (Singh & Geol, 1999). Better rock

mechanical properties are defined by a higher value of this quotient. The third quotient, as an empirical factor, defined by active stress by water pressure and flows, is greater with decreasing water pressure and favourable in-situ stress ratios (Hoek, 2007).

The system is used, among other things, to determine the support measures of a tunnel with known dimension. Using the Q-system and the equivalent dimension of the excavation (D_e), 38 different support categories were determined by Barton et al. (1974). Equation (3) shows the corresponding determination of D_e with the excavation support ratio (ESR) (Table 4), which depends on the use of the excavation and the safety demanded (Singh & Geol, 1999).

$$D_e = \frac{Excavation\ span(s), diameter\ (d)\ or\ height\ (m)}{Excavation\ Support\ Ratio\ (ESR)} \qquad (3)$$

Table 4: Values of the Excavation Support Ratio, ESR (Barton et al., 1974)

Excavation category		ESR
A	Temporary mine opening	3-5
B	Permanent mine openings, water tunnels for hydro power (excl. high-pressure penstocks), pilot tunnels, drifts & headings for large excavations	1.6
C	Storage rooms, water treatment plants, minor road & railway tunnels, surge chambers, access tunnels	1.3
D	Power stations, major road, and railway tunnels, civil defence chambers, portal intersections	1.0
E	Underground nuclear power stations, railway stations, sports and public facilities, factories	0.8

In further research Barton et al. (1980) recommended rock bolt length and the maximum support spans. The Q-system has been refined and completed in many works. Grimstad and Barton (1993) recommended a new support design chart based on new designed steel fiber reinforced shotcrete (Figure 5).

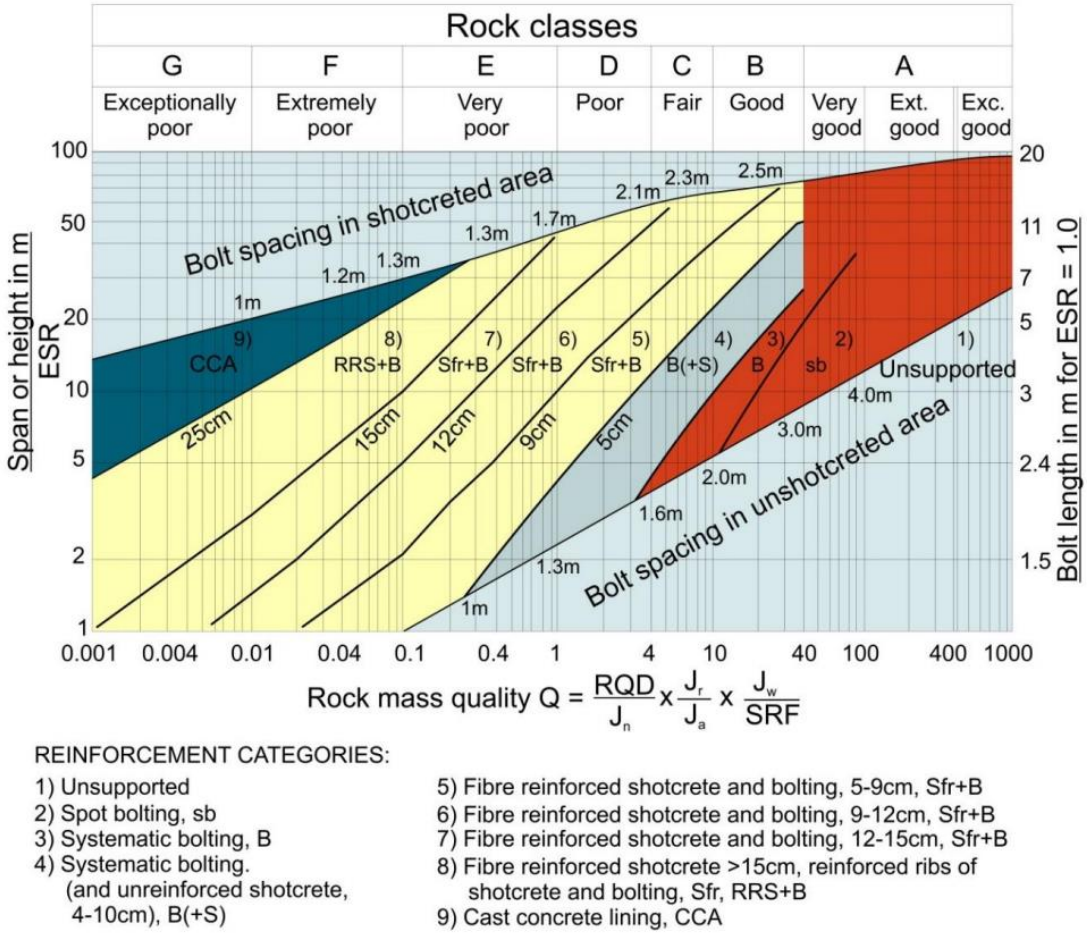

REINFORCEMENT CATEGORIES:

1) Unsupported
2) Spot bolting, sb
3) Systematic bolting, B
4) Systematic bolting. (and unreinforced shotcrete, 4-10cm), B(+S)
5) Fibre reinforced shotcrete and bolting, 5-9cm, Sfr+B
6) Fibre reinforced shotcrete and bolting, 9-12cm, Sfr+B
7) Fibre reinforced shotcrete and bolting, 12-15cm, Sfr+B
8) Fibre reinforced shotcrete >15cm, reinforced ribs of shotcrete and bolting, Sfr, RRS+B
9) Cast concrete lining, CCA

Figure 5: Support categories for rock mass classes by the Q-system and the support span or height [m] (Grimstad and Barton, 1993)

The GSI was presented by Hoek (1994) to summarize the rock mass characteristics of both hard and weak rock masses for rock mechanics in one system. It is based on previous work of Terzaghi's descriptions combined with the knowledge gained by the RMR system (Singh & Geol, 1999). To estimate an average GSI-value the relation between rock mass structure and rock discontinuity surface conditions is assessed. Hereby, it is recommended to use a range of values instead of a single value (Hoek, 1998). The GSI system is a simple and fast system to quantify the strength and deformation properties of rock mass (Singh & Geol, 1999). Since the introduction of the system, it has been modified by many other works to quantify the system. Another category was added to quantify more complex geological features with weak rock mass properties characterized by highly sheared and laminated series (Hoek, Marinos, & Benissi, 1998).

In this work, the GSI is defined between five rock mass structure types and the respective surface quality. The structure ranges from intact to laminated or sheared rock masses with a lack of blockiness due to close spacing of weak schistosity or shear planes. The surface quality ranges from very rough and unweathered surfaces to slickensided and highly weathered surfaces with soft clay coatings and fillings (Figure 6).

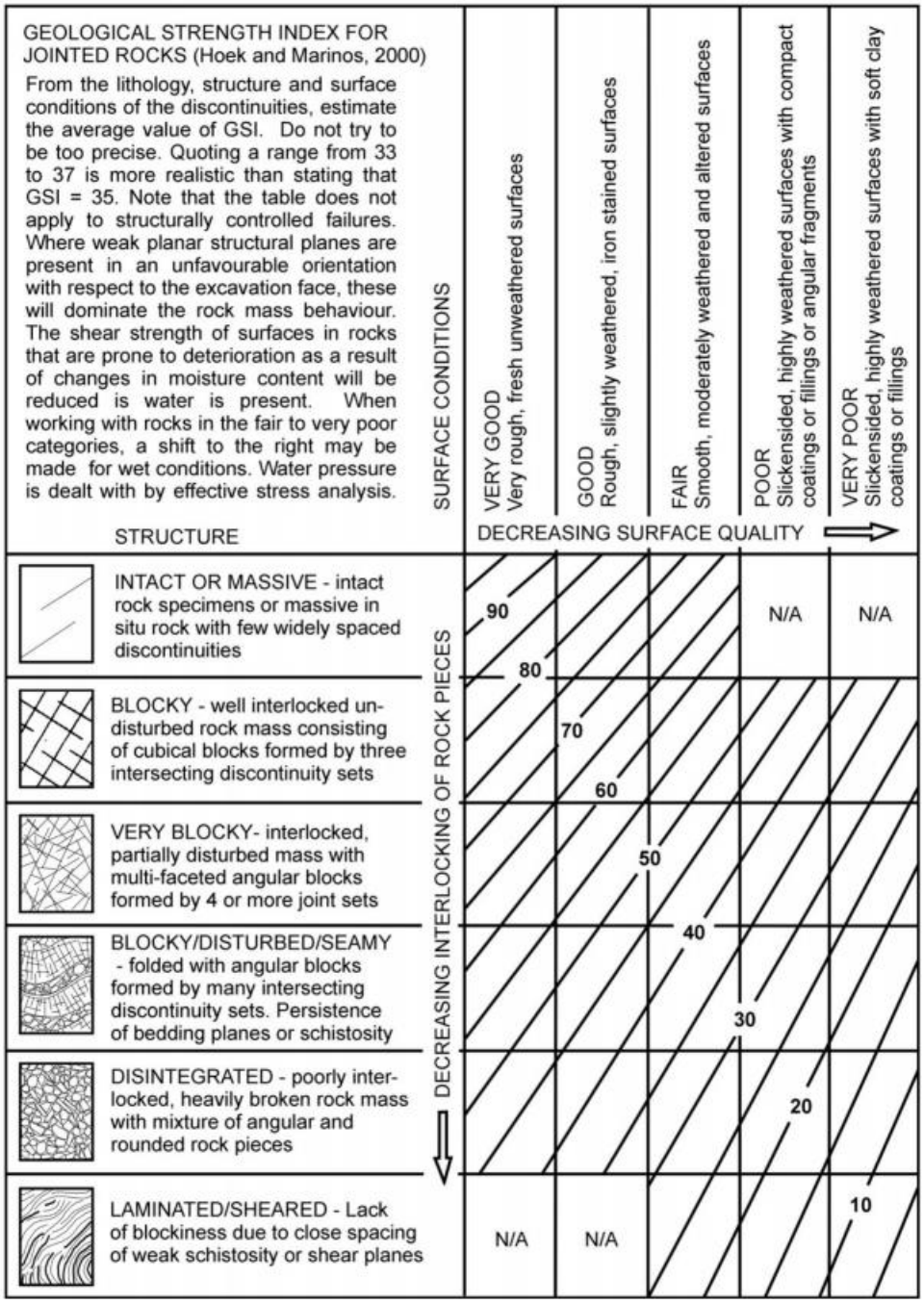

Figure 6: Modified table of Geological Strength Index (GSI) (Hoek et. al, 1998)

2.2 Deformations in underground excavations

The existing stress after an underground excavation is very different from the previous in-situ stress conditions. This can be the impulse for different types of error in rock mass behaviour. A common problem is that due to high stresses, stability is compromised and can result in surface splitting, bending and spalling. Furthermore, a shear failure can happen due to the overload of the existing stress field and blocks can fall out caused by the weakness of the rock (Stille, 2001). The GSI-Value is an efficient classification to assess the rock mass strength and tunnel behaviour. Like other rock mass classifications, the GSI should not be considered on its own when designing tunnels (Marinos, Marinos, & Hoek, 2005). Marinos (2012) defined the rock mass and tunnel behaviour linked to the GSI chart in a tunnel behaviour chart for an overburden of several hundred meters (Figure 7).

The existing in-situ stress can be impacted by many factors. The vertical in-situ stress can be derived from the depth combined with the specific gravity of the rock types above the point. However, there are some factors such as tectonic stress, surface topography, residual stress, discontinuities as well as fracture sets that influence the vertical in-situ stress (Brady & Brown, 2004). The exact determination of the stresses turns out to be complex in practice. Brady and Brown (2004) emphasized that an exact determination of the in-situ stresses is hardly possible with random measurements and has to be carried out according to the site-specific rock structure.

Excavations in jointed, weak to average rock mass with high in-situ stresses are more likely to have a squeezing rock behaviour. The behaviour occurs when the characteristic rock properties and induced stresses push areas next to the tunnel that surpass the limiting shear stress (Barla, 2005). No stress change is necessary for creep so convergence happens even if the tunnel advance stops (Harrison & Hudson, 2000). Martin et. al (2003) highlighted that mining induced stresses play a major role in the rock mass behaviour of underground excavations. At the Malmberget Mine, Jones et al. (2019) has shown that deformations are bigger in weak rock and become stronger in crosscuts when they are close to production blasting. Furthermore, it has been

shown that the redistribution of stresses has a greater influence than the proximity to production blasting. Ultramafic rocks, joint infill materials, shearing of faults and foliation are indicators for a higher possibility of squeezing rock (Varden & Woods, 2015). A high stress field and a weak σ_{ci}-value of > 60 MPa was an observed property for squeezing conditions in earlier case studies in underground excavations (Potvin & Hadjigeorgiou, 2008).

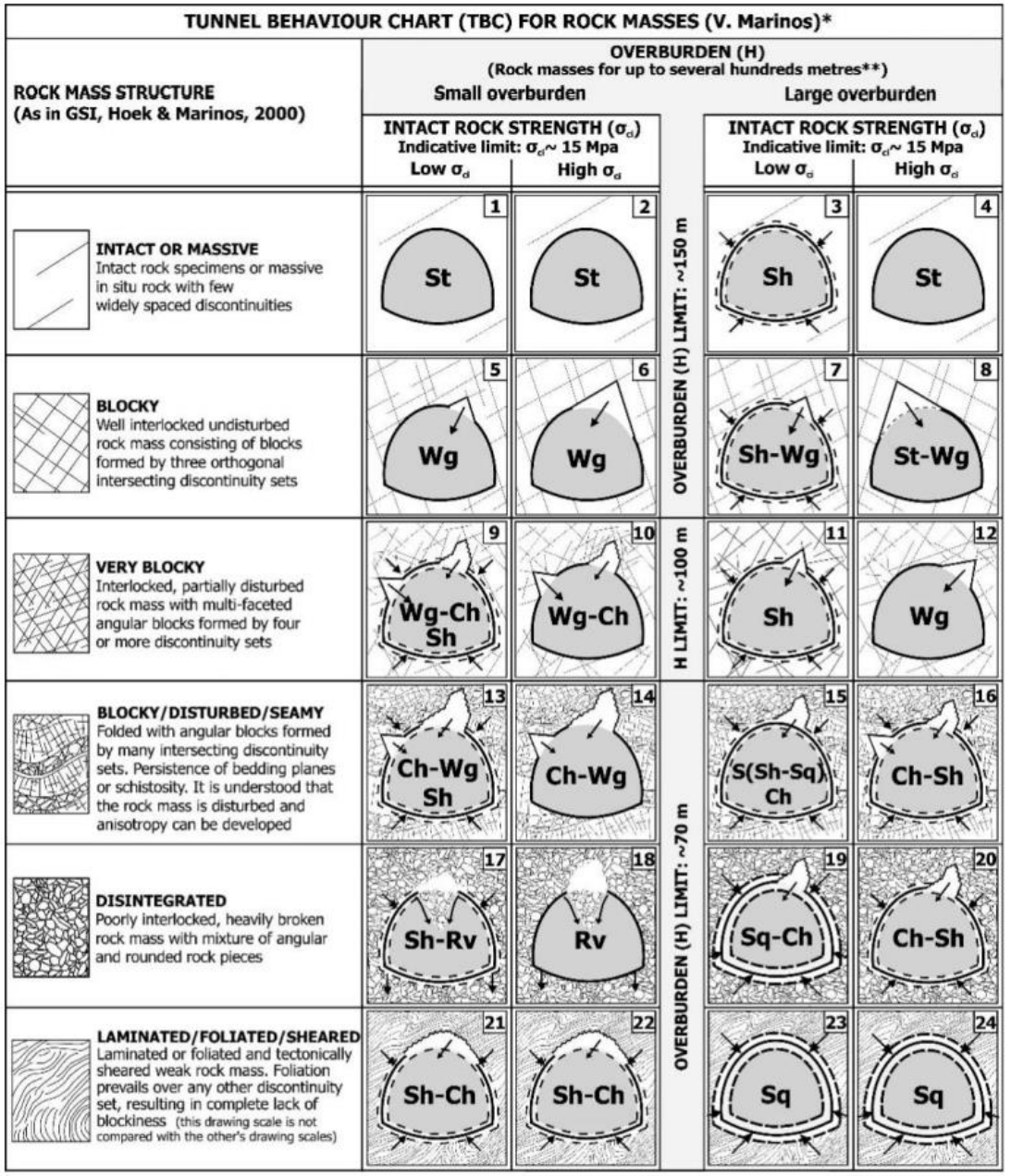

Tunnel rock mass behaviour types (St, Wg, Sh, Sq, Rv, Ch) as defined in figure 3
The engineering geological behaviour may be also controlled by two or three different mechanisms (e.g. Sh-Ch)

Notes:

*** The data used in the TBC were obtained from tunnels excavated by the conventional method with top heading and bench in a non-urban environment with the overburden cover up to several hundred metres (generally not exceeding 500m) with a tunnel diameter=12m**

****The chart does not refer to very high overburden (e.g. many hundreds of m or >1000m), where the scale and the mechanism of failure may differ**

- **The limit-ranges of the uniaxial compressive strength (σ_{ci}) of the intact rock and the overburden thickness (H) are indicative. This is done to avoid standardisation by an inexperienced user. The purpose of this diagram is to predict the failure mechanism of several common rock mass types.**
- **The surface condition of discontinuities, the second component to the GSI system, mainly affect the intensity of the failure phenomenon**
- **High clay presence along the discontinuities or zones in the rock mass may shift the gravity driven behaviour types towards the vertical axis of the chart (e.g. from Wg[9] to Ch [13])**
- **Groundwater presence mainly affects the factor of safety and not the behaviour type. Though, in some cases, such as "Blocky-Disturbed" & "Disintegrated" rock mass, the groundwater presence may "shift" a Chimney (Ch) or Ravelling (Rv) behaviour type to Flowing ground (Fl)**
- **Cases number 4, 8 and 12 may develop brittle failures (Br) when overburden increases considerably (e.g. >800 m) depending on the intact rock strength**
- **The illustrations of the tunnel are sketches; this shape corresponds to the usual top heading**

Figure 7: Tunnel behaviour chart (Marinos, 2012)

2.3 Mobile laser scanning in underground excavations

Deformations underground and the associated fall of ground are major sources of risk in mines leading to high rehabilitation costs to make the areas safe again. Therefore, during the rock engineering and excavation design, a high value is placed on minimizing potential deformations (Jones & Beck, 2017). Jones and Beck (2017) defined several methods that are used:

- Kinematic analysis, relies on structural mapping and wedge identification. From this analysis, a ground support design is engineered to support the wedge and minimise deformation.
- Empirical methods, based on generalized rock mass parameters and classifications.
- Numerical methods, best accounts for known influencing factors such as stress, adjacent faults and excavations.

The mentioned methods need a verification which can be achieved by measurements and monitoring. Options for this are (Jones & Beck, 2017):

- Instrumented ground support
- Extensometers
- Tape extensometers

The disadvantage of the methods is that discrete point-to-point measurements are obtained which are not representing the magnitude of deformation in the whole area (Jones & Beck, 2017). Tripod-mounted terrestrial laser scanners with traditional surveying techniques to determine the position are the commonly encountered method to perform underground 3D mapping. This is time and labour intensive and mapping large areas is difficult to implement (Zlot & Bosse, 2014). A subjective and error-prone method due to possible human error is damage mapping. This can cover large areas and give an insight into the deformation and rock mass changes (Jones & Beck, 2017).

New technological achievements have made LiDAR techniques applicable to detect deformations and overcome the disadvantages of previous methods. The availability of GPS in open pit mining has enabled efficient high accuracy methods to be developed to scan large areas of pits using vehicles. Through further current research, an increasing number of possibilities are being developed to enable mobile scanning in locations lacking GPS. This also includes the potential use in underground mines enabling 3D images of entire areas to be precisely scanned and compared. The scans can provide useful insights into the magnitude, direction and propagation of areas prone to deformation exceeding the ground support limits. Implementing regular scans by mobile laser scanning proved to be beneficial in mines with swelling or squeezing ground (Jones & Beck, 2017).

The first mobile laser scanners for underground use were launched in 2014, starting with the GeoSLAM Zeb-1. Subsequently, several scanners were placed on the market, such as the Mine Vision System, uGPS Rapid Mapper™, V-Scan3D, Zeb-REVO and PX-80. To enable georeferencing even without GPS, the systems make use of various methods. These range over internal measurement units (IMU), radio frequency identification (RFID) tags, stereo cameras and a second laser cameras. All scanners work with LiDAR and a SLAM algorithm (Jones & Beck, 2017).

Since underground excavations are subject to changes in stress state caused by the load distributed in the surrounding rock convergence can occur underground. Convergence is an important research field and a serious concern, causing risk to human safety, damage to infrastructure as well as production losses (Lynch, Marr, Marshall, & Greenspan, 2017). Tracking deformations regularly over a defined time period with mobile laser scanner plays major role in convergence monitoring. The tunnel can converge, diverge or remain stable during deformation (Figure 8). For convergence monitoring to work accurately, the system must be able to determine the exact distances between the two scans. This ensures that the results are representative for the real underground deformation. In practice, various algorithms have been written for this use case. Simple point-to-point calculations give fast results, but more complex algorithms that calculate the average local surface of the

first scan and calculate the vector displacement to the second scan are much more accurate and reliable (Jones & Beck, 2017).

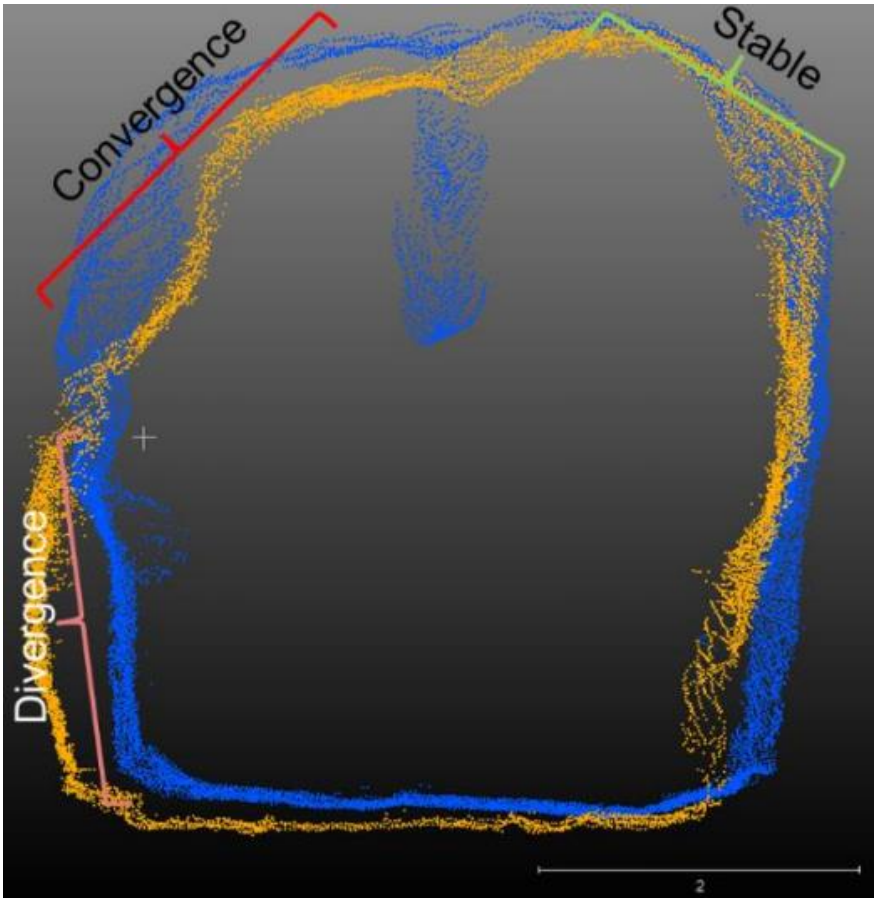

Figure 8: Tunnel cross section showing convergence, divergence and a stable area, blue old scan, yellow new scan (Jones & Beck, 2017)

Some specific application possibilities of mobile laser scanning mentioned by Jones and Beck (2017) are the analysis of convergence rates. Several applications are proposed, including:

- Assessing the effectiveness of ground support designs.
- Assessing the rock mass response of different geotechnical areas.
- The scheduling of rehabilitation to plan access restrictions in advance.
- As a warning for an excavation failure.

Mobile laser scanning in underground excavations is still under development although it has been on the market for many years and is already playing an important role in making mines safer. The scanners give engineers insights into

deformation locations and can be used to optimize support design, plan rehabilitation accordingly and identify potential rock falls earlier (Jones & Beck, 2017). As a conclusion Jones and Beck (2017) recommended using mobile laser scanning data as a conjunction to traditional measurement techniques like damage mapping instead of seeing it as a replacement for conventional techniques.

3 Research area

Areas critical for production and prone to deformation were identified before the start of the thesis work. Because of occurring deformation and other reasons some areas were permanently or partially closed during the practical part of the studies. Additionally, some developed crosscuts in PR 996 were already backfilled before extraction due to stability issues resulting in ore losses. The study area is in some parts near current mining activities and therefore, possibly more prone to deformation. The area includes access drifts as well as crosscuts in PR, HO and AL from level 996 to 1082. The three orebodies are centrally positioned and are merging into a 2 km long orebody at a depth of about 1000 m. Weaker zones are common between the contact zone of the ore and the host rock in the footwall, due to biotite schist occurrence. The mining advances in these orebodies by the development of a series of drifts at the footwall with perpendicular crosscuts. Every crosscut is separated into several subvertical blast rings drilled into the roof that undercut the ore. The production is conducted on multiple sublevels concurrently and the blasting, caving, loading and hauling causes a stress redistribution leading to possible deformation nearby. However, the development step of entries and crosscuts must be conducted long in advance due to high stresses and the large scale of mining (Jones, Nordlund, & Wettainen, 2019). This results in standing times of a few years before production starts. The footwall drive is farther away than the standard 20 m from the last ring because of the biotite schist occurrence along the footwall contact zone. This measure ensures minimized exposure to the poor geotechnical conditions by driving the crosscuts straight through the weaker biotite zone (Jones, 2018).

Printzsköld:

The PR orebody is one of the larger orebodies of the mine. Strike is about 40° north with a dip of approximately 60° southwards. The average thickness of the orebody is

50 m and mining started at level 780. Current mining operations are active at level 996 and 1023. Figure 9 shows a typical layout in PR.

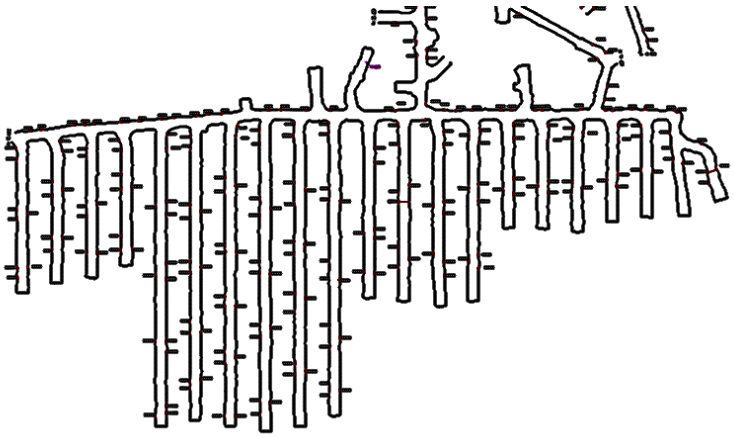

Figure 9: Typical layout of the PR orebody (Winsa, 2017)

Scanning area involves:

Table 5: Scanning area in PR

Orebody	Level Number	Crosscut Number
PR	996	4090
PR	996	4110
PR	996	Footwall drive 2530-3850
PR	1023	4060
PR	1023	4080
PR	1023	4100
PR	1023	Footwall drive 4000-4140
PR	1051	4070
PR	1051	4090
PR	1051	4110
PR	1051	Footwall drive 4030-4130

For convenience reasons during the scanning procedure long footwall drive scans such as the one in PR 996 are divided in parts. For instance, 996 is divided in three parts and it proved to be practical, because the first part from crosscut 2530 to 2370 was sometimes closed. Initially, PR 996o4070 and PR 1023o4040 were also assigned

as research area but were removed prior to the scanning start. Other areas were mainly open, so enough data could be gathered.

Alliansen:

AL is also one of the larger orebodies of the mine. The average thickness is as well 50 m. It strikes east to west and has a dip of 60° southwards. The orebody is the only one in the eastern part with small amounts of hematite besides the dominating magnetite (Jones, Nordlund, & Wettainen, 2019). Production in the orebody is already deeper than in PR at about level 1080.

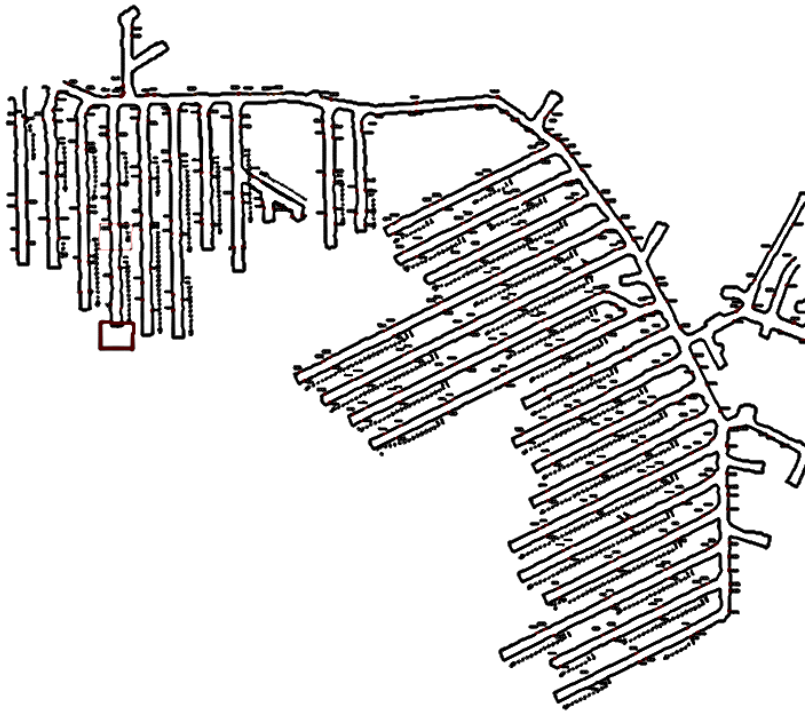

Figure 10: Typical layout of the AL orebody (Winsa, 2017)

Figure 10 shows a typical infrastructure layout in AL. The research area is mostly in the western part of the orebody adjacent to HO. Scanning area involves:

Table 6: Scanning area in AL

Orebody	Level Number	Crosscut Number
AL	1052	2790
AL	1052	2810

AL	1082	2780
AL	1082	2800
AL	1082	2820

Hoppet:

The HO orebody is located between the two other orebodies and is smaller. The average thickness of the orebody is also about 50 m and the average dipping is approximately 60° southwards. Production advances concurrent to AL and is on level 1080.

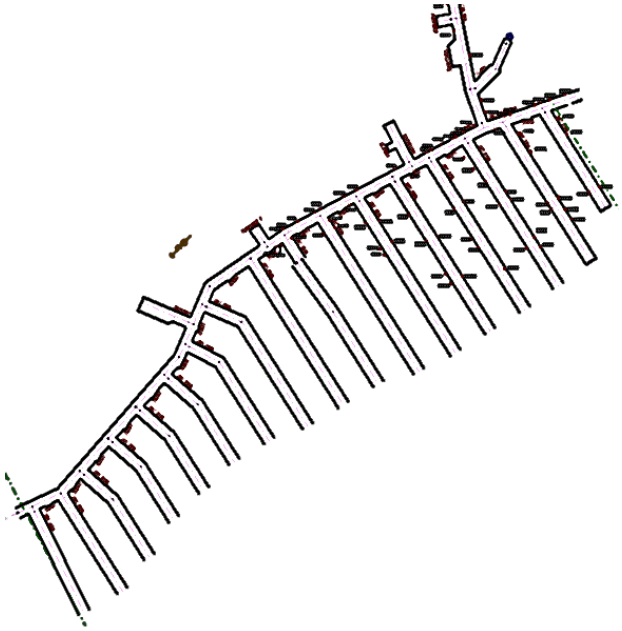

Figure 11: Typical layout of the HO orebody (Winsa, 2017)

Figure 11 shows a typical layout in the HO orebody. Scanning area involves:

Table 7: Scanning area in HO

Orebody	Level Number	Crosscut Number
HO	1023	2640
HO	1023	2680
HO	1023	Footwall drive 2660-2760
HO	1051	2550 (closed since 21.02)
HO	1051	2570 (closed since 10.03)
HO	1051	2590 (closed since 10.03)

HO	1051	2730
HO	1051	2750
HO	1051	2770
HO	1051	Footwall drive 2470-2830
HO	1080	2740
HO	1080	2760
HO	1080	Footwall drive 2620-2820

The footwall drive scans in HO 1051 and 1080 are starting in the AL orebody. In the western part of HO a lot of areas were closed during the scanning time. In 1023 the crosscuts 2520 to 2560 including the footwall drive were closed. Due to seismic events, closure in HO 1051 progressed during the field work, 2530 was all the time closed followed by 2550 to 2590 as well as the including footwall drive.

3.1 Geotechnical characteristics

The geological data is taken from previous research in the orebodies by Granljung (1999) and Magnor (2007), internal records and investigations in the mine. The study area is characterised by different rock types:

The red leptite is fine to medium-grained and consists of kali feldspar and quartz. Additionally, plagioclase, biotite, amphibole and pyroxene occur. The biotite content increases closer to the ore body. The rock type is mainly found in the hanging- and footwall.

The grey leptite is fine grained and can contain in some parts large biotite concentrations that occur layered with other mafic minerals. It is mostly found as inclusion in the ore rock.

The red-grey leptite is defined by a higher content of mafic minerals than the red leptite. These rock types are commonly found in close contact with the ore rock in the hanging- and footwall.

Medium-grained granite mainly consisting of quartz, kali feldspar, plagioclase and biotite is also abundant. In the upper parts of the orebody there are areas with heavily weathered granites.

Biotite schist occurs in a layered structure and is the weakest unit compared to the other rock types in the mine.

To take the rock mass properties into account the geological strength index (GSI) value which is describing the present rock structure from internal records of all three orebodies is considered (Table 8).

Table 8: GSI values for rock types in research area

Rock type	GSI range
Red leptite	60-80
Grey leptite	60-75
Red-grey leptite	65-75
Granite	50-60
Biotite	20-55
Magnetite	50-70
Hematite	50-65

Furthermore, intact rock parameters are taken into account like the uniaxial compressive strength (UCS) and uniaxial tensile strength (UTS), which were determined from mainly the Brazilian test in the AL orebody (Table 9). Nordlund (2013) defined three different biotite zones, the weakest being adjacent to the ore with a typical distance of 0.5-5 m and a thickness of 0.5-5 m. The second biotite zone is in a distance of 5-20 m to the ore contact and shows a thickness of 5-10 m. Biotite 3 is 20-50 m away from the contact zone with a thickness of 20-30 m. The different biotite zones show the weakest geotechnical properties in the system (Nordlund, 2013).

Table 9: Intact rock parameters in research area (Basarir, 2012) (Nordlund, 2013)

Rock type	UCS (MPa)[a]	UCS (MPa)[b]	UTS (MPa)[a]	UTS (MPa)[b]	RMR[b]
Red leptite	167-267	-	11-18	-	-
Grey leptite	72-88	-	7.8-9.2	-	-
Red-gey leptite	116-237	-	8.2-13.8	-	-
Biotite 1	40-60	5-30	-	0-5	35
Biotite 2	90-100	30-50	-	5-10	40
Biotite 3	-	50-80	-	10-20	45
Magnetite	92-108	-	5.0	-	-

[a] Basarir 2012

[b] Nordlund 2013

The primary stress in the Malmberget mine was analysed in different studies (Nordlund, 2013). Sandström and Nordlund recommended following equations for the magnitude and orientation:

- Max horizontal principal stress:

$$6_H = 0.037 \times z\,[MPa], orientation\ (east\ to\ west) \quad (4)$$

- Min horizontal principal stress:

$$6_H = 0.028 \times z\,[MPa], orientation\ (north\ to\ south) \quad (5)$$

- Vertical principal stress:

$$6_V = 0.029 \times z\,[MPa] \quad (6)$$

Hydraulic fracturing was done in 2007 in the mine. Table 10 shows the results of it.

Table 10: Primary stress magnitudes and trends (Ask, et al., 2009) (Sjödberg, 2008)

Cluster	Level (m)	$б_H$ (MPa)	$б_h$ (MPa)	Trend of $б_H$	Trend of $б_h$
1	1170	49.6	23.9	128	38

2	1300	40.8	22.1	137	47
Mean value		45.2	23.1	132	42

3.2 Tunnel support practises

This subsection deals with the applied support practises and the ground support control management plan of the mine to ensure a safe and on-going production underground. Therefore, information is derived from Jones (2018), Winsa (2017) and own work in the research area.

The Malmberget mine, in particular the primarily responsible rock mechanics department, has a well-structured ground control management plan regarding the underground excavations.

The support is linked to the expected life of the excavation, the expected purpose of the opening and the geologic conditions. Geologic models and mapping help to determine areas with unfavourable geology, which are supported more extensively. The present geology is the most important parameter in regard of which type of support is installed. The ground support is divided into standard reinforcement classes to provide traceability, increased security as well as the opportunity to check the reinforcement function. These classes represent the minimum level of support needed to be installed. Thus, given locations may need additional support in poorer rock conditions or new applications. The main objective of the ground control management plan is to ensure the safety of all people, equipment and production underground from a rock mechanical perspective.

By using patterned bolting, the inner cohesive force and strength of the rock are utilized to lock the rock pieces in place. To support the surface sprayed fibrecrete and welded wire mesh is used. Meshes are optional and are used to stabilize falling rock as well as to transfer the load to the anchored bolts. The development cycle that leads to the safe support of the rock includes the following steps:

- Loading
- Scaling to remove loose rock

- Washing to remove dust and ensure fibrecrete adhesion
- Application of fibrecrete
- Installation of rock support

There are five support classes based on geologic conditions and stress situations (Table 11). Class four and five are specially designated to risks by seismic events and exceptionally difficult rock conditions.

Table 11: Support class by rock or risk type

Support Class	Rock/Risk Type
Class 1	Red leptite (in crosscuts, exclusive footwall drifts), magnetite and hematite
Class 2	Grey, grey-red and red-grey leptite with no, little or moderate extent of biotite
Class 3	Massive biotite schists or leptites with high level of biotite
Class 4	Risk of rock falls caused by seismic events
Class 5	Severe rock conditions, such as clay zones

The support classes are defined by a nomenclature with a series of letters and numbers indicating the support type, fibrecrete thickness, primary bolt type, bolt spacing and the usage of additional support like wire mesh and cable bolts (Table 12). Table 13 shows the minimum requirements of the five support classes.

Table 12: Nomenclature for support types. Example of M7-D1.5-NKa

Reinforcement type	Fibrecrete thickness	Bolt type	Bolt C/C	Other
M	7 cm	D	1.5 m	N Ka

Table 13: Recommended support for support class

Support Class	Class code
Class 1	M7-S1.5-0 or M7-Ki1.5-0
Class 2	M7-S1.5-0 or M7-Ki1.5-0
Class 3	M7-D1.0-N

Class 4	M10-D1.0-N
Class 5	According to Rock Mechanics

The nomenclature can be broken down as follows:

- Reinforcement type:
  - K: Kiruna
  - M: Malmberget
  - X: Customized
- Fibrecrete thickness:
  - 0: No fibrecrete
  - 7: 70 mm fibrecrete
  - 10: 100 mm fibrecrete
- Bolt type:
  - R/Ki: Rebar bolt
  - F: Friction bolt
  - D: Dynamic bolt
  - S: Coated friction bolt
  - 0: No bolt
- Additions:
  - N: Steel mesh
  - Ka: Cable bolt
  - NKa: Mesh and cable bolt
  - B: Fibrecrete reinforcing arches
  - 0: Nothing

Areas with a longer life span than cross sections such as ramps, access routes and footwall drifts should be reinforced with a method that uses cement or resin-anchored bolts. Areas with a 4-way intersection or a theoretical span above 9 m also should be reinforced with additional measures including cable bolts with a length of at least 7 m.

Reinforcement arches do not exist as part of any reinforcement classes but are extra support on an as-needed basis. In the research area several arches were constructed to support the stability in crosscuts and ensure a safe extraction. The arches are consisting of fibrecrete with a possible inner reinforcing mesh. In total, there are four types (Table 14).

Table 14: Nomenclature and description of fibrecrete arches

Designation	Description
B1	Arch with 200 mm fibrecrete
B2	Arch with 200 mm fibrecrete, including ring of bolts/cable bolts, 1 m c/c spacing
B3	Arch with 200 mm fibrecrete, including inner reinforcing mesh and bolts/cable bolts with 1 m c/c spacing
B4	Arch with bolts/cable bolts with 0.5 m c/c spacing

The basic support installation as well as the additional support is in some cases a flexible process, but important rules must be followed. For instance, the mesh must be bolted close to the corners and adjacent meshes must overlap by at least three mesh boxes (Figure 12).

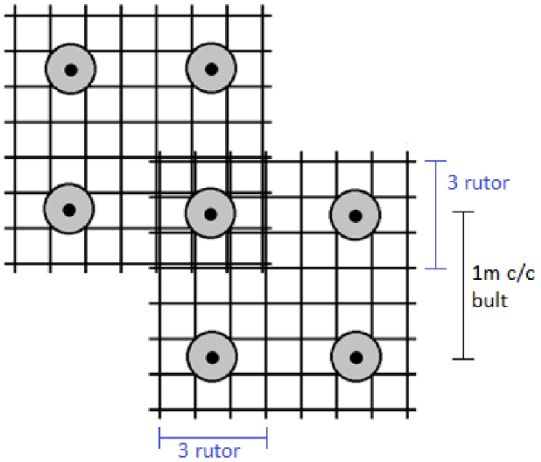

Figure 12: Sketch of minimum overlap of adjacent meshes with 1m c/c bolt spacing (Winsa, 2017)

In zones were rock fall has a higher probability by seismic events, the matching support class must be applied within two rounds of lag-time and in general also before production loading begins on the level above. Also, rock mechanics can require that the reinforcement should be installed earlier, this would be then noted in the development restrictions. In cases of poorer rock conditions than expected a more suitable support class can be applied by the development coordinators, who

are responsible to update the rock reinforcement plan accordingly. Additionally, bolters can install extra bolts if they consider it to be required without approval.

In the opposite case, when the rock conditions are better than expected and a less extensive support class can be applied, the operational rock mechanics must be contacted for further assessment. This decision can only be made by the operational rock mechanics. Updates regarding the support classes or alternative approaches can be made through a discussion of the operational and research and development rock mechanics.

All support types must meet certain needs, such as long-term durability, durability, toughness, tensile strength, loading capacity, energy absorption and others. This is controlled through different approaches. The fibrecrete is controlled through the whole production process to ensure its strength and quality. Also, the thickness is controlled underground to ensure adequate work. If the surface support is not thick enough, the aerial extent must be analysed to respray the area. The mesh is controlled by the supplier's quality control and the documentation is available for LKAB. With the rock bolts delivered by two suppliers, it is similar. Additionally, 1 % of all bolts installed are pull-tested to ensure that the required parameter is met. If that is not the case, the aerial extent must be determined to bolt the area again.

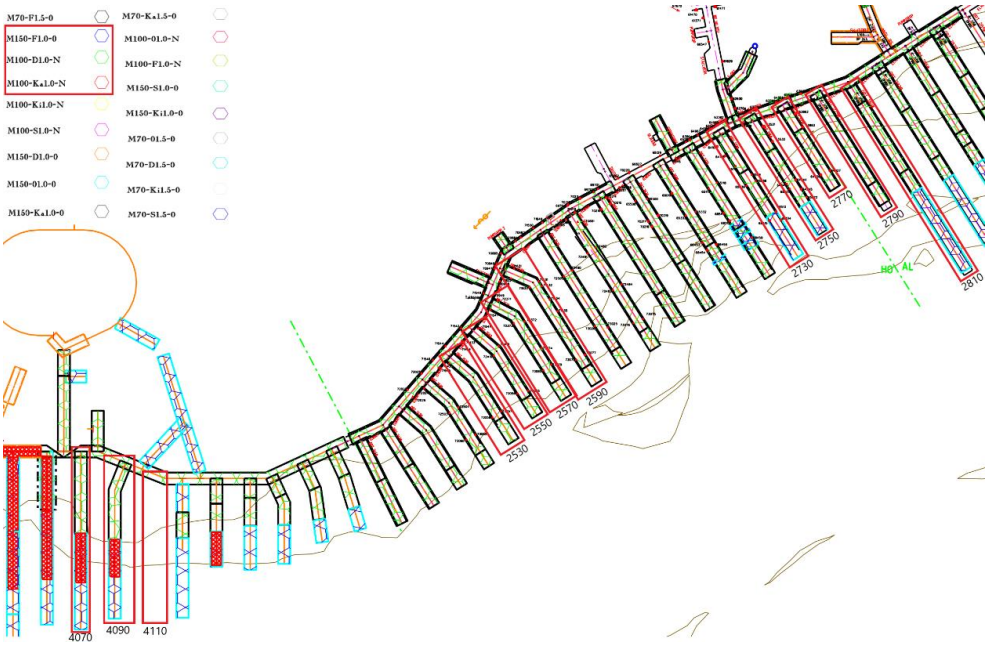

Figure 13: Support classes in the research area at Level 1051 and 1052 with marked crosscuts (MicroStation V8i)

Figure 13 shows representatively the support classes in the research area on level 1051 and 1052 of the three orebodies that are merged to one at that depth. More detailed maps of the different levels and the research area can be found in Chapter 4. The common support in the research area is a 100 mm fibrecrete layer with dynamic bolts of a spacing of 1.0 and an additional mesh, represented by a green signature. This corresponds to the support class four for areas that are prone to rock fall due to seismic activities. In some crosscuts 150 mm fibrecrete with friction bolts of a spacing of 1.0 m is installed. This is shown by a blue signature. In the PR orebody some areas are supported through a 100 mm fibrecrete layer, cable bolts with a spacing of 1.0 m and a mesh.

Fibrecrete arches are also used locally in crosscuts. For instance, in PR996o4110 twelve fibrecrete arches are installed (Figure 14). Also, in other areas such as HO and AL from level 1023 to 1080 a number a fibrecrete arches are installed. In total the research area has more than 50 fibrecrete arches as an additional support measure. A more detailed description of the current conditions is in Chapter 4.

Figure 14: Crosscut PR996, 4110 with installed fibrecrete arches

4 Current state of openings

The chapter is divided into the three orebodies and deals with the current conditions of the research area. The main focus is on parameters which can influence the deformation and describing deformation that has already occurred. For this, data from damage mapping, wall-to-wall distance measurements and floor heave measurements of a part of the research area as well as internal records and own field observations are available.

4.1 Printzsköld

In PR 996 drift 4090 and 4110 are of central interest (Figure 15). In 4090, floor heave measurements as well as convergence measurements are available by previous researches. Additionally, there are geological records and own observations from field work given.

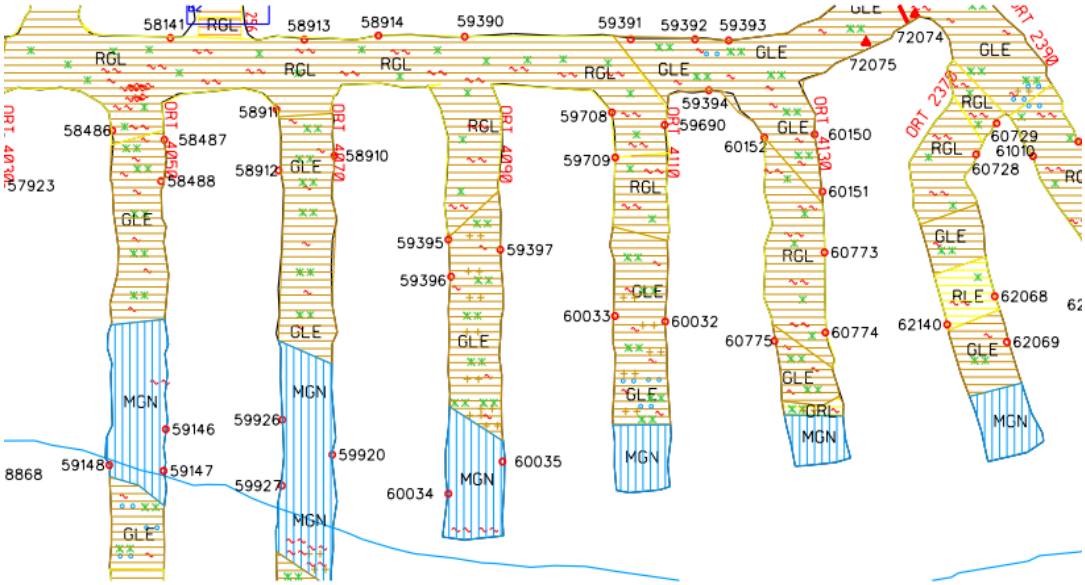

Figure 15: Layout of PR 996 with geological features (MicroStation V8i)

Figure 16: Current state of PR 996o4090 drift

Figure 15 shows red grey leptite at the beginning of the drifts followed by grey leptite and magnetite. Both leptites have homogeneous intrusions of granite and skarn with the grey leptite having a higher content of biotite. Both drifts show a similar geology.

Figure 16 shows 4090 as of section four, the area with the most visible changes and impact. Most activity occurs between sections four and seven, with section five appearing to be the most active area. In section seven the orebody starts, so the most active area is defined by grey leptite with a higher biotite content (Figure 15). Many of the bolts in the area are loaded and there are many fibrecrete flakes in the shoulders and roof held by the mesh. On the lower left wall, the fibrecrete has cracked and fallen off under the mesh. This has revealed loose pieces of rock. The

rock sample shows biotite from the cracked lower left wall in section five. The piece is easily breakable and has a high mafic content. In general, it looks like the left side of the drift is more prone to deformation.

Figure 17 shows the wall-to-wall distance over six months in the drift for different sections which is measured manually with a laser range finder. Positive values represent divergence and negative values represent convergence compared to the first. The measurement series had already started before the project. Within six months the distance decreased by 0.15 m for section five and six at a regular and ongoing pace. In section three there was an increase of 0.1 m in the first three months, but nothing happened in the following three months. The measurements fit the field observations.

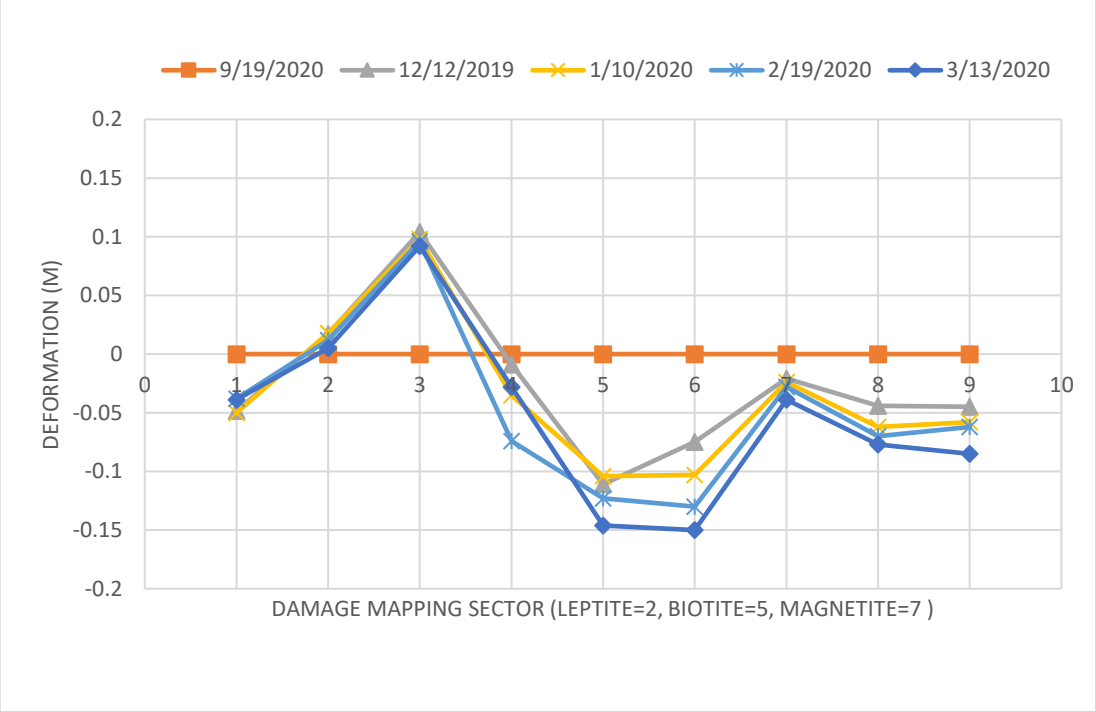

Figure 17: PR996o4090 Wall-to-Wall Convergence/Divergence (by Jones, 2020)

In 4110 twelve fibrecrete arches were installed to stabilize the drift and keep it open until extraction (Figure 14). Beyond the fibrecrete arches, the tunnel appears more deformed. Also here are flakes of fibrecrete in the shoulders and roof which are concentrated in the area from the grey leptite to the ore contact zone. Furthermore, the concrete and fibrecrete arches are wet as can be seen in Figure 14.

In PR 1023, drift 4060, 4080 and 4100 are designated as research area (Figure 18). In all drifts, floor heave measurements by previous work as well as geological records and own observations are given. Additionally, wall-to-wall distance measurements in 4080 were gathered in earlier rock mechanical works. All three drifts start with grey red leptite with skarn and granite intrusions. In 4060 the rock type continues to the orebody with no marked intrusions of biotite. The GSI-value is 35-55. In 4080 and 4100 grey leptite with intrusions of granite, skarn and biotite is present. Here, the leptites have a GSI-value of 25-45 and especially in the ore contact zone the rock is weak with a GSI-value of 30, poor surface conditions and a disturbed structure with many intersecting discontinuity sets.

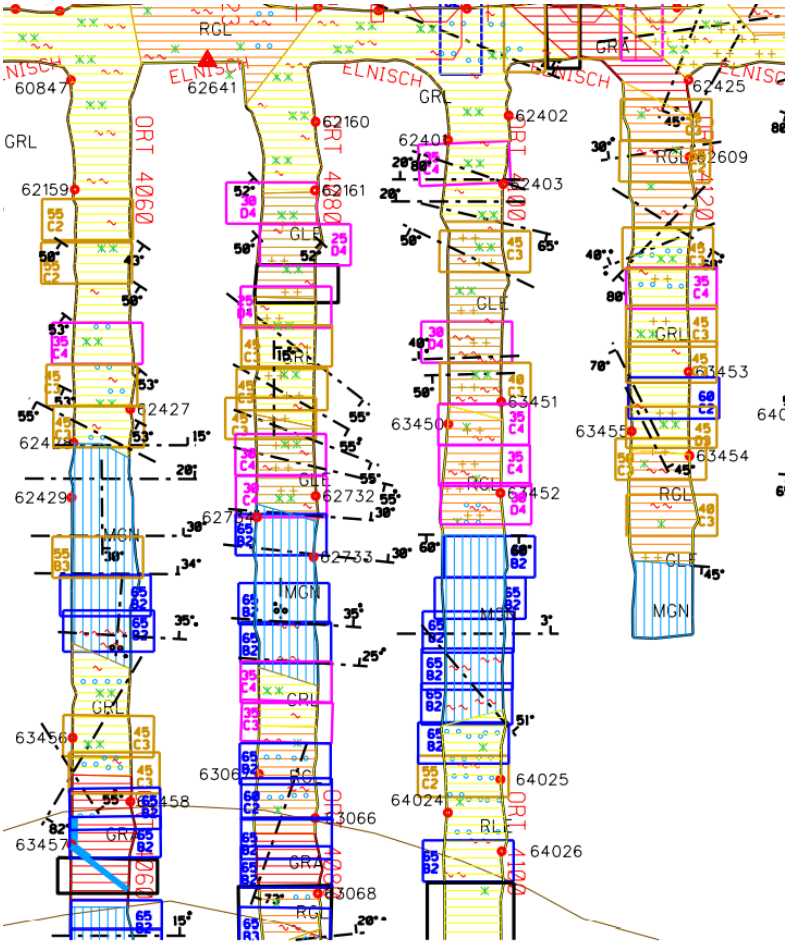

Figure 18: Layout of PR 1023 with geological features (MicroStation V8i)

Figure 19: Current state in PR 1023o4080, cracks marked in red (by Jones, 2019)

Especially in 4080 in section six and seven deformations are recognizable. The walls, shoulders and roof have a lot of cracks and the floor is bulging in the area, but also section four and five show changes due to deformation. Figure 19 is from previous research and the pictures were taken before the mesh was installed. It shows the cracks in the fibrecrete marked by red spray paint to make progressive damage easier to detect. However, it was also evident during own observations that there are many cracks and the area is active. Unfortunately, 4100 was closed during the mapping day, so more accurate data could not be collected. This would be very interesting, as the

drift has a similar structurally weak area at the ore contact zone like 4080. Drift 4060 is in slightly better condition but also shows cracks and moisture in front of the magnetite.

Figure 20 shows the wall-to-wall distance over three months in drift 4080. Within three months the distance decreased by 7 cm in section six, by 6.5 cm in section seven and by 5 cm in section 9. The remaining areas show a slight deformation of less than 3 cm. It seems as if the rate of deformation is decreasing, but the changes are continuing. The wall-to-wall distance readings match well with the geologic map and the field observations because there are many damages and the rock mass has a lower GSI-value in the area from section five to eight.

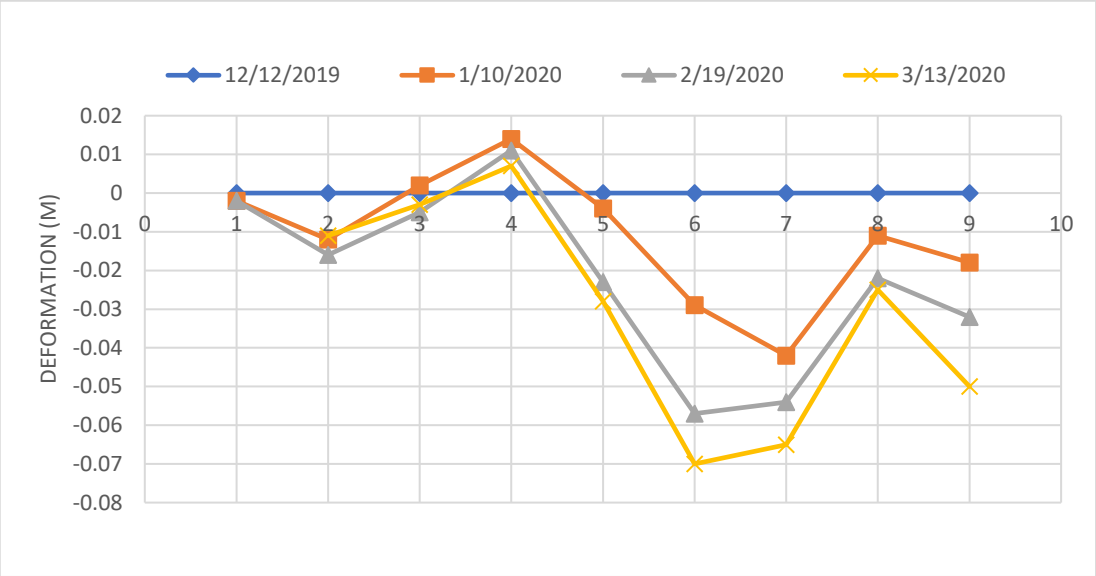

Figure 20: PR1023o4080 Wall-to-Wall Convergence/Divergence (by Jones, 2020)

In January of 2020 the floor heave in different drifts was investigated. For this purpose, the elevation of the floor was measured every 5 m and visualized accordingly (Figure 22). In theory, the drifts are developed with a slope of 1:50. It can be seen that in the first part from point one to five the slope of the drifts are close to the planned one (Figure 21). In 4080 and 4100, a higher slope is visible between point six and seven, which decreases afterwards. It is known that in 4080 the floor was completely cleaned to level it, which means that the real heave is higher than shown here. 4060 does not show such a distinctive slope change.

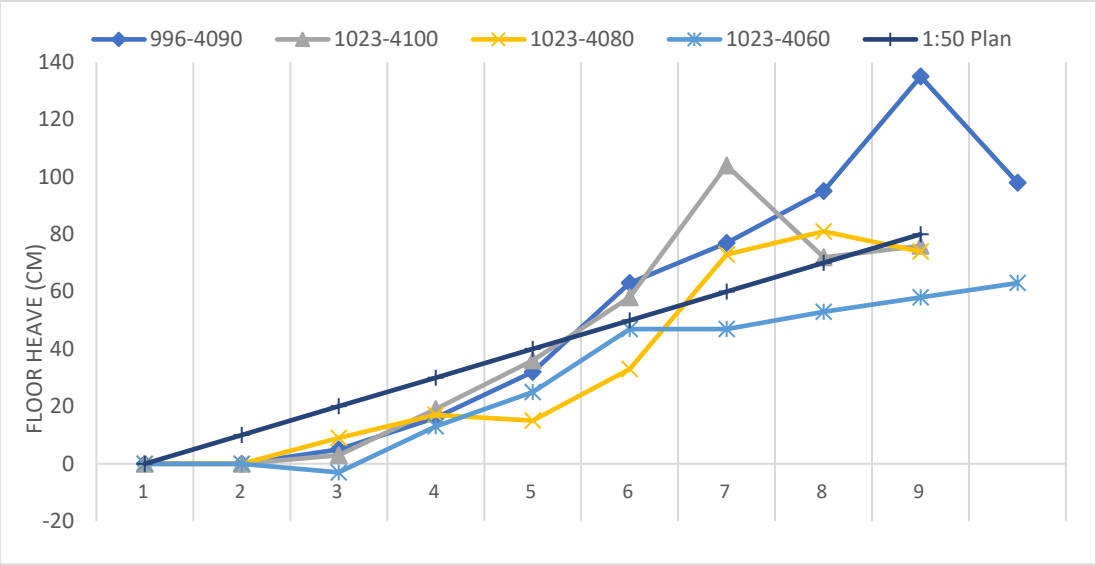

Figure 21: Floor heave in PR 996 & 1023 (by Jones, 2020)

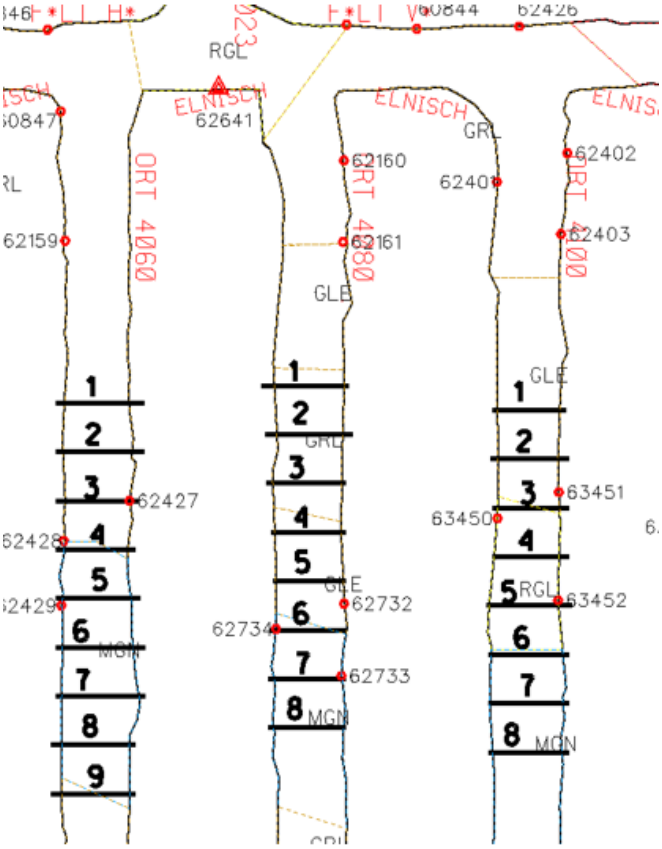

Figure 22: PR 1023 measurement profile for floor heave investigation (by Jones 2020)

In PR 1051 drift 4070, 4090 and 4110 are a part of the research area. There is no data of previous work here. The level shows little deformation compared to the two levels above. Drift 4070 is a good reference for all the drifts in the research area of PR 1051 (Figure 23). The drift perimeter has not changed much and the fibrecrete on the lower walls does not show any weaknesses.

Figure 23: Current state in PR 1051o4070

Figure 24 shows the rock types as well as the GSI-values in PR 1051. All three drifts are starting with red grey leptite and a transition to grey leptite. In drift 4090 and 4110, there are biotite schist parts in the leptite close to the orebody that have a low GSI-value of 20-35 with fair to poor surface conditions and a disturbed structure resulting in a decreased interlocking of rock pieces. The other parts in the area are defined with a GSI-Value of 45-65, good to fair surface conditions and a better interlocking of rock pieces.

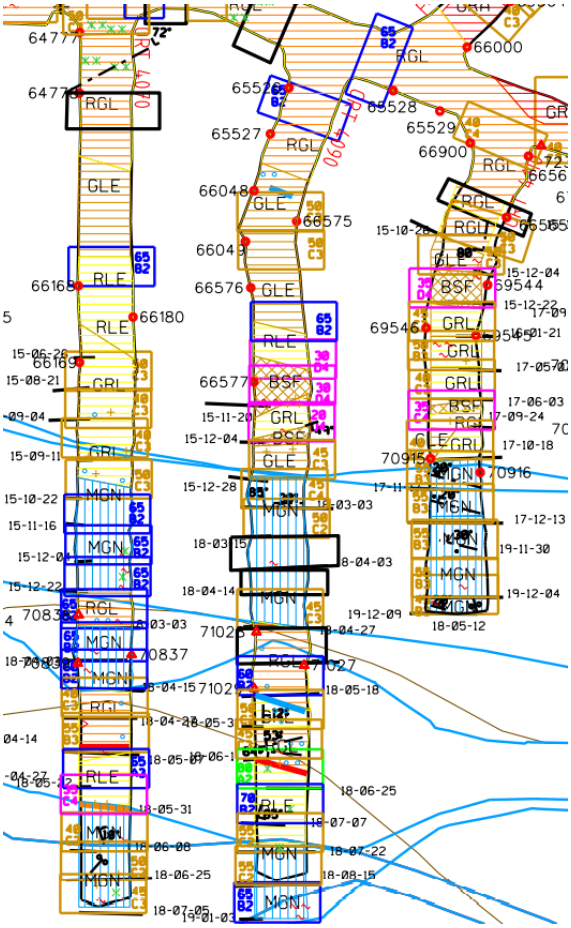

Figure 24: Layout of PR 1051 with geological features (MicroStation V8i)

4.2 Hoppet

In HO 1023 drift 2640 and 2680 are of central interest (Figure 25). In both drifts, the information is limited to geological records and own observations. Biotite schist occurs massively and more often in both drifts than in drifts in PR. The unit has a GSI-value of 10-15 with very poor surface conditions and a poorly interlocked, heavily broken rock mass. Also, the magnetite has a relatively low GSI-value with 20-35 in wide areas and is defined by poor surface conditions. In general, it seems like the area is poorer interlocked and prone to deformation.

Own field observations show that in 2640 over twenty shotcrete arches were installed, but deformation continues to progress. Some arches have small cracks in the shoulders and the surface is wet. In drift 2680, one can see that the roof is

buckling downwards, and a large longitudinal crack is advancing towards the shotcrete arches (Figure 26). The arches are heavily deformed and have cracks in the shoulders. The area is closed to entry due to seismicity and large deformations and is no longer accessible. Furthermore, there is an accumulation of water on the floor in front of the arches.

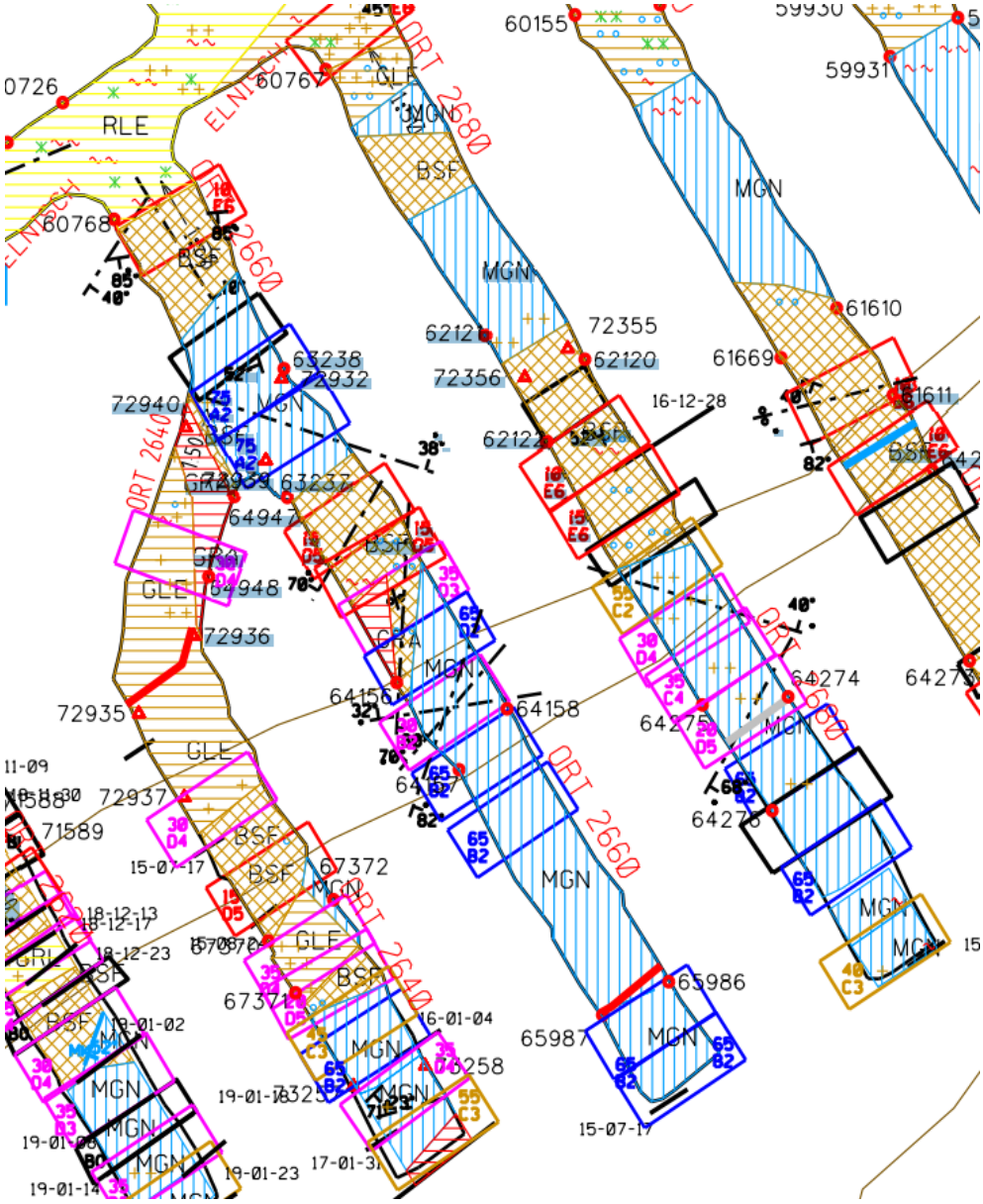

Figure 25: Layout of HO 1023 with geological features (MicroStation V8i)

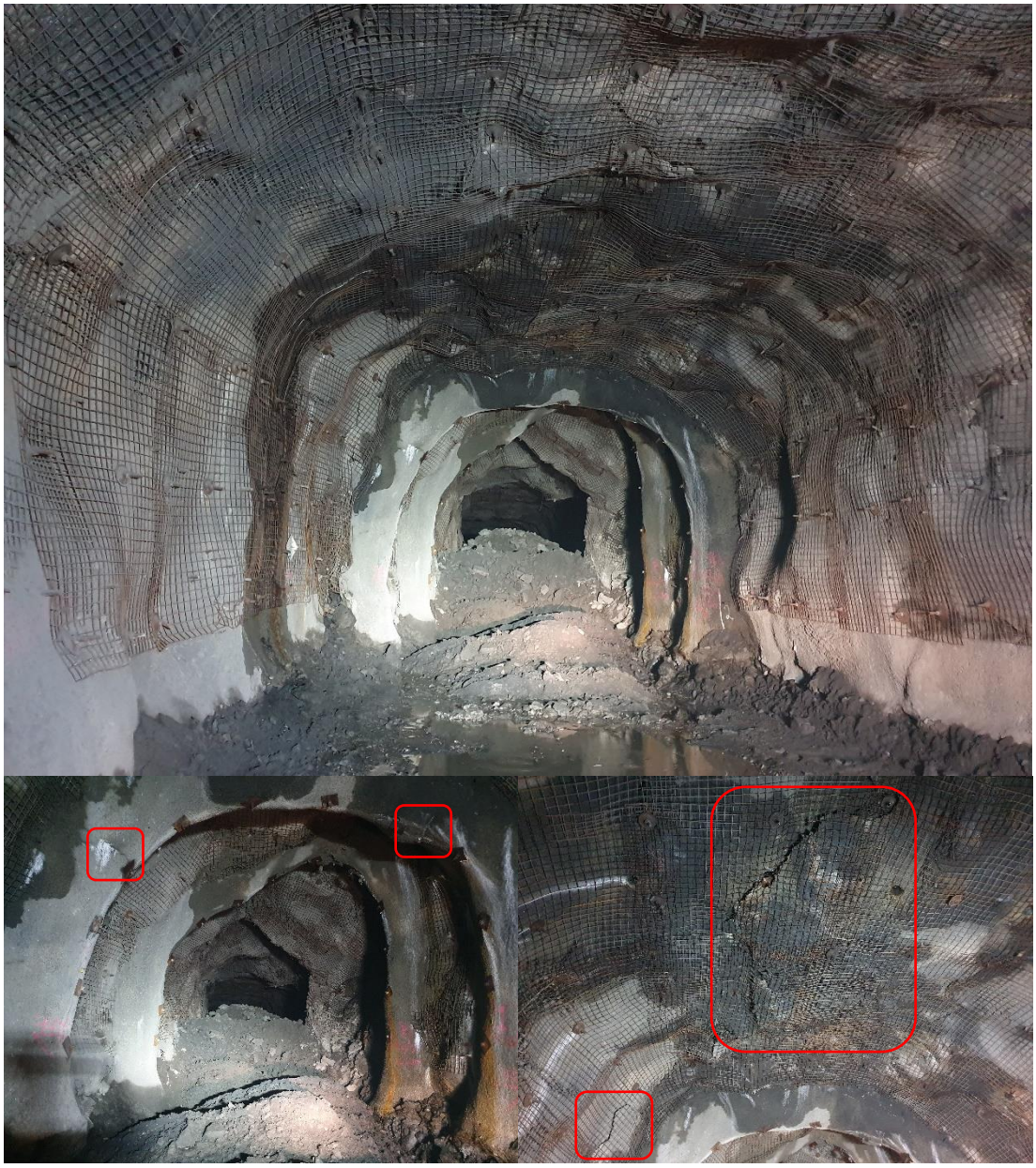

Figure 26: Current state in HO1023o2680, rectangles show cracks in roof as well as on arches

In HO 1051 drift 2730, 2750 and 2770 are part of the research area (Figure 27). In all drifts, geological data and own observations are given. Drift 2730 and 2750 consist of red leptite with granite and skarn intrusions at the entrance. Biotite schist lies between the red leptite and the orebody. In 2780, the drift starts immediately in biotite schist and the ore body that follows. The biotite schist has a typical GSI-value of 30 with poor surface conditions and blocky to disturbed rock pieces, whereas the rest of the area has a GSI-value of 50-65.

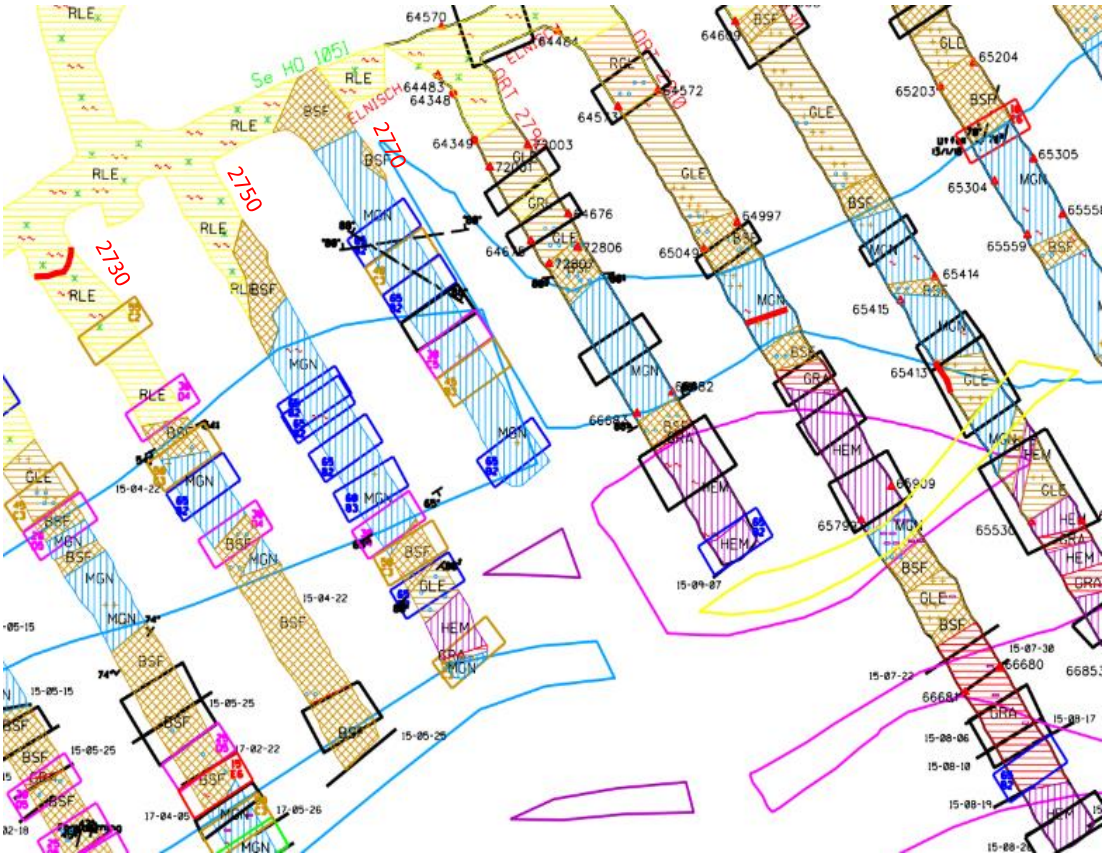

Figure 27: Layout HO 1051 & AL 1052 with geological features (MicroStation V8i)

In 2730 there are more than six shotcrete arches and a possible floor heave 5 m after the end of the ventilation hose (Figure 28). Behind it there is water on the floor and in front of it are almost no detectable cracks and other changes. The area behind the floor heave shows characteristics that indicate deformations such as loaded bolts, cracks in the fibrecrete up to the loosening of it resulting in the rock being visible. The exposed rock formation shows a loose biotite with many spaced joints. The taken rock sample can be pulverized in one hand and appears very weak. 2750 has five shotcrete arches and no visible floor heave. The zone looks a little better but also has several cracks. Although there is biotite schist at the entrance in 2770, which should make it more unstable, the drift looks better than the other two.

Figure 28: Current state in HO1051o2730

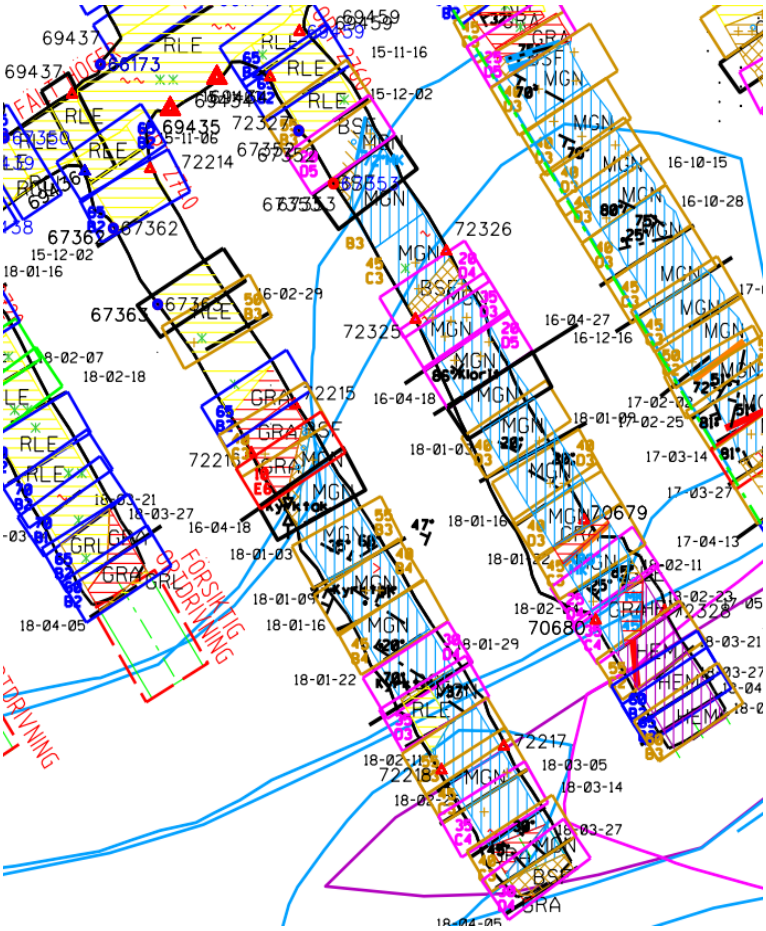

Figure 29: Layout of HO 1080 with geological features (MicroStation V8i)

Drift 2740 and 2760 in HO 1080 are also designated as research area (Figure 29). In 2760 wall-to-wall measurements are given by earlier research. Additional information came from own field observations and geologic records. Both drifts start with red leptite. In 2760 the orebody is closer to the entrance. At the ore contact zone there is a thin biotite schist formation which occurs also more common in the magnetite for the first time. The schist has a GSI-value of 20-35 with poor surface conditions. Due to the intrusions, the magnetite is also weaker with a GSI-value of 40. The magnetite in 2740 can be characterized as similar. The difference is that in 2740 granite and a weaker biotite schist with a GSI-value of 10 and very poor surface condition at the ore contact zone is abundant. 2740 looks a little different compared to the other drifts (Figure 30). There are two large rock falls and therefore two holes

Figure 30: Current state in HO 1080o2740

in the roof. Up to the first hole in the right roof, there are hardly signs of deformation in the drift. From that point on the walls are wet in some points like next to the rock fall on the left side and in front of the second rock fall which is located close to the end of the drift. On the lower right wall at the level of the first hole fibrecrete has fallen off and the rock is showing through. The outcropping rock has a very fine schistosity and falls off at the slightest touch. In 2760 a lot of cracks can be detected as well as water. The conditions are close to 2740, but without the rock falls.

Figure 31 shows the wall-to-wall distance over three months in drift 2760. Within three months the distance decreased by 1.4 cm in section one and by less than 1 cm in section four and five. The remaining areas show a slight deformation of less than 4 mm. In this scale, the accuracy of manual measurement with a laser range finder can be questioned. Even if the values were accurate, the distance differences would be acceptable.

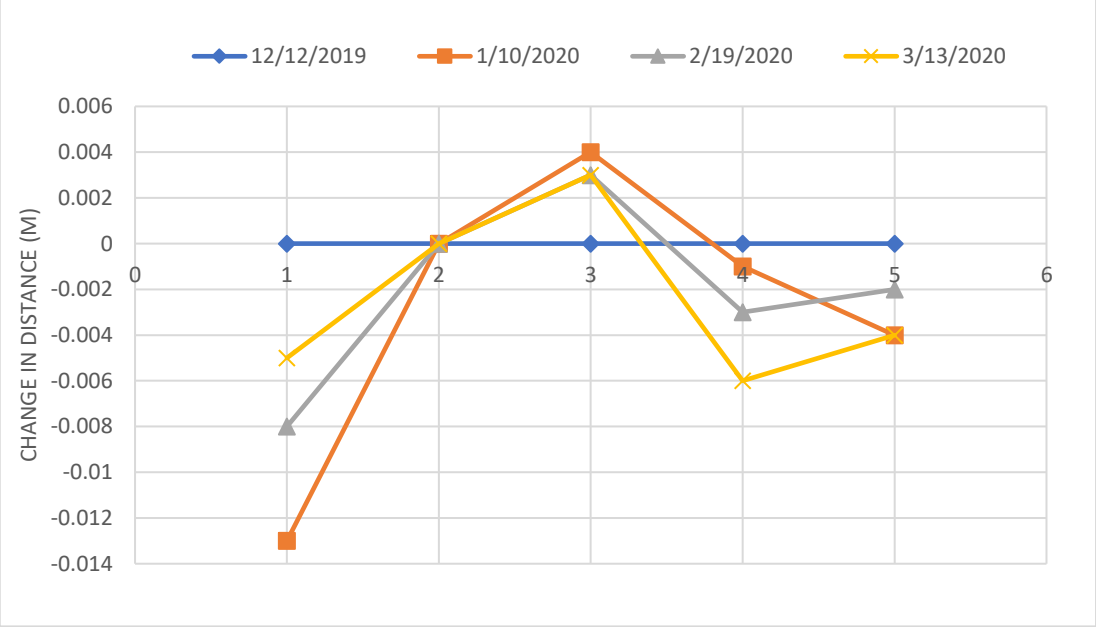

Figure 31: HO1080o2760 Wall-to-Wall Convergence/Divergence (by Jones, 2020)

4.3 Alliansen

In AL 1052 drift 2790 and 2810 are a part of the research area (Figure 27). Here own observations and internal records are available. Both drifts start with red leptite with

intrusions of skarn and granite and show, like in HO 1051, a biotite shist formation at the ore contact zone. The drifts are developed till the hematite orebody and have biotite shist between the magnetite and hematite.

2790 has six shotcrete arches to stabilize the area. There is water between arche four and six, but there are no other irregularities. In 2810 there are five shotcrete arches. Arche two has a large crack on the left side and arche four has one on the right shoulder. There is also a large crack in front of the first one. The beginning of the tunnel seems to be in better condition. 2790 looks better compared to 2810.

Figure 32: Current state in AL1052o2810

In AL 1082 drift 2780, 2800 and 2820 are designated as research area (Figure 33). In 2780 and 2800 wall-to-wall distance measurements were gathered in earlier rock mechanical works.

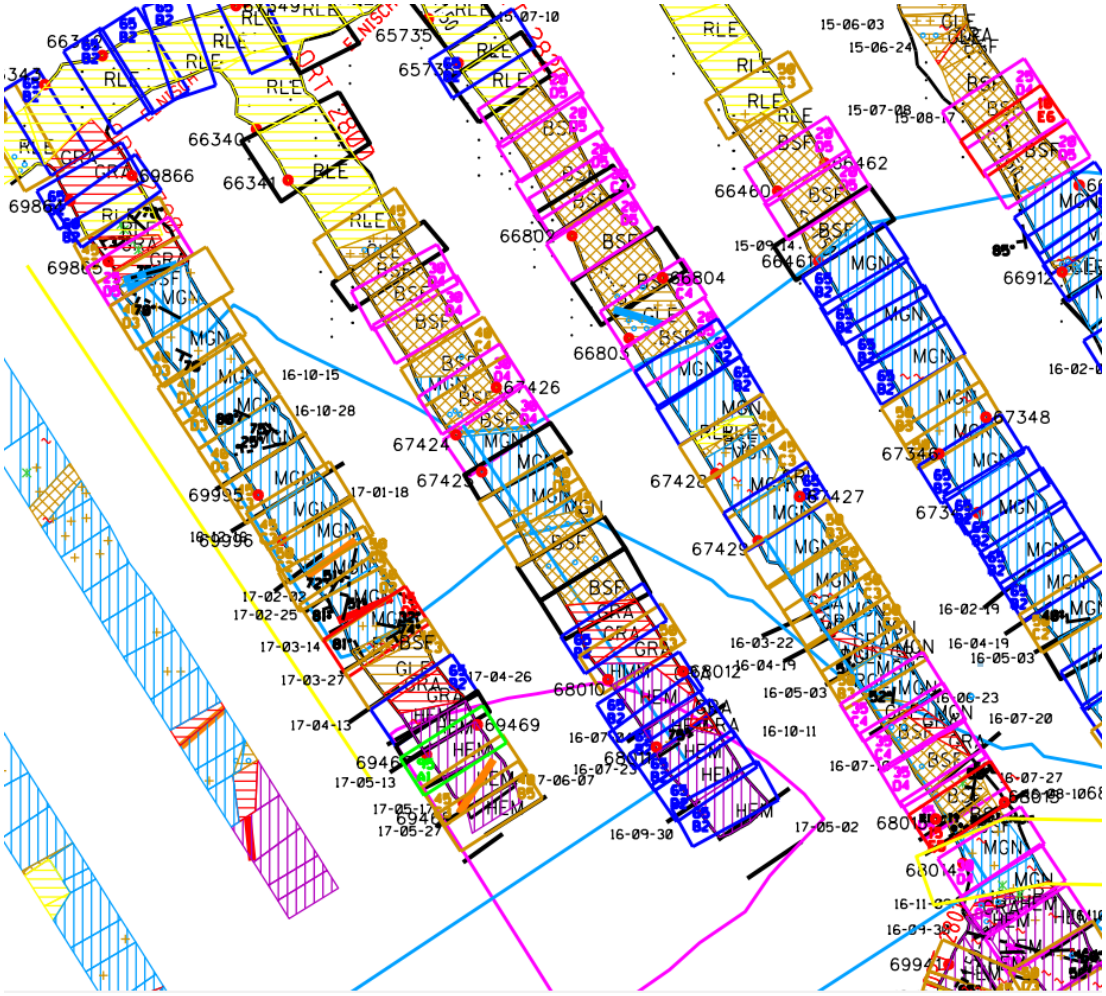

Figure 33: Layout of AL 1082 with geological features (MicroStation V8i)

Drift 2800 and 2820 show a high occurrence of biotite schist at the first ore contact zone with weak rock mechanical properties (Figure 33). The schist has a GSI-value of 20-30 with poor surface conditions and many intersecting discontinuity sets. The first part of the orebody seems to be competent rock, but later parts show a decreased GSI-value and intrusions of biotite schist and granite. 2780 also has a weak ore contact zone with biotite schist abundance with a GSI of 25, but in a smaller extend. Figure 34 shows the current condition from drift 2800. This is one of the most affected areas. Many bolts are loaded, cracks are long and wide and the fibrecrete is loosening at the bottom of the walls, causing the rock to break through. The cracks

are beginning to connect and are getting longer as well as wider, resulting in less stability. As the rock piece shows it is mostly biotite schist at the areas where the rock breaks through. 2780 and 2820 are also affected by the consequences of deformation but are in a better condition.

Figure 34: Current state in AL 1082o2800

The wall-to-wall distance measurement in 2780 over three months shows a peak change of 1.5 cm and is therefore not further considered here. In 2800 reduction of distance of 3.0 cm occurred in section two, the area with the outcropped biotite schist (Figure 35). Deformation in the order of -2-3 cm also occurred in section one and five during the three-month period.

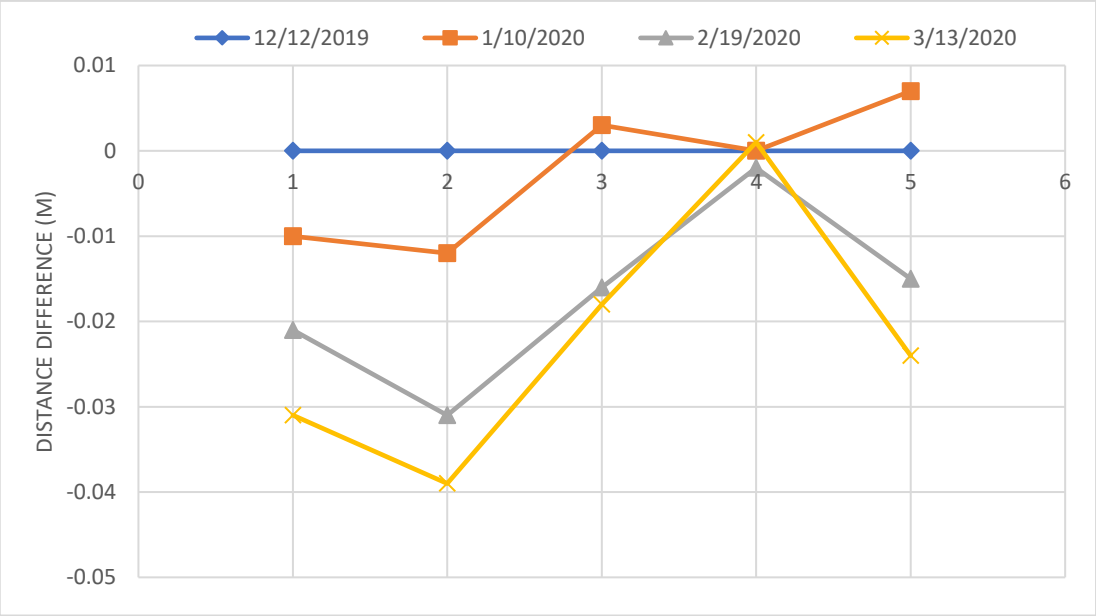

Figure 35: AL1082o2800 Wall-to-Wall Convergence/Divergence (by Jones, 2020)

5 The uGPS Rapid Mapper™

In order to collect data of large areas more quickly a new mobile laser scanner is used (Figure 36). This results in a lower point cloud density with a useful accuracy for the given conditions. The scanner is designed to be mounted to a vehicle. During the scanning procedure it is installed on a mount at the front of the car and connected to the electricity of the car. There have been above ground solutions on the market for many years with stationary scanners and a GPS device to enable mobile scanning. This does not work underground. The uGPS Rapid Mapper™ by Peck Tech Consulting Ltd. uses vertically and horizontally mounted SICK LMS 111 scanners, optional RFID tags for global coordinate referencing and an IMU for assisting in motion tracking to scan underground. The vertical laser measures the distance between the scanner and the drift perimeter and by using the estimation of the current position and movement during the scanning along the opening it creates and positions rings in space, which over time produces a 3D point cloud of the scan area (Lavigne & Marshall, 2012). Table 15 shows more specifications of the device.

Table 15: uGPS Rapid Mapper™ specifications

Range	25 m
Scanner Accuracy	+/- 30 mm
Scanner Precision	+/- 12 mm
Viewing Angle	270
Angular Resolution	0.5
Scanning Frequency	10 Hz
Vehicular Speed	1 – 15 km/h
Scan Spacing	Vehicle speed [m/s] / 10 Hz

Figure 36: The uGPS Rapid Mapper™ (Peck Tech Consulting Ltd., 2020)

5.1 System implementation

Prior to scanning the area must be prepared through several steps. For the geo-referencing and alignment of the scans LiDAR targets need to be installed, surveyed and documented with information about the target's identification, position, and purpose (Figure 37). Additional information about the route of each scan is also included. The data is recorded in a CSV-file and defined as the control points file. Scanning without targets to check the roughness of the surface or other interests is possible, but for comparing scans the geo-referencing is obligatory. While installing the targets several points must be followed:

- Spacing of 50 to 100 m
    - Smaller distance leads to high rate of smoothening

    - Higher distance leads to higher accuracy errors
- A target is required at the start and end point of every scan
- Targets should be preferably installed in the height of the scanner
- Long axis parallel to the tunnel to ensure a high enough reflection
- Possibility to survey must be ensured

After the appropriate installation of the targets the targets can be surveyed by the surveyors to use it for the alignment of the scans.

Figure 37: LiDAR target installed in a drift

5.2 Data collection and processing

The scanning procedure always included some initial steps. The uGPS Rapid Mapper™ is attached underground at main level 1000 to the mounting system in front of the car and connected to a laptop via Wi-Fi. The user connects via a real-time interface for calibration of the scanner. The calibration is done on a levelled concrete surface with the engine turned off, ensuring no mistakes by a gradient and vibration. Afterwards, the scanning in desired areas can start. For scan comparison, the starting location needs to be the same every time within a couple of meters and starting and end point must be 5-10 m before or after the first or last target, respectively. To minimize variability in the start and end points we defined rules to follow:

- Starting point: Circles with spray paint on left and right wall at the height of the driver
- End point: One car length after the last target

The speed recommended by Peck Tech Consulting Ltd. during the scans is 3 km/h to ensure a high enough point cloud density (Figure 38). Higher speeds lead to lower data density possibly resulting in accuracy issues and target alignment failures. During the scans a real-time interface shows on a computer the driving speed as well as the functionality of both scanners. After scanning and inputting locational information and scanning notes, the scans can be downloaded through a wi-fi connection or USB stick from the scanner.

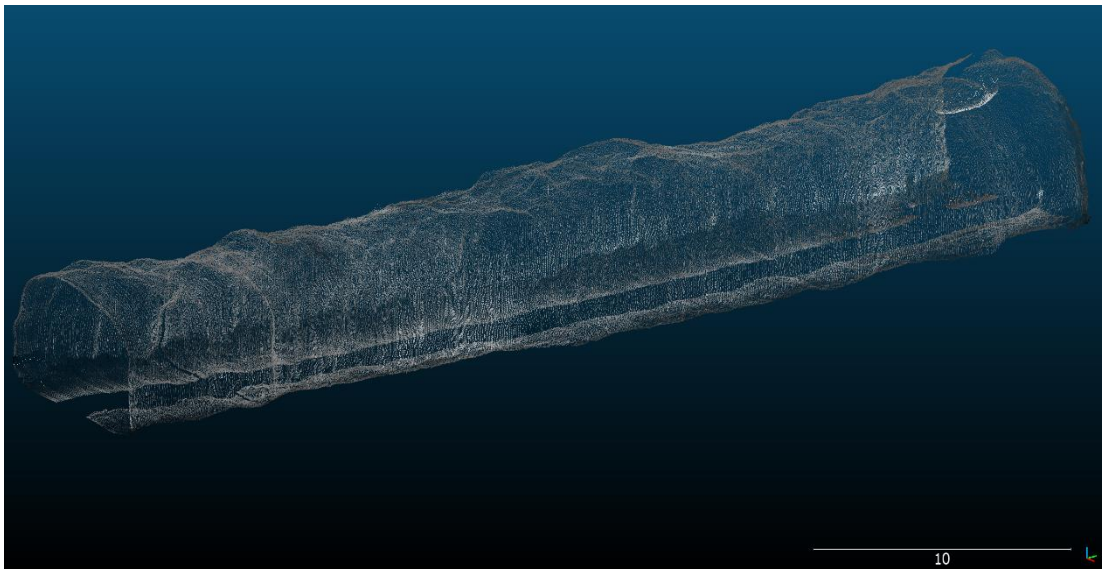

Figure 38: Sample scan of the uGPS Rapid Mapper™ showing the intensity (CloudCompare)

Afterwards, the scans can be converted with the uGPS Rapid Mapper™ Scan File Converter and the control points file to conduct the target alignment for further analysis in CloudCompare. Also, the convergence monitoring analysis between different scans is created in the converter and examined in CloudCompare.

To always have a set of actual scans of different locations and additional information a scan register is created. The aim is to have bi-monthly or monthly scans of the locations depending on the first research results. For instance, areas close to production and prone for deformation such as the crosscuts in PR 1023 are of huge interest.

5.3 Experimental testing

To validate that the system is working within the known parameters several tests were designed, performed and analysed. The emphasis during the tests has been on the accuracy and repeatability of the measured values. The aim was to have a higher confidence in interpreting the data as well as the ability to filter data.

5.3.1 Impact of different calibrations

In order to determine the impact of the calibration on the scientific work with the uGPS Rapid Mapper™, the calibration was carried out with same and different slopes instead of on a plane surface. For this purpose, gradients of 0°, 1°, 5° and 10° were chosen to scan the same area three times with every calibration setting. Figure 39 shows the experimental setup used for this experiment. To simulate a calibration on a slope, wood was placed under the front wheels. Since the method proved to be impractical above a slope of 5°, washers were placed under the uGPS Rapid Mapper™ in the further test series. Drift PR1051o4090 was then scanned as described in the test procedure.

Figure 39: Calibration procedure with wood under the front wheels

In the test series, some of the calibrations from 0° to 10° provided an extreme dislocation of the original scan (Figure 40). Only in the surveyed target locations the measured data series are the same. The drift was scanned from right to left, so a calibration at an incline implies a negative slope during the scanning procedure. This was to be expected, since for example a slope of 5° is defined as a 0° inclination during calibration. Consequently, the drift with an approximate slope of 0° is visualized with a slope of -5° and in order to be located at the right height at the surveyed target locations, the scan starts at a higher position.

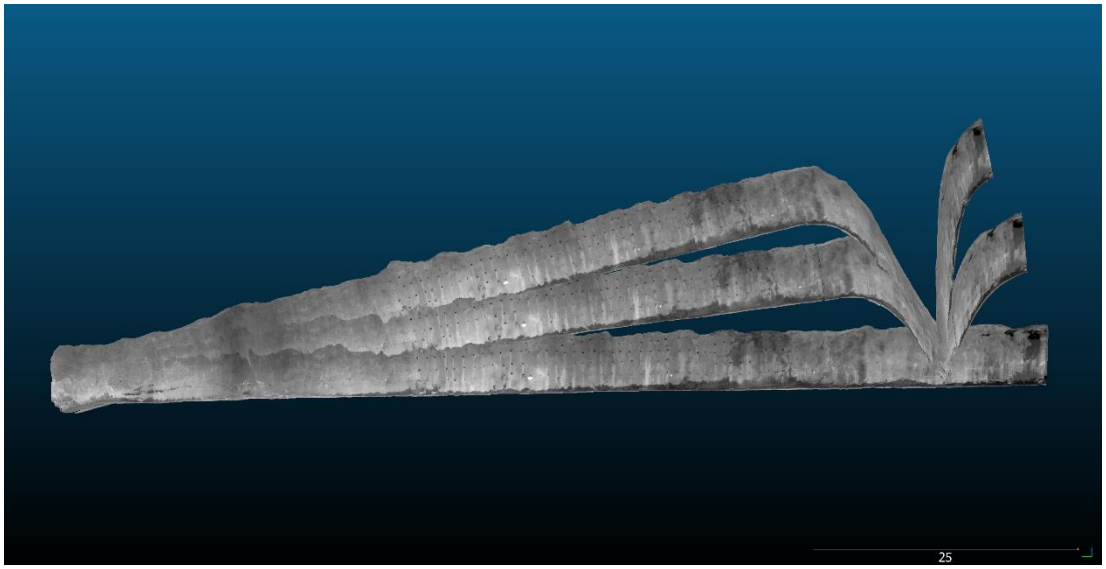

Figure 40: Scans with a calibration of 0°, 5° and 10° (CloudCompare)

The test series shows the importance of reasonable calibration before scanning in order to be able to rely on the results. Calibration at a slope with 1° shows no measurable difference, but anything beyond that shows a difference. For this reason, a spirit level was always used during the calibration procedure to measure that the area is flat ensuring that the calibration is done properly. Thus, the influence of calibration mistakes on the repeatability and accuracy of the scans can be excluded.

5.3.2 Impact of different driving

As a rule of thumb, the vehicle driver should attempt to drive in the center of the opening being scanned. In this test series, non-central driving was intentionally exaggerated to see if and how significant the influence of driving style is on the

repeatability and accuracy of the uGPS Rapid Mapper™. For this purpose, the drift PR1051o4090 was scanned six times, twice centered, left-adjusted and right-adjusted. Other parameters, such as calibration, driving speed and light emission, were unchanged during the test. After that, an analysis of the individual scans as well as convergence monitoring with a centered scan as reference file was performed.

Observing the individual scans, it is noticeable that, compared to driving in the middle, the intensity and thus the recognition of the underground infrastructure is different (Figure 41). This is critical if, for example, water or cracks in the fibrecrete want to be detected, especially if they extend from the left to the right side. This is because the same object has a different intensity on the left than on the right side while not driving centered.

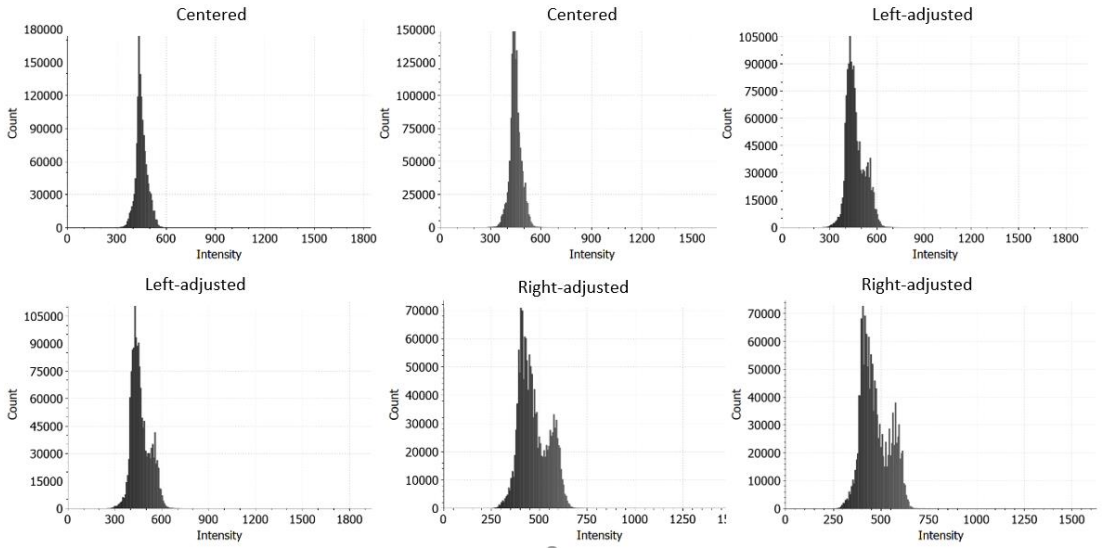

Figure 41: Histograms of the intensity while driving centered, left- and right-adjusted (CloudCompare)

Furthermore, the convergence monitoring also shows differences in relation to non-centered driving. Figure 42 shows from left to right the convergence monitoring of centered driving with the two left-adjusted, the two right-adjusted and the centered driving. It is apparent in this figure that the first four convergence monitoring show more deformation areas than the fifth. Thus, the driving has not only an influence on the intensity of the laser but also on the accuracy of the laser and convergence

monitoring. For this reasons, centered driving was always checked during the scans to exclude any intensity and accuracy issues.

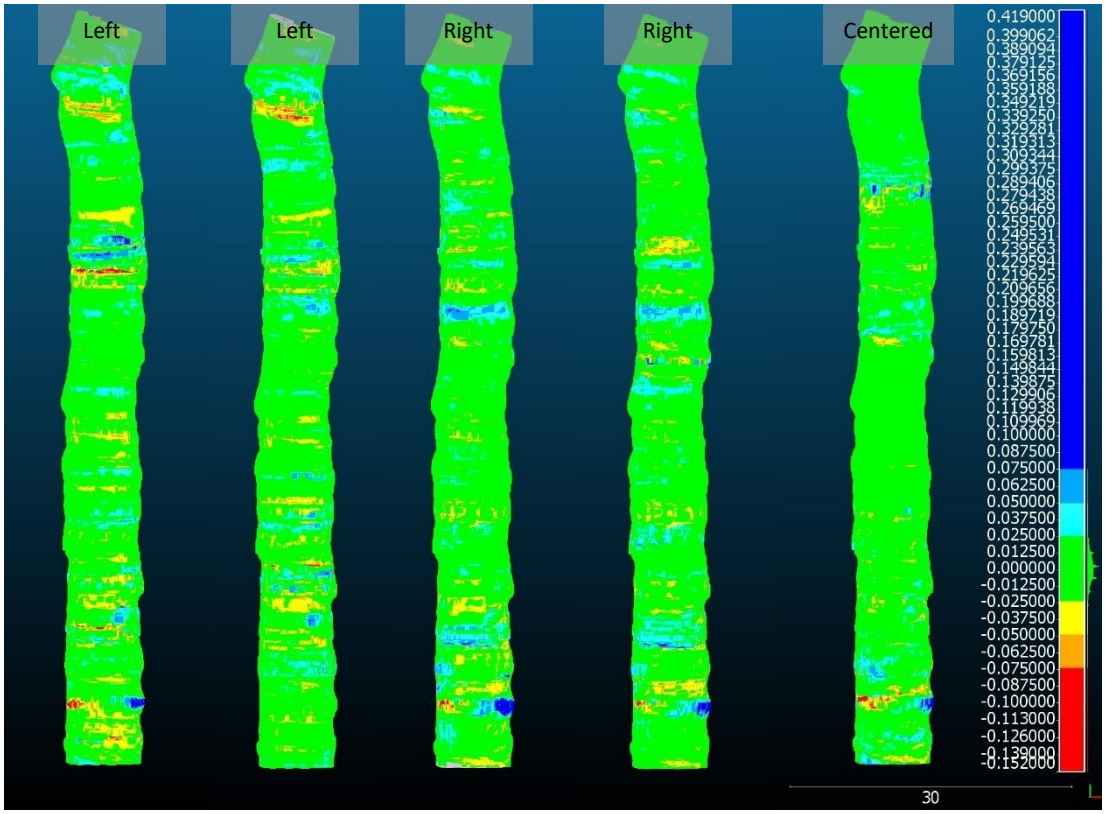

Figure 42: Convergence monitoring of centered driving to left-, right-adjusted and centered driving with a deformation scale in m; top view (CloudCompare)

5.3.3 Convergence monitoring test

This test series, where deformation is imitated through three movable wooden objects on the wall, is designed to assess the accuracy and resolution of convergence monitoring. The possible impact of the angle of incidence on the laser is also considered as a central factor. The angle of the surface of the objects varies between 22.5°, 45° and 67.5° relative to the angle of incidence of the laser beam. To imitate a deformation the three objects were moved 2 cm between scans until a total artificial deformation of 8 cm was reached. The form of the objects and test designs as a sketch and in installed form can be seen in Figure 44 and Figure 43. Through convergence monitoring of the original layout with the attached objects layout and with the different deformation values the accuracy, resolution, and impact of angle of incidence can be derived.

The first test was completed with thin, 5 cm objects. After the first test in AL1052o2810 with the thin wooden objects it became clear that wider objects in z-direction are needed for the convergence monitoring even though the thin objects are identifiable in the actual scans (Figure 45). Therefore, new sketches were made and the three objects were enlarged for the second run, where the height was increased to 60 cm by adding wooden plates. The test procedure stayed the same with a deformation rate of 2 cm and a maximum deformation of 8 cm in the same drift.

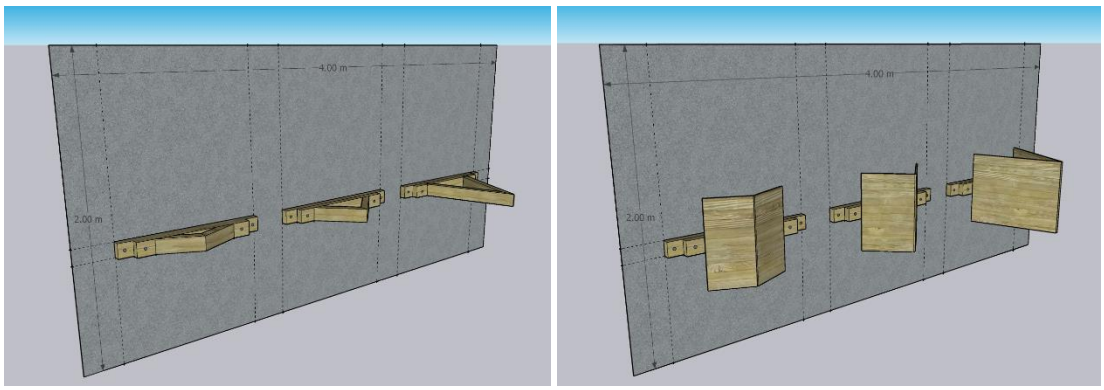

Figure 44: Test design of objects for both tests (Google SketchUp 2020)

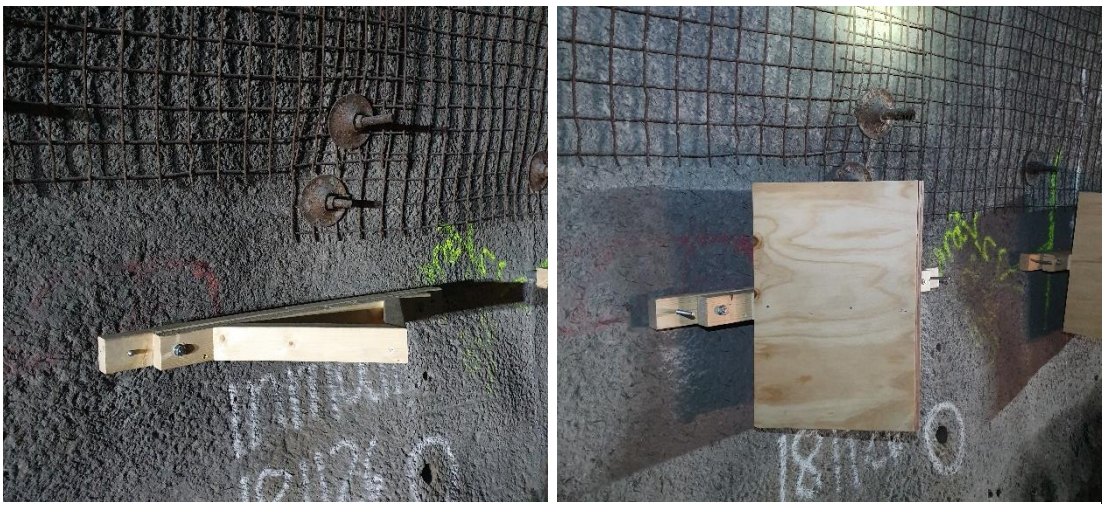

Figure 43: Wooden objects with 45° of both tests in installed locations

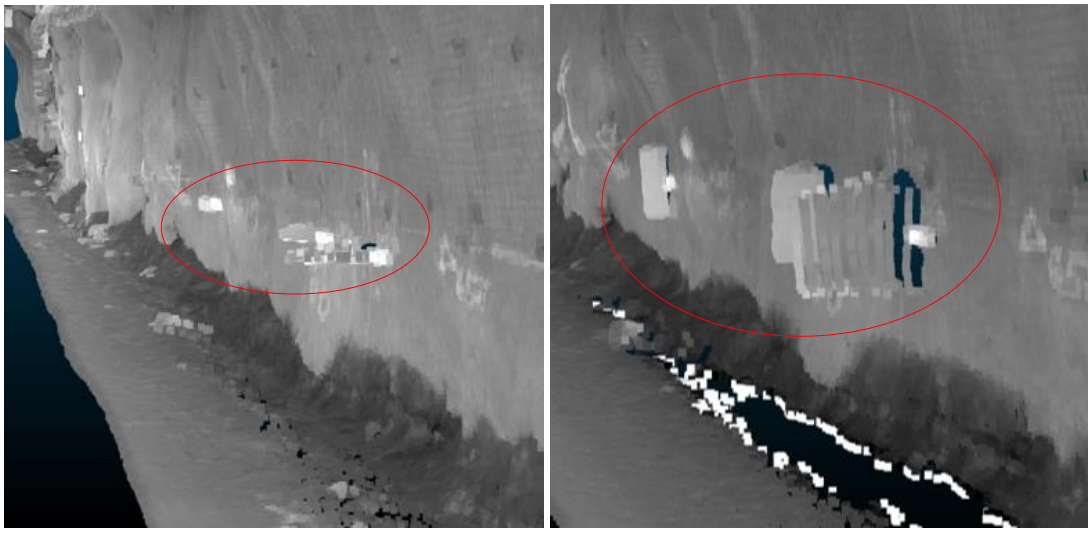

Figure 45: Scans of installed objects of test 1 & 2 without artificial deformation (CloudCompare)

Since no visual deformation could be detected in the convergence monitoring analysis with the first test design due to the 5 cm thin objects, the test results will not be discussed further.

In the adapted test design, the three objects are clearly visible in the convergence monitoring (Figure 46). Convergence is visible in the program from an artificially created deformation of 4 cm. In the later analysis of real deformation, it should be considered that in the last scan, with a deformation of 8 cm, an error appears at the object with 67.5°. Instead of showing the artificially induced convergence on both sides of the triangle, a change from divergence to convergence can be seen. In addition, the scanned deformation is significantly larger than 8 cm and there is a propagation of the error.

Thus, it can be concluded that the convergence monitoring of the uGPS Rapid Mapper™ can provide reliable results starting from a deformation of 4 cm, but especially uneven, irregular and rough surfaces, an alternation of divergence and convergence as well as suspiciously large deformations have to be particularly controlled to avoid misinterpretations in the results. The source of this error is a miss-matching of the compared laser scan lines across the angled surface as the vehicle drives by. It tends to create or exaggerate actual convergence. It is a well-understood error that does not detract from the usability of the system, but the user must be

aware of it. It can typically be identified in the scan and verified by looking at the raw scan data. All mobile scanners suffer from errors of this type.

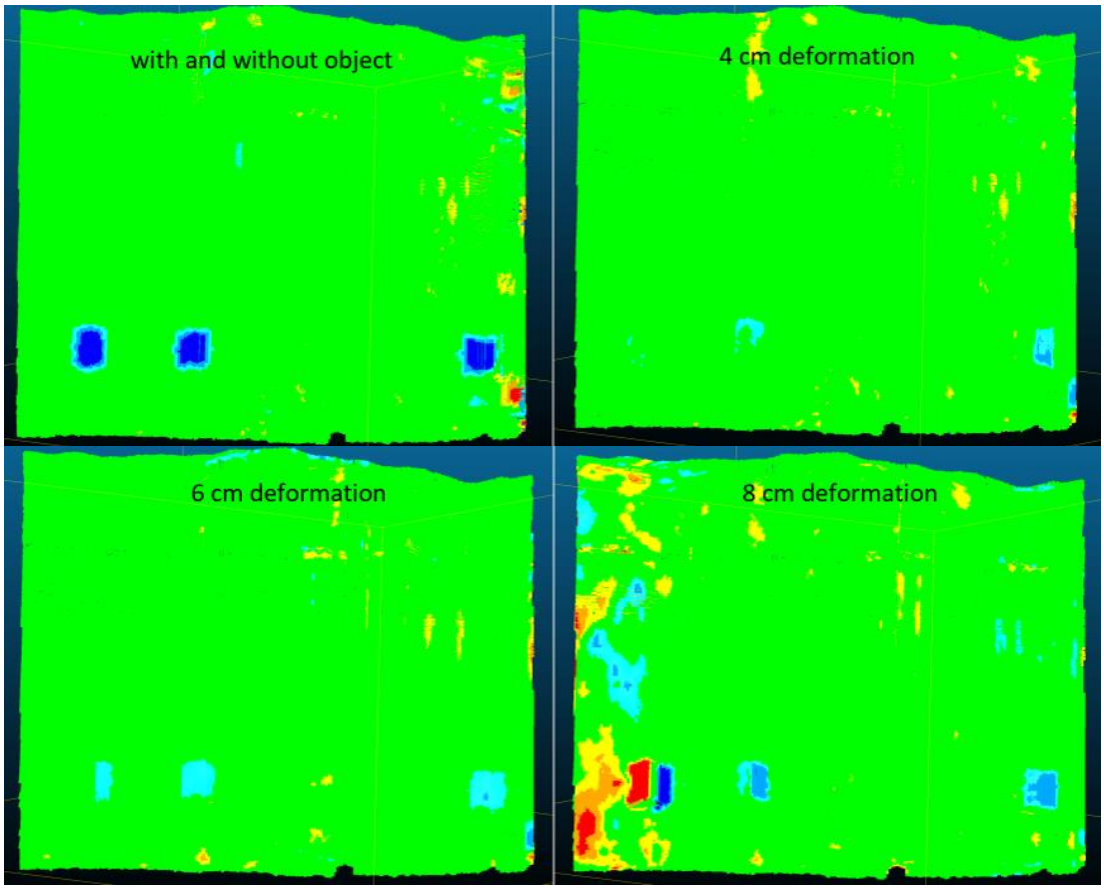

Figure 46: Convergence monitoring with & without an object, 4 cm, 6 cm and 8 cm deformation (CloudCompare)

5.3.4 Repeatability test

The applied repeatability test was performed in HO1051o2590 by placing four additional unsurveyed targets between the two existing surveyed ones (Figure 47). The drift was then scanned ten times in a row without varying parameters. Convergence monitoring was used to see whether there is no deformation or whether there were any anomalies that would affect the repeatability. With the four additional targets attached, a statistical analysis was performed on the variation of the size of the targets in xy- and z-direction. In this analysis, the distance between the targets was from 11.5 to 12.6 m and a total of 60 values per direction were available.

Figure 47: Test design with additional unsurveyed targets

In the convergence monitoring, the first scan was compared with the subsequent nine scans. In nine out of ten cases, no anomalies were found that would hinder the interpretation of real data in the research work. The convergence monitoring of scan six to one shows a deformation range of -0.206 to 0.163 m, which is certainly due to an error (Figure 49). It can be seen that deformation is already indicated at the beginning of the scan due to a change in the ventilation tube because of changing air volumes in the tube. This causes minimal deformations in the further run of the scan. After the two shotcrete arches, an extreme error occurs, which could already be observed in a similar way in subsection 5.3.3. Also, in this test a rapid change from divergence to convergence as well as a propagation and an increased deformation value of up to -0.206 m can be seen. When viewing the scan in plan view it is notable that the change takes place from one side to the other and looks similar to the convergence monitoring with centered driving in Figure 42 lower part (Figure 48).

It seems that the error occurs more frequently at the end of scans and after unusual changes such as the shape of the ventilation hose or the appearance of shotcrete arches. The test underlines the importance of careful analysis of areas with alternating convergence and divergence as well as areas with conspicuously large deformations in order to not interpret data wrong.

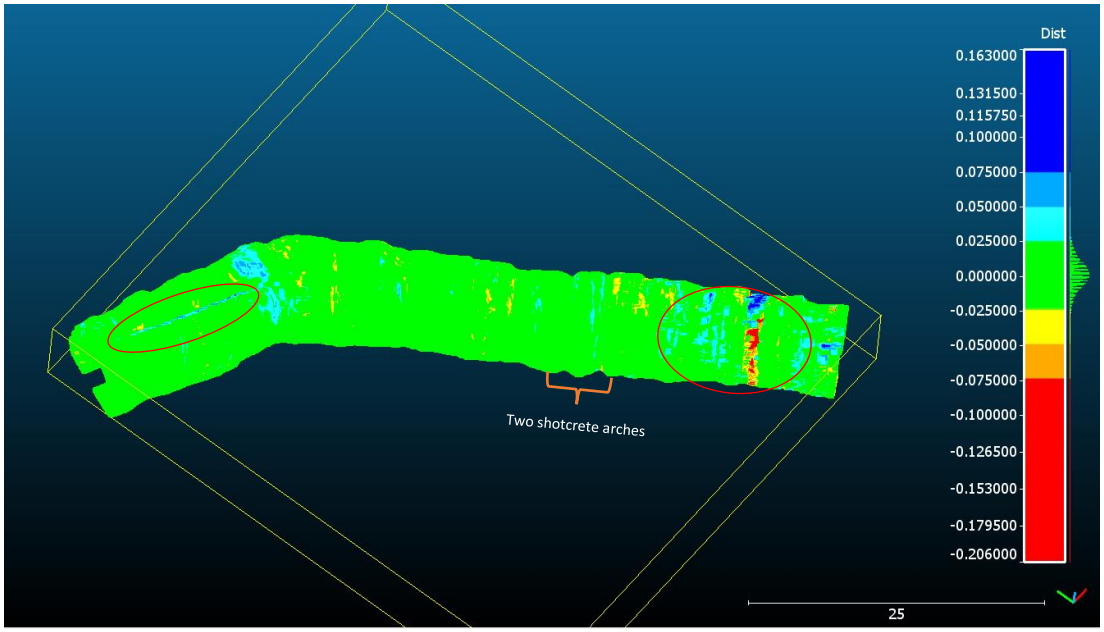

Figure 49: Convergence monitoring of scan 1 & 6, deformation scale in m (CloudCompare)

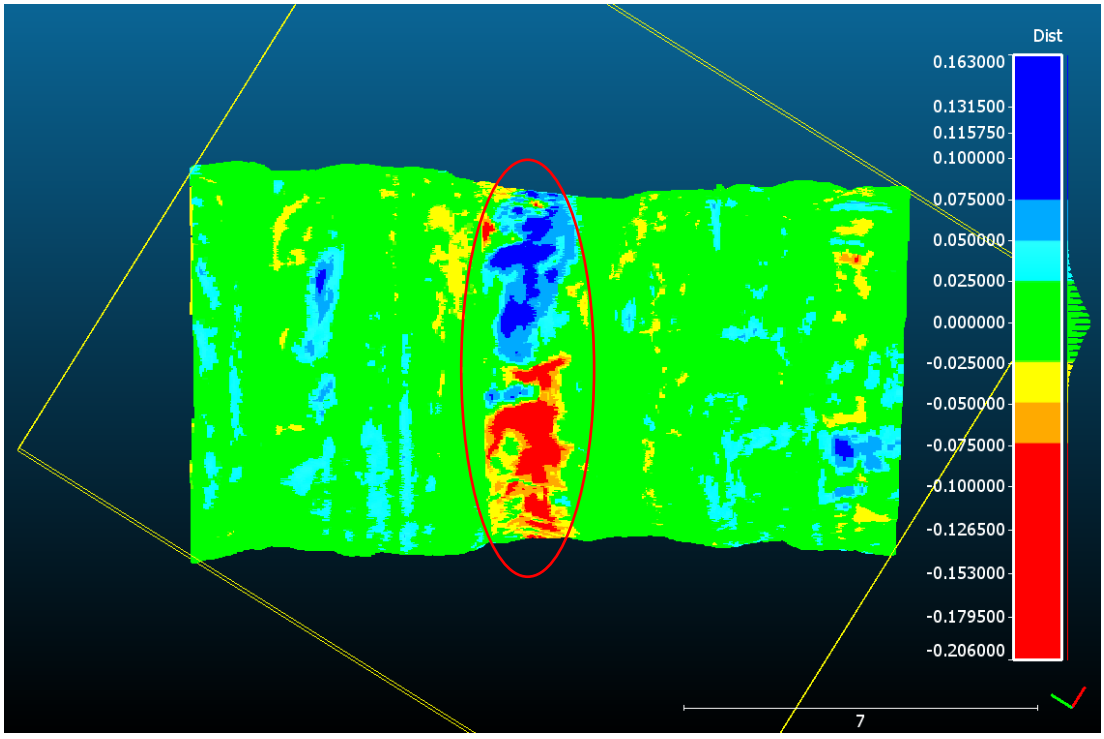

Figure 48: Detailed convergence monitoring of scan 1 & 6 in high deformation area with top view, deformation scale in m (CloudCompare)

The statistical analysis of the 60 values of the target size is visualized in a box plot diagram (Figure 50). In the z-direction, the target size shows a smaller deviation. The range of all values is between 0.3 and 0.37 m and thus deviates by a maximum of 4 cm from the median of 0.34 m. 50 % of all values are between 0.322 m and 0.35 m.

In xy-direction, the range of values is between 0.45 and 0.58 m with an outlier at the lower end of 0.41 m. The maximum deviation from the median 0.51 m within the box plot is 9 cm. The median is exactly in the middle of 50 % of the values.

Thus, the size deviation in z-direction is fully within the limits, whereas the range in xy-direction is a somewhat large one.

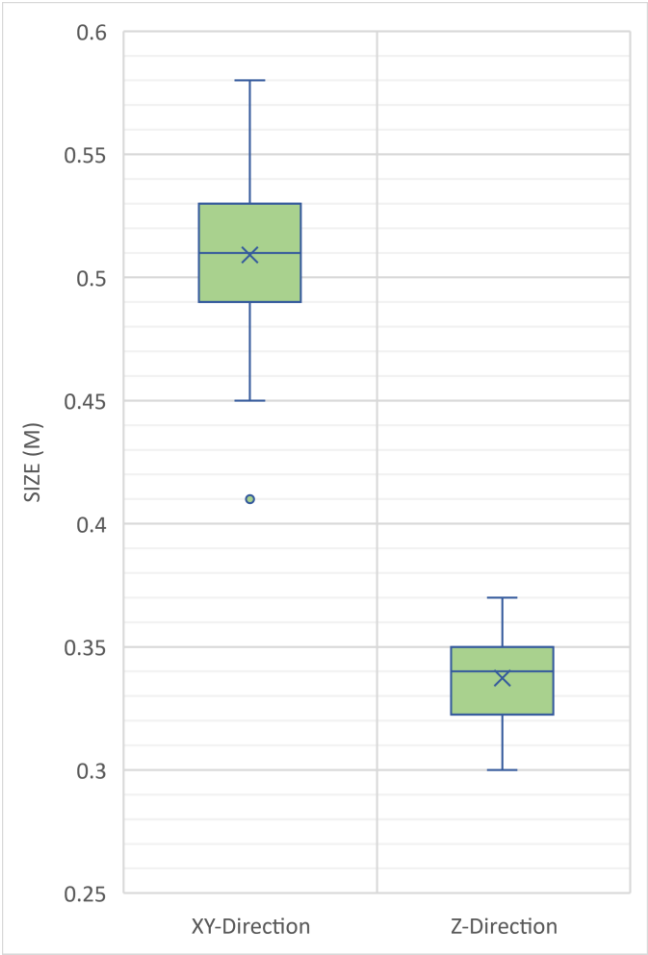

Figure 50: Box plot diagram of target size in xy- & z-direction

5.3.5 Scan repeatability and accuracy test

This test series was analysed by Alkayal (2020) and the preparatory field work was carried out in collaboration. To determine the repeatability of scans from the uGPS Rapid Mapper™ simply in HO1051o4090, three scans were conducted and the wall-to-wall distance at a specific place was measured manually with a laser range finder as well as in CloudCompare for all three scans. To minimize any human error, the

average value of three measurements was taken and the points were marked with white spray paint to find them for the measurement in CloudCompare. Table 16 shows the test results.

Table 16: Difference of manual measured and scanned distance (Alkayal, 2020)

Scan	Distance (m)	Difference (m)
Laser distance meter	6.791	0
1	6.768	0.022
2	6.779	0.011
3	6.771	0.019
4	6.775	0.015

The maximum deviation of the distance determined in the scan to the manual measurement is 0.022 m and the maximum deviation between the scan values in CloudCompare is 0.11 m for scan one and two. The assessed values are within the expected accuracy of the scanner (Table 15).

To determine the individual accuracy of the scans from the uGPS Rapid Mapper™, an analogical test was performed in the same drift. Using a laser range finder, the distance between points was measured and compared with the distance of the same points in the scan. To minimize human error during the measurement, the average value of three measurements was taken for comparison and the points were marked

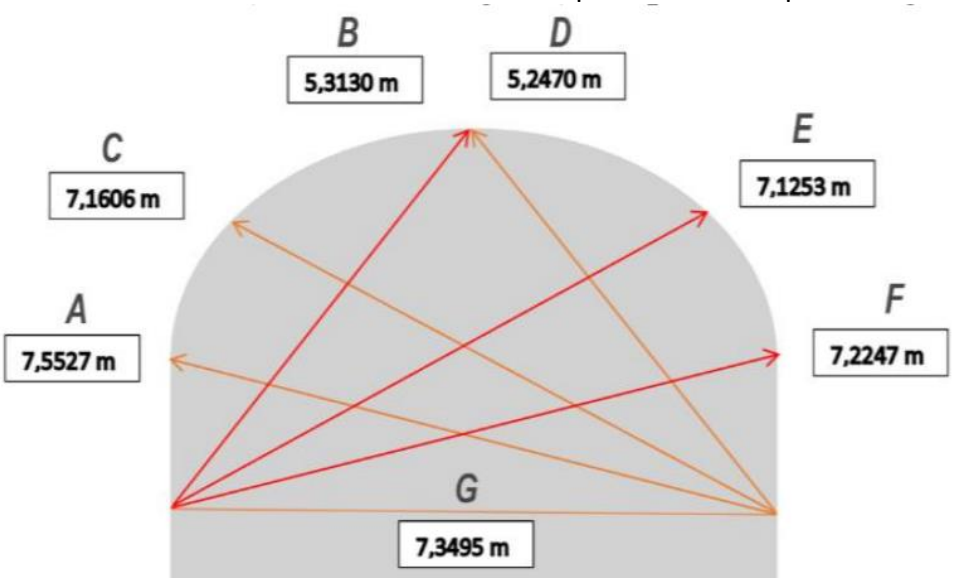

Figure 51: Distance measurement with laser range finder (Alkayal, 2020)

with white spray paint so that they are visible in the scan in CloudCompare. For the test seven points were marked, three on each side and one at the roof (Figure 51; Figure 52).

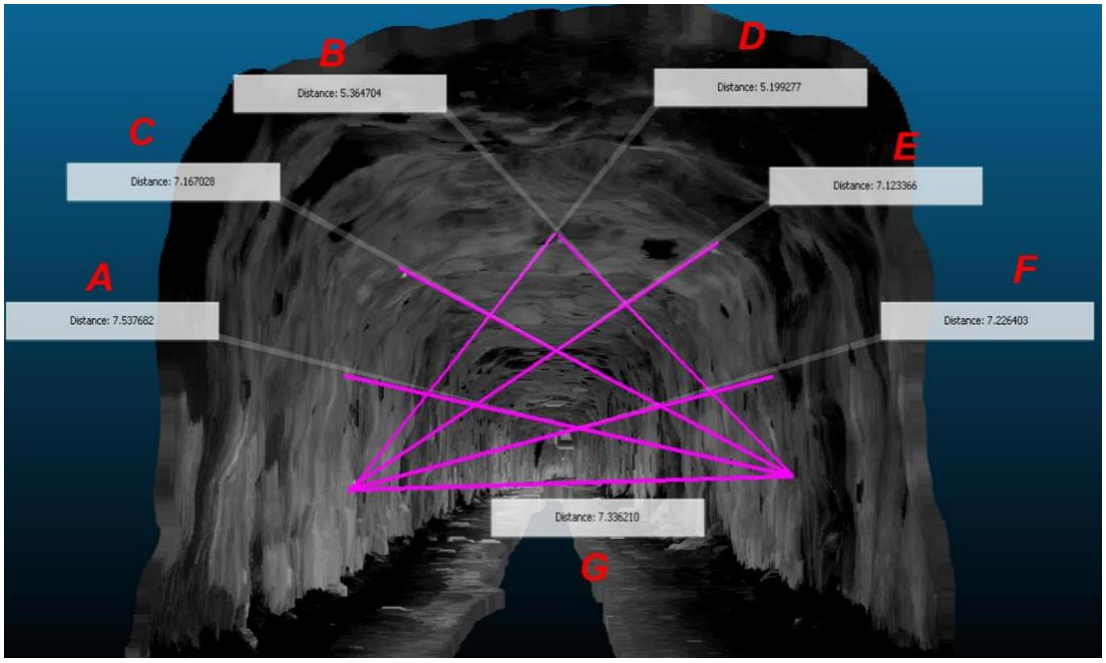

Figure 52: Distance measurement in CloudCompare (Alkayal, 2020)

Table 17: Difference in distance between manual and CloudCompare measurement (Alkayal, 2020)

Measurement	Difference (m)
A	0.015
B	-0.064
C	-0.052
D	0.048
E	0.002
F	-0.002
G	0.013

In Table 17 the difference between the manual measurement and the measurement of the scan in CloudCompare of the seven distances can be seen. A, E, F and G have a smaller deviation than 2 cm. This is within expectations since the scanner has an accuracy of +/- 3 cm (Table 15). B, C and D have approximately a deviation of 5 cm. Due to the simple experimental setup, it is not possible to definitively determine the

source of the error. There could have been a minimal deviation due to a human mistake during the measurement with the laser range finder or during the measurement in CloudCompare.

6 Results

The results of the scans will be reviewed individually. A discussion and comparison of the scan results obtained can be found in Chapter 7.

During the project 353 scans were conducted to test the system and investigate the deformation underground. The goal was to obtain bi-monthly to monthly scans of every scan path in the area. However, in an actively producing mine, the priority is set differently, so that safety and the fulfilment of production targets are more important. This led to piles of rock, machines or destroyed targets in the drifts as well as closed drifts due to safety precautions. Nevertheless, enough data of most drifts could be collected during the fieldwork period. Since the research areas of the AL and HO orebody are adjacent, the scans are in the same subsection.

6.1 Printzsköld

The PR orebody has been of central interest from the very beginning. Especially PR996 and PR1023 are of interest to be able to draw conclusions about possible consequences in PR1051 or deeper.

In PR996o4090 the scans show that there is convergence on both walls and that the floor heaved over time. All scans are compared with a baseline scan from 18.12.2020, so it shows a total time span of 5.5 months. During this time, there is a measured maximum deformation of 26.2 cm in the shown part of the drift in the convergence monitoring, with quantitatively more convergence occurring. Appendix 2 also shows the left wall of the drift. The wall-to-wall distance decreased in the same area 15 cm in 6 months (Figure 17). It must be considered that the wall-to-wall distance includes the deformation at both walls in the measurement.

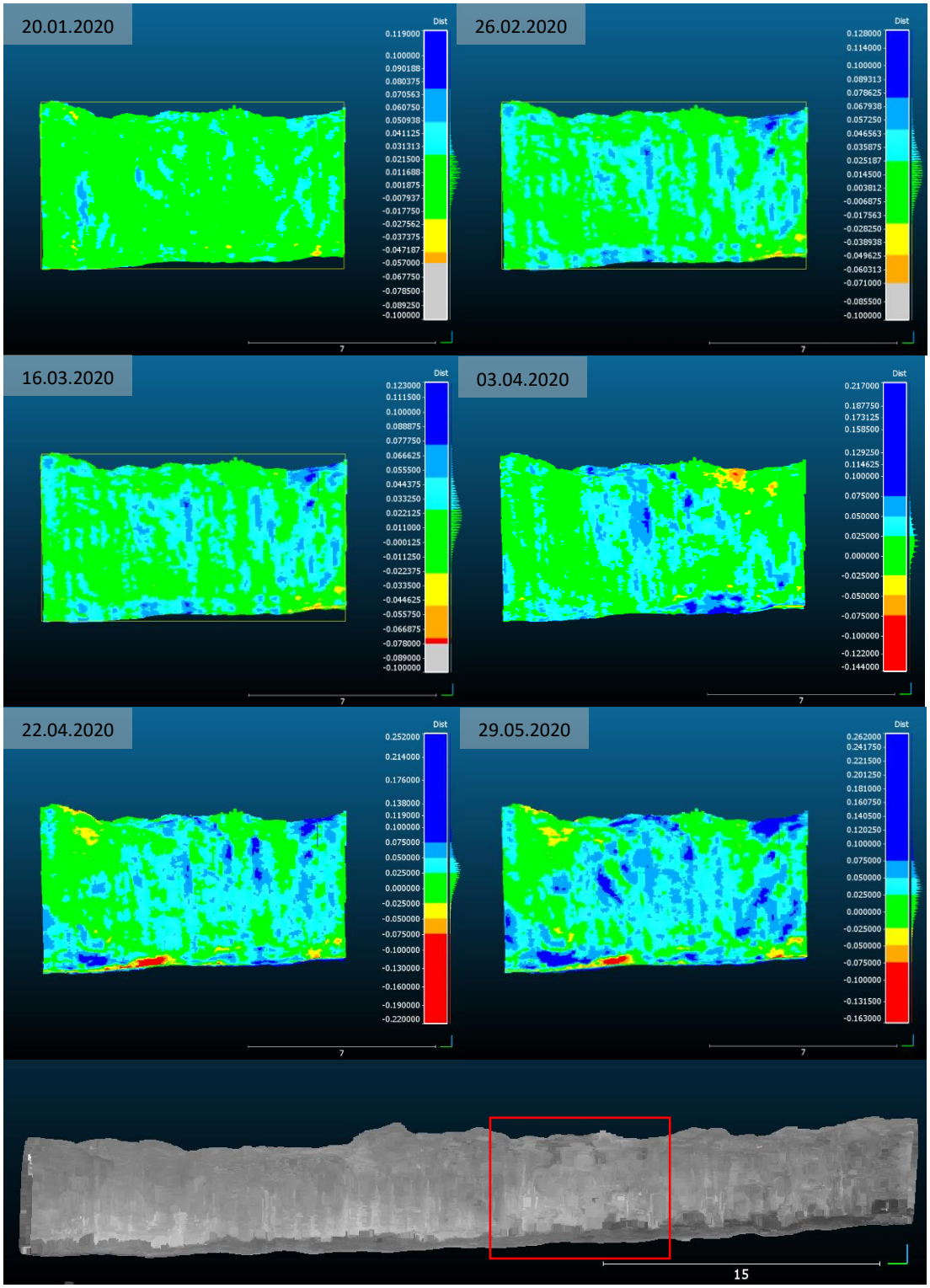

Figure 53: PR996o4090, convergence monitoring on the right wall with a scan from 18.12.2019, square indicates convergence monitoring area (CloudCompare)

In PR1023o4060 no trend in deformation is detectable between 19.03.2020 and 29.05.2020 (Figure 54). Instead, the error of convergence and divergence from the

test series can be detected at the end of the drift. The rest of the drift shows fluctuations that do not follow any detectable trend.

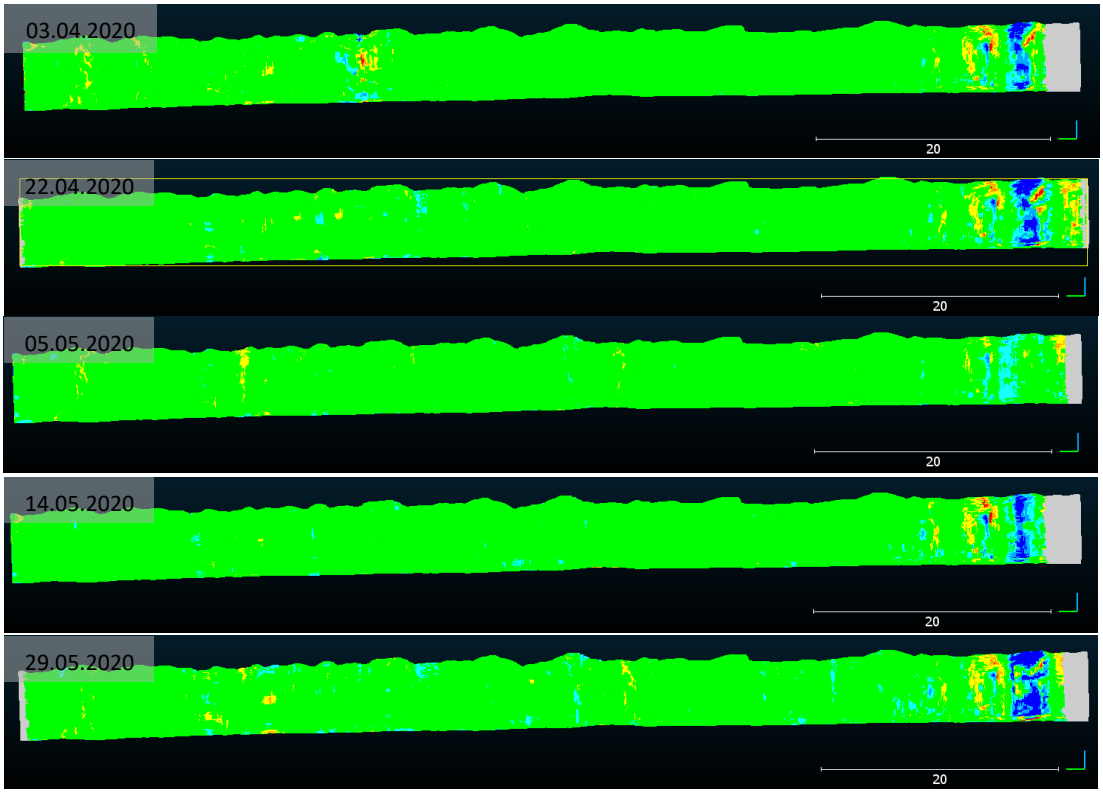

Figure 54: PR1023o4060, convergence monitoring on the right wall with a scan from 19.03.2020 (CloudCompare)

In the adjacent drift PR1023o4080 deformation is detectable, but also the earlier mentioned error. The error occurs again at the end of the drift and shows a suspiciously high deformation magnitude of +/- 14.8 cm in 15 days with a rapid change from convergence to divergence at the roof in plan view (Figure 55).

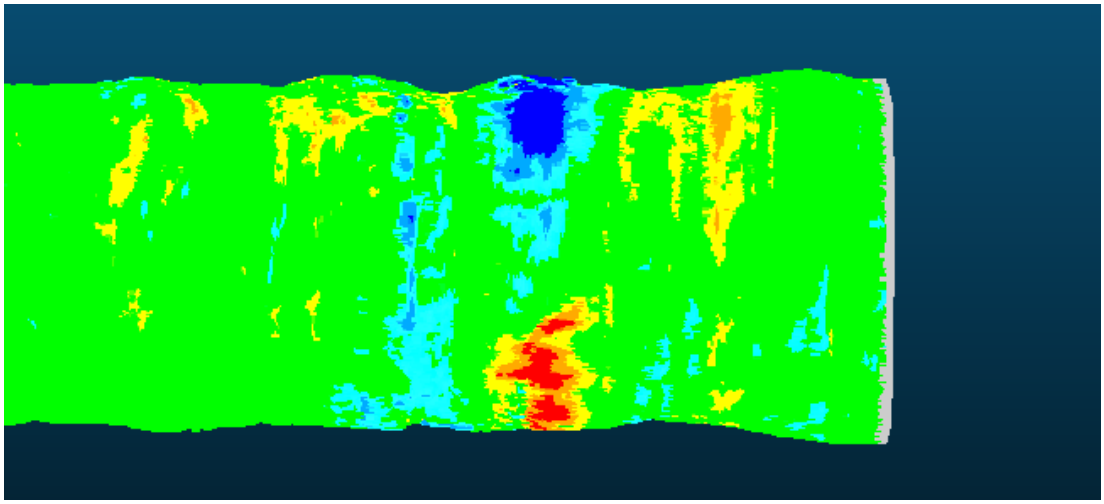

Figure 55: PR1023o4080 error in convergence monitoring at the end of the drift in plan view (Cloud Compare)

The detectable deformation on the right wall of the drift shows a maximum deformation of 10.5 cm in a time span of 2.5 months and is at an area with more water as seen in the last intensity scan of the drift by a darker grey (Figure 56). Convergence mostly occurs at the right side of the monitoring section. This area consists of grey leptites with biotite inclusions and a GSI-Value of 30, where a wall-to-wall convergence of 7 cm in three months was manually measured, the floor heaved and extensive cracks on the right wall occurred (Subsection 4.1). Other areas, except for the end of the drift with the known error, do not show any detectable trends.

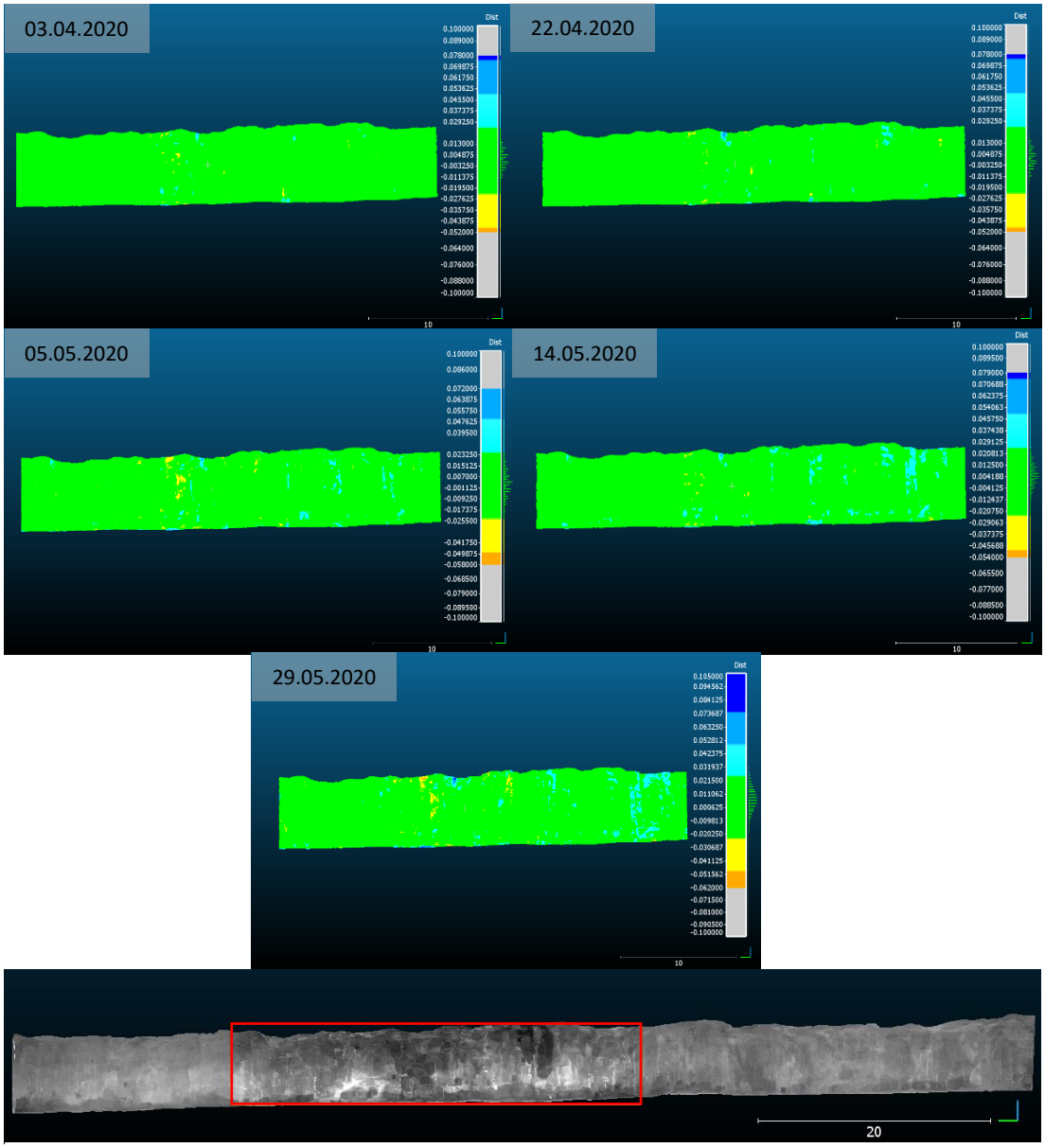

Figure 56: PR1023o4080, convergence monitoring on the right wall with 19.03.2020 as reference, square indicates convergence monitoring area (CloudCompare)

In PR1023o4100, there are only two scans in the research time that can be compared in convergence monitoring. Deformation in the range of 25 cm is indicated at many locations of the drift for a period of less than one month. In addition, the well-known error with the suspiciously high deformation at the beginning and end of the drift becomes apparent again. (Figure 57).

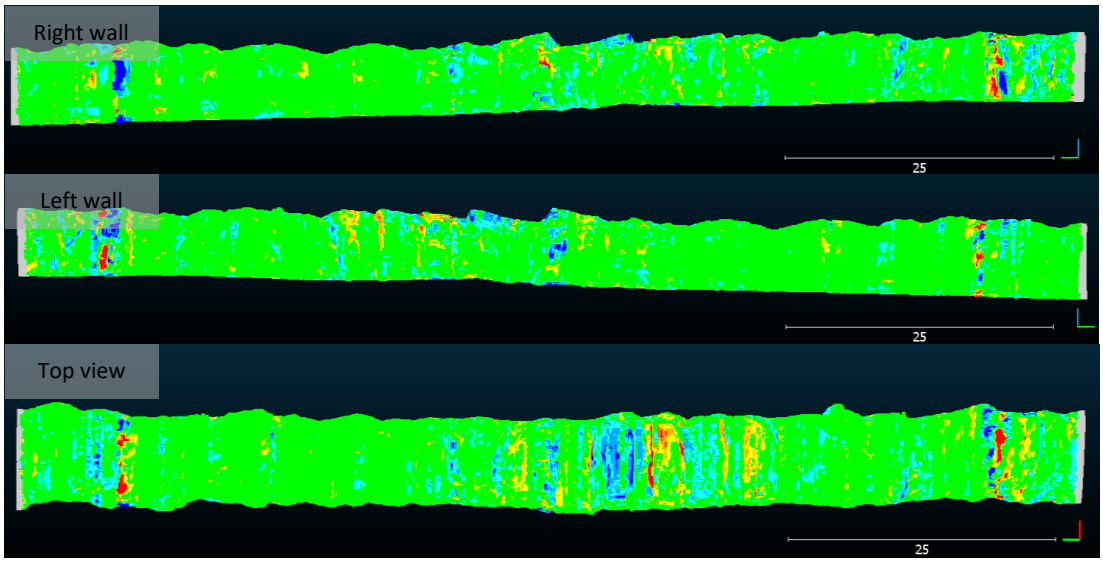

Figure 57: PR1023o4100, convergence monitoring 21.02. & 16.03.2020 (CloudCompare)

In the three drifts of PR 1051, no trends could be found that indicate progressing deformation. As in previous convergence monitoring, some data shows the divergence-convergence error occurring most frequently at the end of the drift.

6.2 Alliansen and Hoppet

Since the level 1082 and 1080 are prioritized in the two orebodies, the corresponding results are shown first. Figure 58 shows the crosscut layout of the adjacent orebodies.

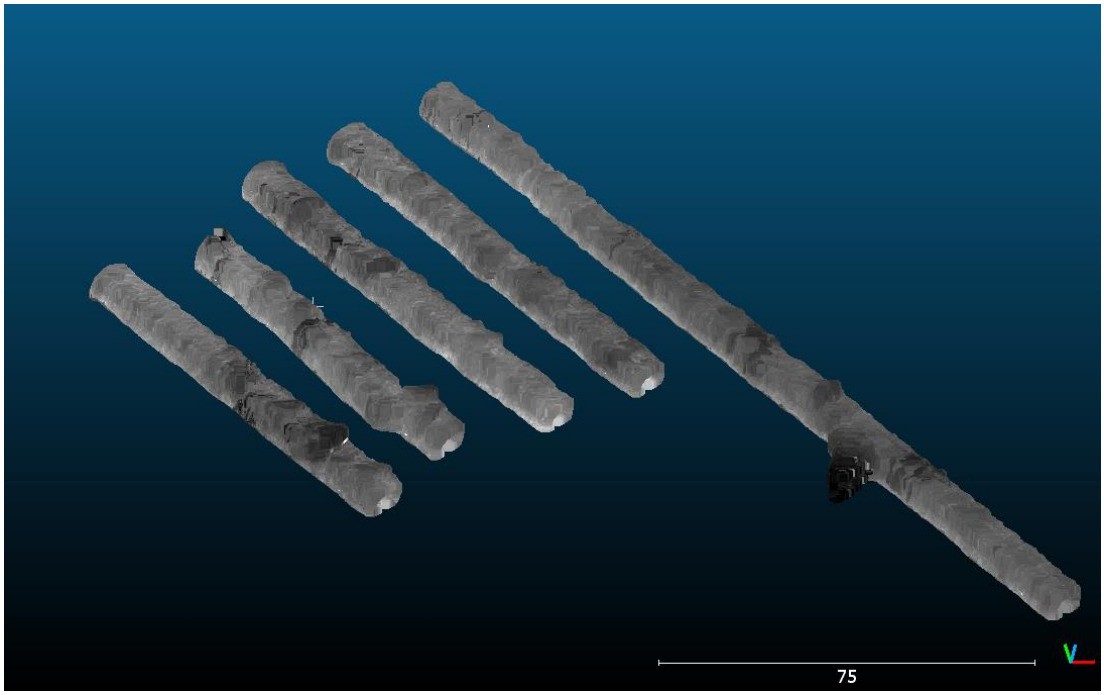

Figure 58: AL 1082 & HO 1080 layout with intensity scans of five drifts (CloudCompare)

In AL1082o2780 two convergence monitoring results are given. These are in a period of five weeks and show no evidence of a deformation trend. The drift has a smaller spread of weak rock masses than the neighbouring drifts 2800 and 2820. On the other hand, the two data series reveal the convergence-divergence error again at the end of the drift as well as deformation given at the entry because of the ventilation hose. (Figure 59).

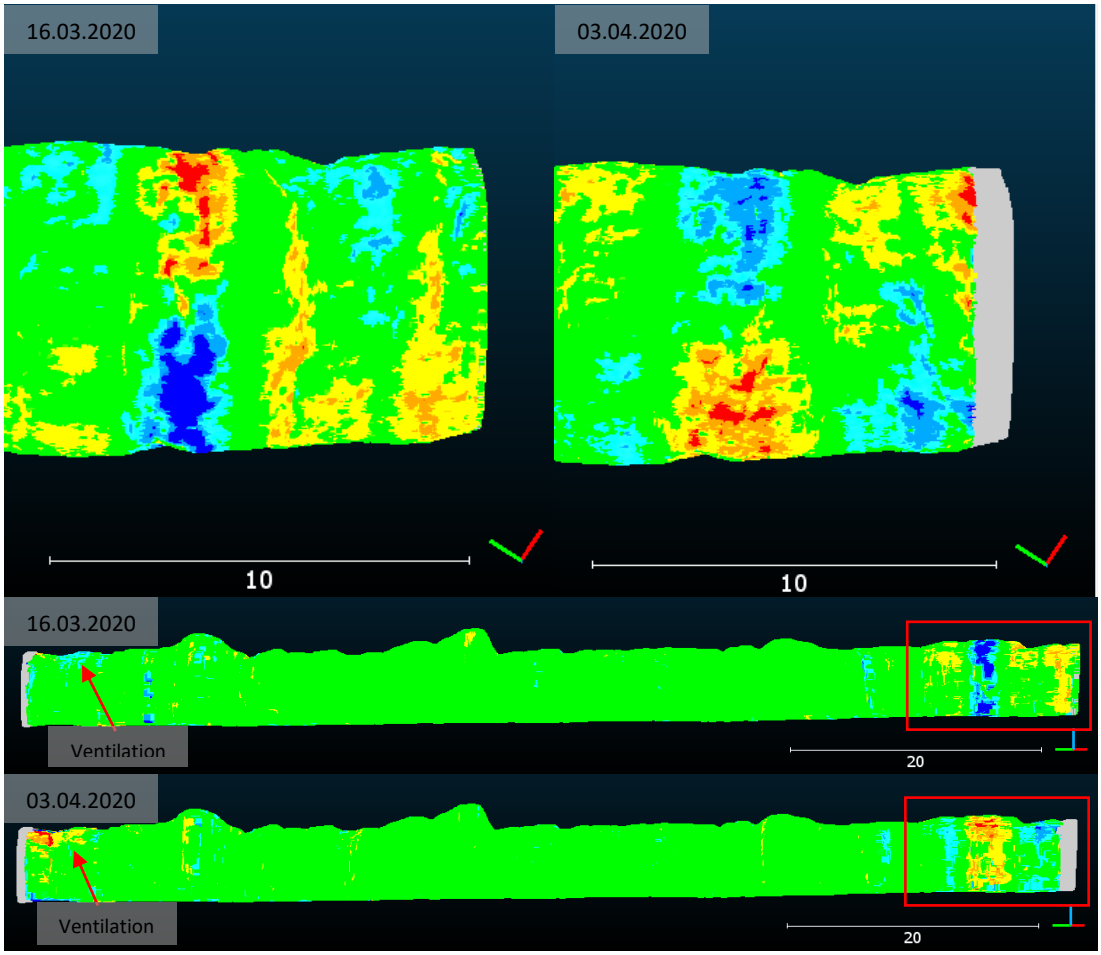

Figure 59: AL1082o2780 convergence monitoring with scan from 26.02.2020 & convergence-divergence error, squares indicate error bands at the end of the drift (CloudCompare)

In AL1082o2800, convergence can be seen in sections one to four on both sides of the wall, as well as on the floor and roof. The previous wall-to-wall distance measurements in section two showed a distance reduction of 3 cm in three months (Figure 35). It should be noted that the measurements are single point measurements for every 5 m and are not expected to represent the maximum deformation in the area but can be used a reference. By scanning, the convergence from 26.02.2020 to 05.05.2020 in the drift was analysed (Figure 60). Over this period, a maximum convergence of 27.2 cm and a maximum divergence of 14.1 cm was detected in the affected area. In the lower scan of 26.02.2020, sprayed cracks in the fibrecrete can be seen in form of lighter lines as well as the section numbering. The deformation on the left wall is concentrated lower (Appendix 2).

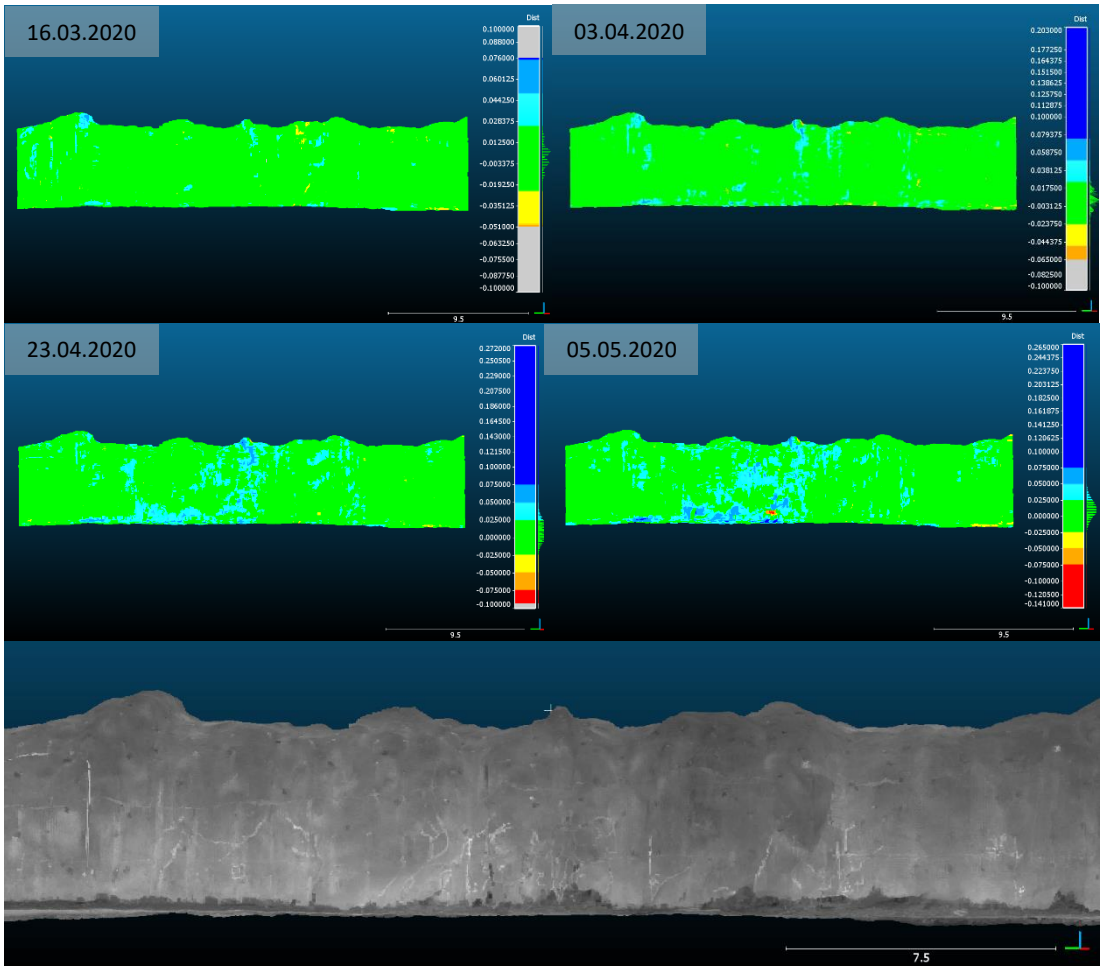

Figure 60: AL1082o2800 convergence monitoring of right wall with scan from 26.02.2020 and intensity scan from 26.02.2020 (CloudCompare)

In AL1082o2820, there was only target during the first three scans, so there is only one convergence monitoring file of two later scans.

Since HO1080 is of huge interest, five convergence monitoring files from HO1080o2740 are available. Nevertheless, detecting deformation trends proved to be difficult, as the values are very distorted (Figure 61). For instance, in the first two weeks of the test series at the entrance of the drift, there is an offset of the floor by more than 1 m in convergence. In the area of the roof where there had been a big rock fall the deformation increases by time, which shows a clear progression within 2.5 months monitoring time circled in red in Figure 61. The bottom scan shows clearly how it is possible to detect water, characterized by darker areas on the surface of the fibrecrete.

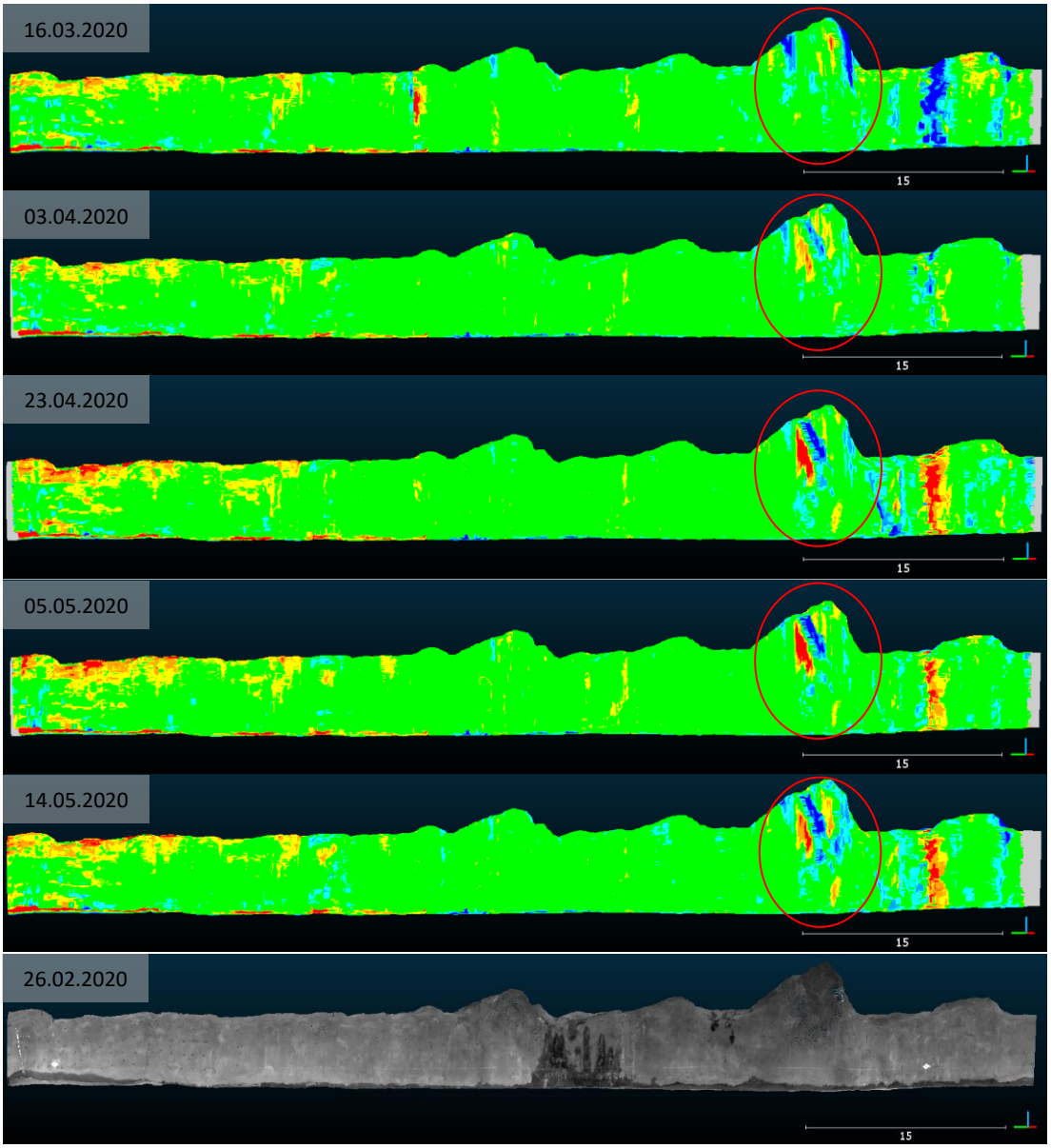

Figure 61: HO1080o2740 convergence monitoring with a scan from 26.02.2020 and intensity scan of 26.02.2020, circles indicate rock fall area (CloudCompare)

The drift HO1080o2760 has a unique layout due to an error during blasting, as the direction had to be adjusted during development (Figure 62). Exactly at this bend, convergence occurs which is shown in the convergence monitoring. The deformation increases at the edges of the curve so that the access becomes narrow with time.

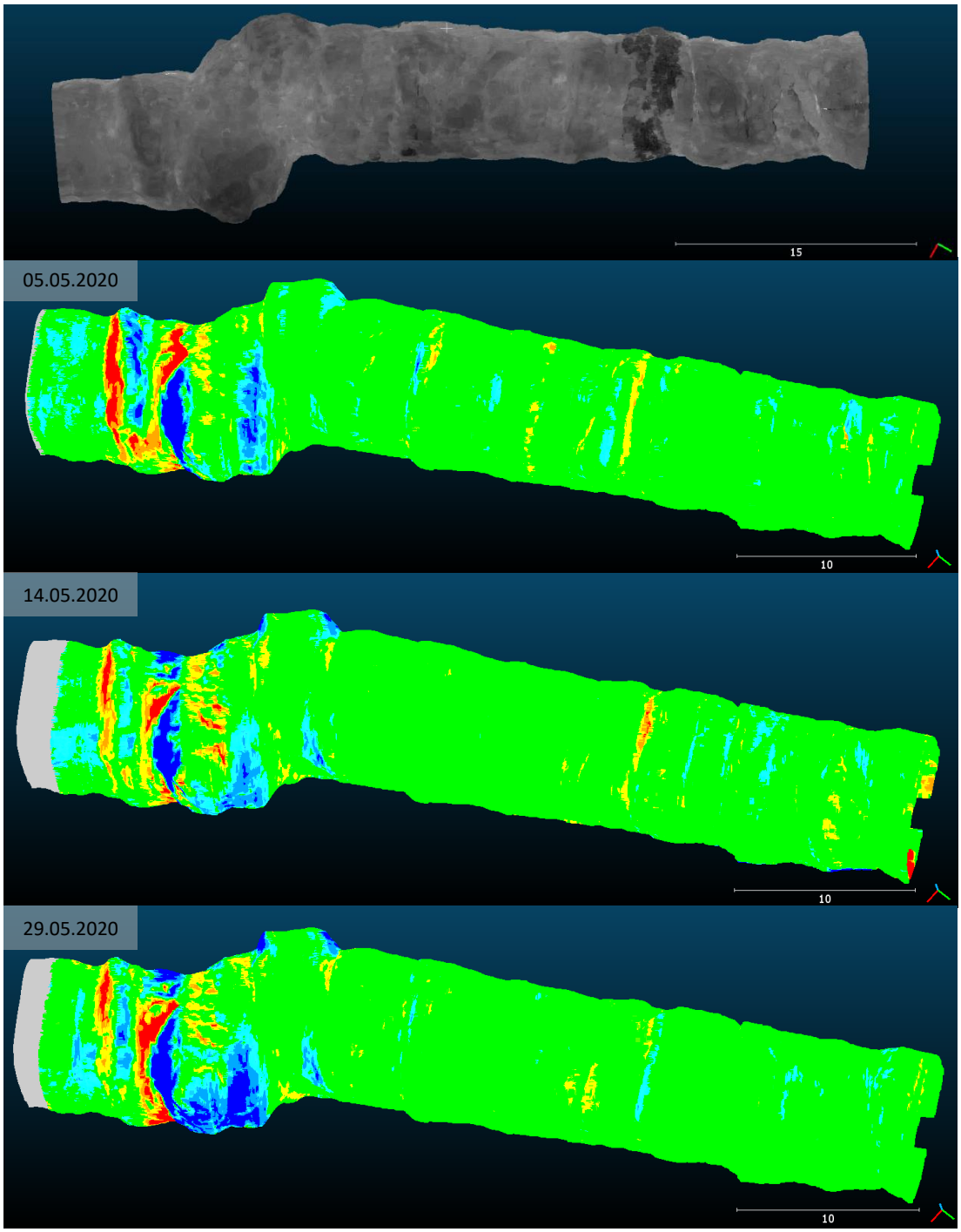

Figure 62: HO1080o2760 in plan view & convergence monitoring with a scan from 03.04.2020, lateral plan view (Cloud Compare)

In HO1051o2730 one convergence monitoring file with a time span of two weeks exists and in it there is a difference in ventilation similar to the one in drift HO1051o2750 (Figure 63), so the data is not suitable for an identification of trends in deformation (Appendix 2). However, there is no possibility given to detect deformation trends in the two other drifts, 2750 and 2770, either, despite several

scans. The data is not accurate enough due to the long and varying ventilation tubes and the divergence-convergence error that occurs in both drifts (Figure 63).

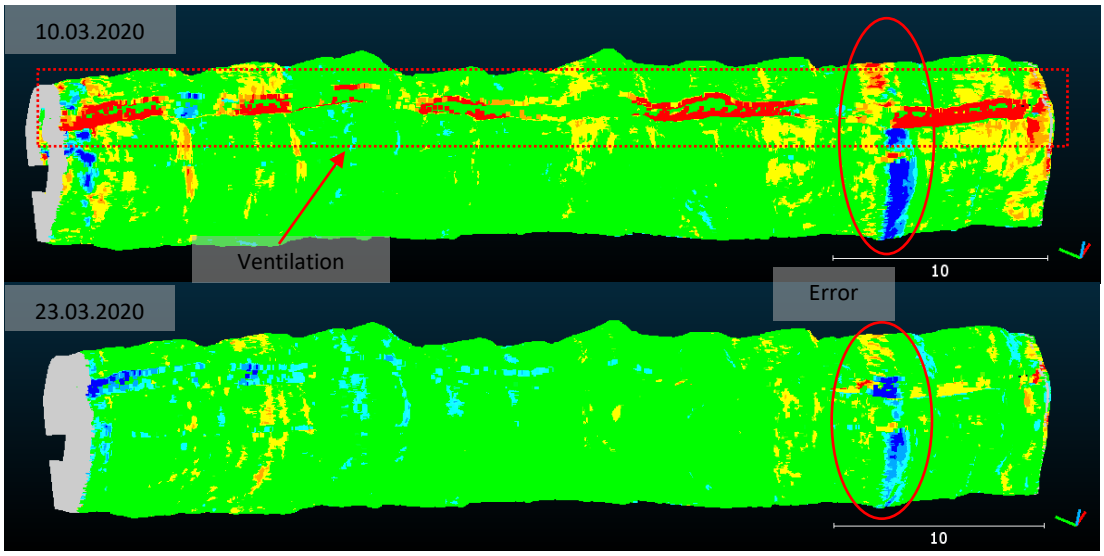

Figure 63: HO1051o2750 convergence monitoring with scan of 21.02.2020, circles indicate error bands at the end of the drift (CloudCompare)

There is one convergence monitoring file in AL1052o2790 and HO1023o2640 as well as none in HO1023o2680, which is why the areas cannot be assessed on trends in deformation.

7 Discussion

This chapter is divided in two parts. First, it discusses the key findings in the research work regarding the impact of rock mechanical properties on the deformation as well as the magnitude of deformation in two subsections. Second, it discusses the real-life capabilities of the uGPS Rapid Mapper™ derived by conducted tests as well as the field work.

7.1 Deformation in the mine

Through 353 scans in total, many tests, convergence measurements as well as field observations, current deformations could be detected in the mine. A number of other data series were also used to assist in this process.

7.1.1 Printzsköld

The scans allowed to find convergence at the ore contact zone, a geotechnically weak zone in this specific case, in PR996o4090 and compare it to conventional methods like the wall-to-wall distance measurements with a manual laser distance meter. It is noticeable that the deformation results of the convergence monitoring with the uGPS Rapid Mapper™ are several times higher because they show the whole area instead of only one random point every 5 m like the point-to-point measurements. Thus, assessing the real maximum deformation is better possible with the uGPS Rapid Mapper™ since it is more comprehensive. To be precise, the wall-to-wall distance in PR996o4090 decreased in the past by 15 cm within six months, whereas the new results show a maximum convergence of 26.2 cm for one side within 5.5 months. In PR1023o4080 a similar result is derived. In the same section the wall-to-wall distance decreased in the past by 6 cm in three months and in the convergence monitoring the maximum convergence is 10.5 cm in two months. The obtained values by scanning cover a greater area and are better suited to assess deformation trends with a higher areal resolution of the desired drift or drift part.

In PR996o4090 the shown deformation occurs in front of the orebody at a location with grey leptite with biotite intrusions which is surrounded by stronger rock masses of red grey leptite and magnetite. The area shows the same geotechnical settings as PR1023o4080 and PR1023o4100 but no GSI-values by face mapping are given. Based on PR1023 it can be stated that the grey leptite has a GSI-value of 30-35 whereas the surrounding rock masses have a value of 60-65 for magnetite and 40-45 for red grey leptite. The area was rehabilitated before scanning started. So, further progressing deformation with the mobile laser scanner could be detected after rehabilitation. Thus, the drift was obviously showing higher deformation rates in the past before being rehabilitated and lacked stability.

In PR1023o4060 no trend in deformation is apparent between 19.03.2020 and 29.05.2020. Here the geology is also different from neighbouring drifts with red grey leptite with a GSI-value of 45-55 being present with no stronger rock mass in front and a relatively weak beginning orebody with a GSI-value of 55.

In PR1023o4080 a total deformation of 10.5 cm in 2.5 months could be detected during the research time. Here the deforming area consists of grey leptite with a GSI-value of 30 at the ore contact zone surrounded by higher quality rock masses. Also, this drift was scaled, shotcreted and resupported in 10.2019 before scanning started and still a trend in deformation could be detected. Thus, also here deformation was apparent in the past that lead to a rehabilitation.

In PR1023o4100 a high deformation in the order of 25 cm could be investigated at many locations of the drift for a period of less than one month. The convergence monitoring clearly shows that there was relatively quick deformation happening between 21.02.2020 and 16.03.2020. That was months before closing and reinforcing the drift was decided due to large floor heave, large deformations, fibrecrete cracks and broken bolts. This is a proof that the system could be used to help identify and quantify areas of deformation before rehabilitation is necessary in a quick, easy and accurate investigation with the mobile scanner.

7.1.2 Alliansen and Hoppet

Detecting trends in AL and HO proved to be more difficult due to variations in the layout of the drifts and a lower number of useable scans.

In AL1082o2800 deformation by regular laser scanning could be assessed in an area with a massive biotite schist formation with a GSI-value of 30-40 which was already detected by detailed damage mapping in that entry. The total deformation is 27.2 cm in 2.5 months and is occurring where the wall is being pushed out from beneath the mesh line. The mesh is not installed far enough down and leaves the lower part of the walls unsupported. This shows that through regular scanning, negligent and incorrect installations of ground support can be detected and corrected by reacting to prevent serious consequences at an early stage.

In AL1082o2780 no trend was detectable during a period of six weeks. The drift shows no grey leptite and any biotite based on obtained data by face mapping and is therefore geotechnically more stable than other drifts on that level.

In HO1080o2760 progressing deformation occurs at the bended area which is also an area of lower rock quality with a GSI-value of 25-35 between the more competent magnetite and hematite orebody. Both factors together lead to a high rate of convergence.

In the adjacent drift HO1080o2740 no trend in deformation is detectable except than at the location of the rock fall. In front of the orebody there is a locally occurring granite with a GSI-value of 10, but no deformation is visible in the scans taken of this area.

7.2 Detected trends in deformation

It was possible to gain extensive insights in a total of eight drifts. In some drifts, not enough suitable scans could be conducted, interfering factors such as through-going ventilation were present or, as in PR1051, there was simply no deformation present so that no further conclusions could be drawn. It also must be noted that in many

drifts there were no more than three to four comparable and georeferenced scans, which made the analysis more challenging.

It is evident that especially weaker rock formations, such as biotite schist intrusions in mainly grey leptites or biotite schist formations, are squeezed by the large stresses in the deep mine, causing convergence and instability in the excavations. Especially if the rock formations are located between competent rock masses like red grey leptite, magnetite or hematite with a higher GSI-value. The deformation increases as the GSI-value difference between the prone to deformation area and the adjacent rock masses increases. An additional factor is the proximity to production causing more stress and consequently leading to possible deformation. It will be interesting to investigate if there will be similar trends in deformation in PR1051 as in the upper levels as production continues to progress downwards. When viewed with only the factors gained from this study it is only a matter of time before deformation will occur in PR1051.

As a general guideline, in PR996 and PR1023 areas with a GSI-value of 25-35 tend to deformation and in HO1080 and AL1082 areas with a GSI-Value of 10-25 show deformation. Also, the occurrence of water correlates positively with detected deformation.

Applications proposed by Jones and Beck (2017) for mobile LiDAR scanners in underground excavations include:

- Assessing the effectiveness of ground support designs.
- Assessing the rock mass response of different geotechnical areas.
- The scheduling of rehabilitation to plan access restrictions in advance.
- As a warning for an excavation failure.

It became evident that in previously rehabilitated drifts, like Pr996o4090 and PR1023o4080, the deformation is lower compared to the drifts rehabilitated after the scans were conducted, like in PR1023o4100. Convergence monitoring with the uGPS Rapid Mapper™ can be used to detect critical areas with deformation at an early

stage and hence initiate rehabilitation at an earlier stage. By that the risk to human safety, damage to infrastructure, closure of drifts and production losses can be minimized further. Additionally, the effectiveness of ground support designs or new rehabilitations can be assessed by comparing convergence monitoring results of scans before and after the rehabilitation in the same drift. For the planning of access restrictions or rehabilitation in advance a fixed rule must be implemented such as the rehabilitation must take place after a total deformation of 40 cm or a deformation rate of 20 cm/month. The implementation of such a rule with an absolute number is out of scope for this thesis and requires extensive knowledge of the specific conditions in each orebody. It is also clearly possible to identify more specific lacks in the ground support design or installation such as in AL1082o2800 were the mesh was not installed far enough down the wall (Subsection 7.1.2).

7.3 Real-life capabilities of the uGPS Rapid Mapper™

Central objectives of the research were to assess deformations, define deformation trends and define how these can be detected with the used approach by understanding the uGPS Rapid Mapper™ and assessing its usability. This is the first use of the system in the mine and is seen as a big chance to gather three-dimensional data quickly in comparison to common stationary scanning applications.

So, after installing everything to be ready for scanning five tests were presented. Two of the tests were aimed more at ensuring proper use and eliminating possible sources of interference. These tests were simple and clear and the execution of what was studied is also given in the future (Subsections 5.3.1 & 5.3.2). The artificial convergence monitoring test with varying angles of incidence and the repeatability test proved to be useful. The error detected in the test often occurred due to the more complex structure of deformation in real conditions and was consequently filtered out in the investigation. This represents a main disadvantage of the convergence monitoring as soon as changes occur in the drift the monitoring can be

falsified. There are many things than can lead to fake deformation in convergence monitoring. Main factors during the research work at the Malmberget Mine were:

- Volume changes at the ventilation tubes
- New infrastructure such as shotcrete arches or mesh
- Alterations in the floor height due to scraping or laying down gravel

Sometimes the error is not really traceable and not from an external source but occurs because of a miss-matching of the compared laser scan lines across an angled surface as the vehicle drives by. This can lead to the error seen in Figure 46, especially when the angle of incidence is high, such as in the artificial deformation test. However, all mobile scanners suffer from this error and it is a well-understood error that does not detract from the usability. In the repeatability test one convergence monitoring of ten showed the observed error (Figure 48).

Another important point to follow is that the data series per drift is large enough. Two or three scans per drift are not sufficient to detect a deformation trend with certainty. Therefore, the data series should contain at least six scans per drift and should contain a deformation of at least 4 to 6 cm. Having additional data sources, such as damage mapping over a period of time or the wall-to-wall distance measurements is beneficial to further support the gained results. Also, marking sections on the walls with reflective spray paint is a big assistance. The paint is easy to see in the scans and provides a quick and simple help. However, according to the mine, this is not feasible for a mine-scale deployment because it is too labour-intensive.

The main intention of the research work to detect and track deformation on a regular basis with little work power is given. The uGPS Rapid Mapper™ successfully detects areas of deformation and trends over time. An advantage here of course is the immediate visualization and the 3D view which allows more conclusions to be drawn. The convergence monitoring of the uGPS Rapid Mapper™ should not be seen as a replacement for conventional monitoring techniques and should rather be used as a

conjunction to traditional measurement techniques like Jones and Beck (2017) recommended for the usage of mobile laser scanning.

8 Conclusion

The study aimed to identify the real-life capabilities of the uGPS Rapid Mapper™ and assess deformation in the Malmberget Mine. The real-life capabilities were investigated with several designed tests and during the scanning work. For assessing the deformation 353 scans within four months were performed. An additional objective of the project was to help the mine to react in advance to deformations in order to ensure a safe and continuous production.

The designed tests showed that the uGPS Rapid Mapper™ can detect deformations from 4 cm upwards, but the convergence monitoring can be affected by changes in the drifts such as new infrastructures, moving ventilation tubes and alteration in the floor height due to scraping or laying down gravel that have to be known to use the scans properly. Therefore, it is very important to pay extensive attention to certain features during the interpretation of data. These are:

- Alternating convergence and divergence especially close to target locations
- Conspicuously high deformation values
- Uneven, irregular and rough surfaces
- Changes in scan area such as new infrastructure or a changing floor height

The tests have also shown that the device is suitable for detecting large cracks as well as water in the used area.

The scanning results obtained by the uGPS Rapid Mapper™ and convergence monitoring to identify deformation gave a further insight on the magnitude of deformation and to the linkage to geotechnical parameters. Detected trends are:

- Geological trend:
    - Deformation occurs mainly in grey leptites with an increased share of biotite schist inclusions
    - Deformation increases when the GSI difference between deformed area and adjacent rock gets higher

- Geotechnical trend:
    - In the Printzsköld orebody at level 996 and 1023 areas with a GSI of 25-35 tend to deformation
    - In the Hoppet orebody at level 1080 and the Alliansen orebody at level 1082 areas with a GSI of 10-25 show deformation
- In humid areas there is more deformation – the occurrence of water correlates positively with the detected deformation

The obtained results are covered by the given results of classical observations in the research area. The scans were able to further support and visualize the suspected deformations. In addition, more accurate numbers and the distribution in the drifts could be determined and visualized. The work supports the assumption that convergence occurs mainly in areas of geotechnically weak zones and due to squeezing mechanisms.

9 Recommendations

In this chapter, possible recommendations are made that have evolved during the studies in order to improve the system as well as the determination of deformation trends:

- Perform further convergence monitoring especially in the areas where deformation was certainly found to continue to control the deformations as well as better understand the system
- Think in a larger time scale while conducting convergence monitoring – like in PR996o4090
- Conduct scans at areas with less data to do a proper convergence monitoring analysis with at least five scans
- Stick strictly to the simple scanning rules like doing the calibration accordingly, drive centered at a constant speed of 3 km/h, start and stop scan at the allocated points. Little changes have a big impact on the sensitive convergence monitoring
- Clean dirty targets promptly to ensure a high enough reflectivity for the alignment
- Define rules with absolute threshold numbers for the need of rehabilitation for detected deformation in convergence monitoring to further minimize risks caused by deformation

References

Alkayal, A. (2020). *Laser scanning of overbreak and time-dependent deformation for drifts at Malmberget mine.* Lulea University of Technology.

Ask, D., Cornet, F., Fontbonne, F., Nilsson, T., Jönsson, L., & Ask, M. (2009). New high-capacity quadruple packer tool for hydraulic stress measurements in mines and high-stress areas. *International journal of Rock Mechanics and Rock Engineering, 46*, pp. 1097-1102.

Atlas Copco. (2007). *Mining Methods in Underground Mining.* Nacka, Sweden: Atlas Copco.

Barla, G. (2005). Design analyses for tunnels in squeezing rock. In G. Barla, *11th International Conference of IACMAG* (pp. 3-22). Torino, Italy.

Barton, N. R., Lien, R., & Lunde, J. (1974). Engineering classification of rock masses for the design of tunnel support. *Rock Mech., 6*, pp. 189-239.

Barton, N., Loset, F., Lien, R., & Lunde, J. (1980). Application of the Q-system in design decisions. In M. Bergman, *Subsurface space, Volume 2* (pp. 553-561). New York: Pergamon.

Basarir, H. (2012). *Malmberget mine field visit report.* Lulea, Sweden: Division of Mining and Geotechnical Engineering, Lulea University of Technology.

Bergman, S., Kübler, L., & Martinsson, O. (2001). *Description of regional geological and geophysical maps of northern Norbotten county (east of the Caledonian orogen).* SGU Geological Survey of Sweden.

Bieniawski, Z. T. (1973). Engineering classification of jointed rock masses. *Transaction of the South African Institution of Civil Engineers, v. 15*, pp. 335-344.

Bieniawski, Z. T. (1989). *Engineering rock mass classifications: a complete manual for engineers and geologists in mining, civil and petroleum engineering.* New York: Wiley.

Bieniawski, Z. T. (1993). Classification of rock masses in engineering: The RMR system and future trends. In J. A. Hudson, *Comprehensive Rock Engineering, Volume 3* (pp. 553-573). New York: Pergamon Press.

Brady, B. H., & Brown, E. T. (2004). *Rock Mechnichs: For Underground Mining, 3rd ed.* Dordrecht, Netherlands: Springer.

Deere, D. U., & Deere, D. W. (1988). The rock quality designation (RQD) index in practice. In L. Kirkaldie, *Rock classification systems for engineering purposes, Volume 984* (pp. 91-101). Philadelphia: American Society for Testing Materials.

Deere, D. U., Hendron, A. J., Patton, F. D., & Cording, E. J. (1967). Design of surface and near surface construction in rock. *8th U.S. Symposium on Rock Mechanics: Failure and breakage of rock .* New York: Society of Mining Engineers, American Institute of Mining, Metallurgical, and Petroleum Engineers.

Dunstan, G., & Power, G. (2011). Sublevel caving. In P. Darling (Ed.), *SME Mining Engineering Handbook* (Third Edition ed., p. 1417/1437). Society of Mining, Metallurgy and Exploration (SME).

Granljung, M. (1999). *Bergmekaniskt övervakningssystem vid Printzsköldmalmen.* Lulea University of Technology.

Grimstad, E., & Barton, N. (1993). Updating the Q-system for NMT. *International Symposium on Sprayed Concrete-Modern use of wet mix sprayed concrete for underground support.* Oslo: Norwegian Concrete Association .

Harrison, J. P., & Hudson, J. A. (2000). *Engineering Rock Mechanics: An Introduction to the Principles.* Amsterdam, Netherlands: Elsevier Science & Technology.

Hoek, E. (1994). Strength of rock and rock masses. *International Society of Rock Mechanics New Journal, Version 2*, p. 4ß16.

Hoek, E. (1998). Reliability of Hoek-Brown estimates of rock mass properties and their impact on design. *International Journal of Rock Mechanics & Mining Sciences, Volume 35*, pp. 63-68.

Hoek, E. (2007). *Practical rock engineering.* RocScience.

Hoek, E., Marinos, P., & Benissi, M. (1998). Applicability of the Geological Strength Index (GSI) classification for very weak and sheared rock masses. The case of the Athens Schist Formation. *Bulletin of Engineering Geology and the Environment, Volume 57*, pp. 151-160.

Jones. (2018). *Malmberget Ground Control Management Plan.* TGS. Malmberget: LKAB.

Jones, E., & Beck, D. (2017). The use of three-dimensional laser scanning for deformation monitoring in underground mines: Paper No. 066. *13th AusIMM Underground Operator's Conference.*

Jones, T., Nordlund, E., & Wettainen, T. (2019). Mining-Induced Deformation in the Malmberget Mine. *Rock Mech Rock Eng*, pp. 1903-1916. Retrieved from https://doi.org/10.1007/s00603-018-1716-6

Lavigne, N. J., & Marshall, J. A. (2012). A landmark-bounded method for large-scale underground mine mapping. *Journal of Field Robotics*, pp. 861-879.

LKAB. (2018). *Annual and sustainability report 2018.*

LKAB. (2019). *Annual and sustainability report 2019.*

Lynch, B. K., Marr, J., Marshall, J. A., & Greenspan, M. (2017). *Mobile LiDAR-based convergence detection in underground tunnel environments.*

Magnor, B. (2007). *Modellering av biotitzoner I Malmberget, Alliansen och Printzschöld Hifab projekt 313188.*

Marinos, V. (2012). Assessing rock mass behaviour for tunelling. *Environmental & Engineering Geoscience, Volume 18(4)*, pp. 327-341.

Marinos, V., Marinos, P., & Hoek, E. (2005). The Geological Strength Index: applications and limitations. *Bulletin of Engineering Geology and the Environment, Volume 64(1)*, pp. 55-65.

Martin, C. D., Kaiser, P. K., & Christiansson, R. (2003). Stress, instability, and design of underground excavations. *International Journal of Rock Mechanics and Mining Sciences, 40(7-8)*, pp. 1027-1049.

Nordlund, E. (2013). Deep hard rock mining and rock mechanics challenges. pp. 39-56.

Peck Tech. (2016). *uGPS Rapid Mapper™ System, Automated Target Alignment.* Mining Technology Solution.

Potvin, Y., & Hadjigeorgiou, J. (2008). Selection of ground support for mining drives based on the Q-system. *Journal of the Southern African Institute of Mining and Metallurgy, 108(7)*, pp. 397-404.

Quinteiro, C., Quinteiro, M., & Hedström, O. (2001). Underground Iron Ore Mining at LKAB. In W. Hustrulid, & R. Bullock, *Underground Mining Methods - Engineering Fundamentals and International Case Studies* (pp. 361-364). Society for Mining, Metallurgy and Exploration (SME).

Singh, B., & Geol, R. K. (1999). Rock mass classification: a practical approach in civil engineering. *Elsevier Science*, p. 282.

Sjödberg, J. (2008). Three-dimensional unit stress tensor modeling of complex ore body geometry. *42nd U.S. Rock Mechanics Symposium and 2nd U.S. - Canada Rock Mechanics Symposium.* San Francisco.

Stille, H. (2001). Rock Support in Theory and Practice. In W. A. Hustrulid, & R. L. Bullock, *Underground mining methods: Engineering fundamentals and international case studies* (pp. 535-546). Littleton, Colorado, USA: Society for Mining, Metallurgy, and Exploration, Inc. (SME).

Varden, R. P., & Woods, M. J. (2015). Design approach for squeezing ground. In Y. Potvin, *Proceedings of the International Seminar on Design Methods in Underground Mining* (pp. 489-504). Perth, Australia: Australian Centre for Geomechanics.

Wettainen, T. (2010). *Analys och prognostisering av uppblockning i Printzsköld.* Lulea University of Technology.

Winsa, M. (2017). *Typförstärkning MUJ - Anvisning - revision 05.* TGM. Malmberget: LKAB.

Zlot, R., & Bosse, M. (2014). Efficient large-scale three-dimensional mobile mapping for underground mines. *Journal of Field Robotics, Volume 31, no. 5*, pp. 758-779. doi:10.1002/rob.21504

Appendix 1

Table: A 1: Descriptions and Ratings of the Parameters of the Q-Value (Barton et al. 1974)

Table 1. Descriptions and Ratings for the Parameters RQD, J_n, and J_r

1.	ROCK QUALITY DESIGNATION (RQD)		
A.	Very poor	0— 25	Note:
B.	Poor	25— 50	(i) Where RQD is reported or measured as ≤ 10 (including 0) a nominal value of 10 is used to evaluate Q in Eq. (1)
C.	Fair	50— 75	
D.	Good	75— 90	
E.	Excellent	90—100	(ii) RQD intervals of 5, i. e. 100, 95, 90, etc. are sufficiently accurate
2.	JOINT SET NUMBER	(J_n)	
A.	Massive, no or few joints	0.5—1.0	
B.	One joint set	2	
C.	One joint set plus random	3	
D.	Two joint sets	4	
E.	Two joint sets plus random	6	
F.	Three joint sets	9	
G.	Three joint sets plus random	12	Note:
H.	Four or more joint sets, random, heavily jointed, "sugar cube", etc.	15	(i) For intersections use $(3.0 \times J_n)$
J.	Crushed rock, earthlike	20	(ii) For portals use $(2.0 \times J_n)$
3.	JOINT ROUGHNESS NUMBER	(J_r)	
	(a) *Rock wall contact* and (b) *Rock wall contact before 10 cms shear*		
A.	Discontinuous joints	4	Note:
B.	Rough or irregular, undulating	3	(i) Add 1.0 if the mean spacing of the relevant joint set is greater than 3 m
C.	Smooth, undulating	2	
D.	Slickensided, undulating	1.5	
E.	Rough or irregular, planar	1.5	
F.	Smooth, planar	1.0	(ii) $J_r = 0.5$ can be used for planar slickensided joints having lineations, provided the lineations are favourably orientated
G.	Slickensided, planar	0.5	
	(c) *No rock wall contact when sheared*		
H.	Zone containing clay minerals thick enough to prevent rock wall contact	1.0 (nominal)	
J.	Sandy, gravelly or crushed zone thick enough to prevent rock wall contact	1.0 (nominal)	

Table 2. Descriptions and Ratings for the Parameters J_a and J_w

4.	JOINT ALTERATION NUMBER (J_a)		φ_r (approx.)	
	(a) *Rock wall contact*			
A.	Tightly healed, hard, non-softening, impermeable filling i. e. quartz or epidote	0.75	(—)	Note: (i) Values of $(\varphi)_r$ are intended as an approximate guide to the mineralogical properties of the alteration products, if present
B.	Unaltered joint walls, surface staining only	1.0	(25°—35°)	
C.	Slightly altered joint walls. Non-softening mineral coatings, sandy particles, clay-free disintegrated rock etc.	2.0	(25°—30°)	
D.	Silty-, or sandy-clay coatings, small clay-fraction (non-softening)	3.0	(20°—25°)	

Table 2. Continued

E.	Softening or low friction clay mineral coatings, i. e. kaolinite, mica. Also chlorite, talc, gypsum and graphite etc., and small quantities of swelling clays. (Discontinuous coatings, 1—2 mm or less in thickness)	4.0	(8^0—16^0)
	(b) *Rock wall contact before 10 cms shear*		
F.	Sandy particles, clay-free disintegrated rock etc.	4.0	(25^0—30^0)
G.	Strongly over-consolidated, non-softening clay mineral fillings (Continuous, < 5 mm in thickness)	6.0	(16^0—24^0)
H.	Medium or low over-consolidation, softening, clay mineral fillings. (Continuous, < 5 mm in thickness)	8.0	(12^0—16^0)
J.	Swelling clay fillings, i. e. montmorillonite (Continuous, < 5 mm in thickness). Value of J_a depends on percent of swelling clay-size particles, and access to water etc.	8.0—12.0	(6^0—12^0)
	(c) *No rock wall contact when sheared*		
K, L, M.	Zones or bands of disintegrated or crushed rock and clay (see G, H, J for description of clay condition)	6.0, 8.0 or 8.0—12.0	(6^0—24^0)
N.	Zones or bands of silty- or sandy clay, small clay fraction (non-softening)	5.0	
O, P, R.	Thick, continuous zones or bands of clay (see G, H, J for description of clay condition)	10.0, 13.0 or 13.0—20.0	(6^0—24^0)

5.	JOINT WATER REDUCTION FACTOR	(J_w)	Approx. water pressure (kg/cm²)	
A.	Dry excavations or minor inflow, i. e. < 5 l/min. locally	1.0	< 1	Note: (i) Factors C to F are crude estimates. Increase J_w if drainage measures are installed
B.	Medium inflow or pressure occasional outwash of joint fillings	0.66	1.0— 2.5	
C.	Large inflow or high pressure in competent rock with unfilled joints	0.5	2.5—10.0	(ii) Special problems caused by ice formation are not considered
D.	Large inflow or high pressure, considerable outwash of joint fillings	0.33	2.5—10.0	
E.	Exceptionally high inflow or water pressure at blasting, decaying with time	0.2—0.1	> 10.0	
F.	Exceptionally high inflow or water pressure continuing without noticeable decay	0.1—0.05	> 10.0	

Table 3. Descriptions and Ratings for the Parameter *SRF*

6.	STRESS REDUCTION FACTOR			(*SRF*)
	(a) *Weakness zones intersecting excavation, which may cause loosening of rock mass when tunnel is excavated*			
A.	Multiple occurrences of weakness zones containing clay or chemically disintegrated rock, very loose surrounding rock (any depth)			10.0
B.	Single weakness zones containing clay, or chemically disintegrated rock (depth of excavation $\leqq 50$ m)			5.0
C.	Single weakness zones containing clay, or chemically disintegrated rock (depth of excavation > 50 m)			2.5
D.	Multiple shear zones in competent rock (clay free), loose surrounding rock (any depth)			7.5
E.	Single shear zones in competent rock (clay free) (depth of excavation $\leqq 50$ m)			5.0
F.	Single shear zones in competent rock (clay free) (depth of excavation > 50 m)			2.5
G.	Loose open joints, heavily jointed or "sugar cube" etc. (any depth)			5.0
	(b) *Competent rock, rock stress problems*	σ_c/σ_1	σ_t/σ_1	
H.	Low stress, near surface	> 200	> 13	2.5
J.	Medium stress	200—10	13—0.66	1.0
K.	High stress, very tight structure (Usually favourable to stability, may be unfavourable to wall stability)	10—5	0.66—0.33	0.5—2.0
L.	Mild rock burst (massive rock)	5—2.5	0.33—0.16	5—10
M.	Heavy rock burst (massive rock)	< 2.5	< 0.16	10—20
	(c) *Squeezing rock;* plastic flow of *incompetent rock under the influence of high rock pressures*			
N.	Mild squeezing rock pressure			5—10
O.	Heavy squeezing rock pressure			10—20
	(d) *Swelling rock; chemical swelling activity depending on presence of water*			
P.	Mild swelling rock pressure			5—10
R.	Heavy swelling rock pressure			10—15

Note:

(i) Reduce these values of *SRF* by 25—50% if the relevant shear zones only influence but do not intersect the excavation

(ii) For strongly anisotropic stress field (if measured): when $5 \leqq \sigma_1/\sigma_3 \leqq 10$, reduce σ_c and σ_t to $0.8\,\sigma_c$ and $0.8\,\sigma_t$; when $\sigma_1/\sigma_3 > 10$, reduce σ_c and σ_t to $0.6\,\sigma_c$ and $0.6\,\sigma_t$ where: σ_c = unconfined compression strength, σ_t = tensile strength (point load), σ_1 and σ_3 = major and minor principal stresses

(iii) Few case records available where depth of crown below surface is less than span width. Suggest *SRF* increase from 2.5 to 5 for such cases (see H)

Appendix 2

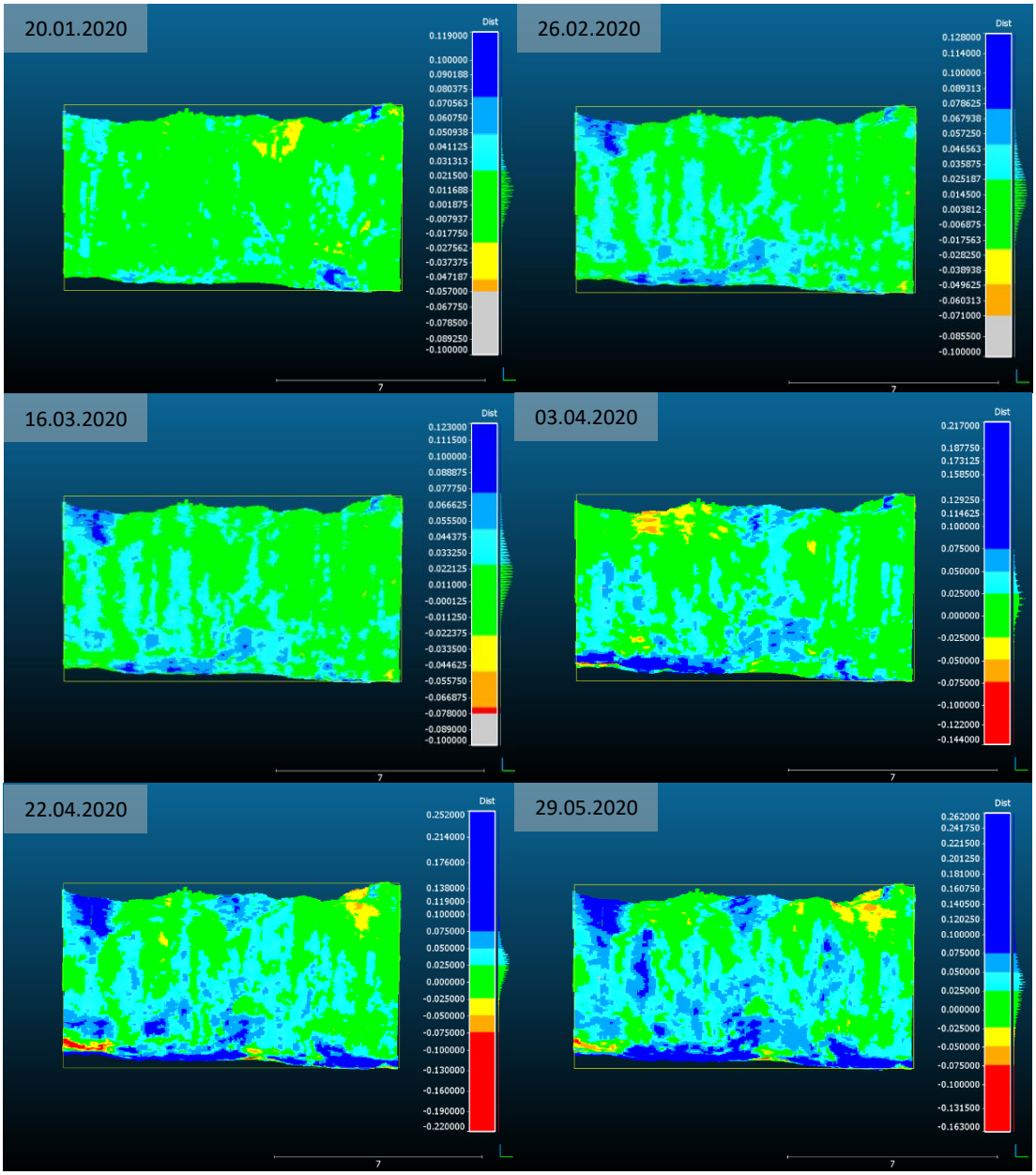

Figure A 1: PR996o4090, convergence monitoring on the left wall with a scan from 18.12.2019 (CloudCompare)

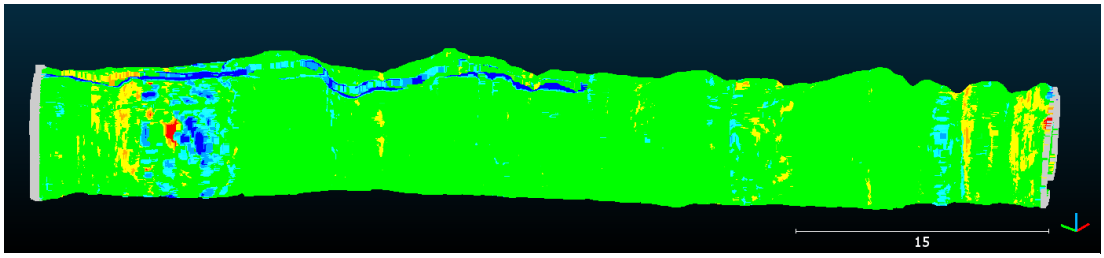

Figure A 3: HO1051o2730 convergence monitoring between 10.03.2020 and 05.05.2020 (CloudCompare)

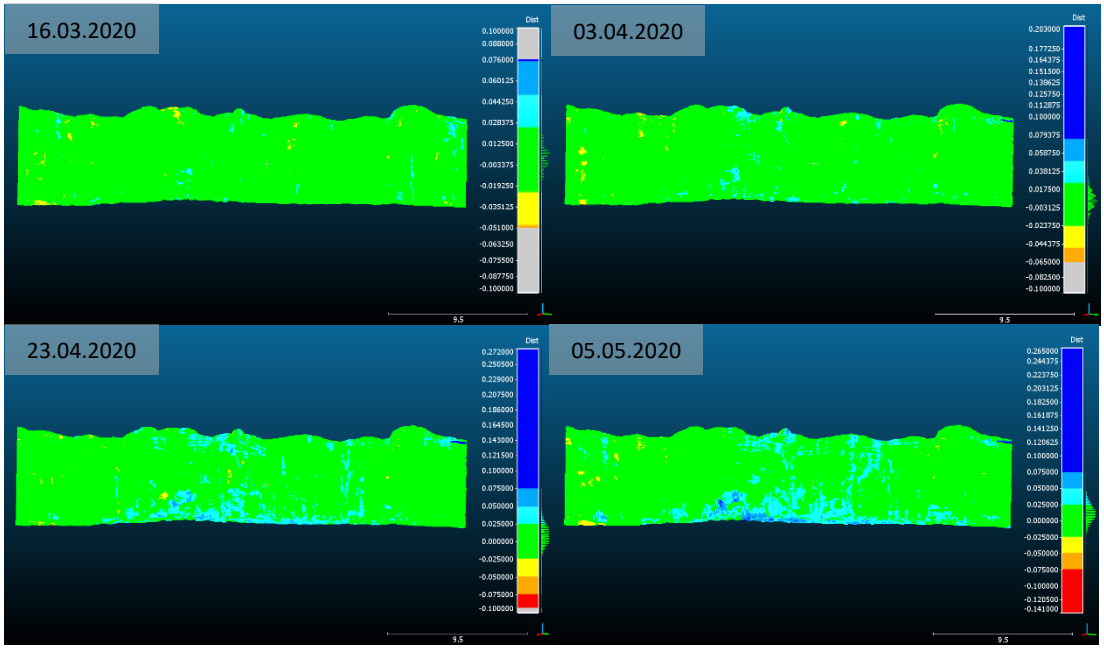

Figure A 2: AL1082o2800 convergence monitoring of left wall with scan from 26.02.2020 (CloudCompare)